

# The SPARC water vapour assessment II: Biases and drifts of water vapour satellite data records with respect to frost point hygrometer records

Michael Kiefer<sup>1</sup>, Dale F. Hurst<sup>2,3</sup>, Gabriele P. Stiller<sup>1</sup>, Stefan Lossow<sup>1</sup>, Holger Vömel<sup>4</sup>, John Anderson<sup>5</sup>, Faiza Azam<sup>6,7</sup>, Jean-Loup Bertaux<sup>8</sup>, Laurent Blanot<sup>9</sup>, Klaus Bramstedt<sup>6</sup>, John P. Burrows<sup>6</sup>, Robert Damadeo<sup>10</sup>, Bianca Maria Dinelli<sup>11</sup>, Patrick Eriksson<sup>12</sup>, Maya García-Comas<sup>13</sup>, John C. Gille<sup>14,15</sup>, Mark Hervig<sup>16</sup>, Yasuko Kasai<sup>17</sup>, Farahnaz Khosrawi<sup>1,18</sup>, Donal Murtagh<sup>12</sup>, Gerald E. Nedoluha<sup>19</sup>, Stefan Noël<sup>6</sup>, Piera Raspollini<sup>20</sup>, William G. Read<sup>21</sup>, Karen H. Rosenlof<sup>22</sup>, Alexei Rozanov<sup>6</sup>, Christopher E. Sioris<sup>23</sup>, Takafumi Sugita<sup>24</sup>, Thomas von Clarmann<sup>1</sup>, Kaley A. Walker<sup>25</sup>, and Katja Weigel<sup>6,26</sup>

<sup>1</sup>Karlsruhe Institute of Technology, Institute of Meteorology and Climate Research, Karlsruhe, Germany

<sup>2</sup>Cooperative Institute for Research in Environmental Sciences, University of Colorado, Boulder, Colorado, USA

<sup>3</sup>Global Monitoring Laboratory, NOAA Earth System Research Laboratories, Boulder, Colorado, USA

<sup>4</sup>Earth Observing Laboratory, National Center for Atmospheric Research, Boulder, Colorado, USA

<sup>5</sup>Hampton University, Hampton, Virginia, USA

<sup>6</sup>University of Bremen, Institute of Environmental Physics (IUP), Bremen, Germany

<sup>7</sup>Deutsches Zentrum für Luft- und Raumfahrt (DLR), Institute of Networked Energy Systems, Oldenburg, Germany

<sup>8</sup>LATMOS, Sorbonne Université, Paris, France

<sup>9</sup>ACRI-ST, 11 Boulevard d'Alembert, 78280 Guyancourt, France

<sup>10</sup>NASA Langley Research Center, Hampton, VA, USA

<sup>11</sup>Instituto di Scienze dell'Atmosfera e del Clima del Consiglio Nazionale delle Ricerche (ISAC-CNR), Bologna, Italy

<sup>12</sup>Department of Space, Earth and Environment, Chalmers University of Technology, Gothenburg, Sweden

<sup>13</sup>Instituto de Astrofísica de Andalucía, CSIC, Granada, Spain

<sup>14</sup>National Center for Atmospheric Research, Atmospheric Chemistry Observations & Modeling Laboratory, P.O. Box 3000, Boulder, USA

<sup>15</sup>Atmospheric and Oceanic Sciences, University of Colorado, Boulder, USA

<sup>16</sup>GATS Inc., Driggs, Idaho, USA

<sup>17</sup>National Institute of Information and Communications Technology (NICT), Terahertz Technology Research Center, Tokyo, Japan

<sup>18</sup>Institute for Advanced Simulations, Jülich Supercomputing Centre, Jülich, Germany

<sup>19</sup>Remote Sensing Division, Naval Research Laboratory, Washington, DC, USA

<sup>20</sup>Instituto di Fisica Applicata del Consiglio Nazionale delle Ricerche (IFAC-CNR), Sesto Fiorentino, Italy

<sup>21</sup>Jet Propulsion Laboratory, California Institute of Technology, Pasadena, California, USA

<sup>22</sup>Chemical Sciences Laboratory, NOAA Earth System Research Laboratories, Boulder, Colorado, USA

<sup>23</sup>Center for Research in Earth and Space Science, York University, Toronto, Canada

<sup>24</sup>National Institute for Environmental Studies, Tsukuba (Japan)

<sup>25</sup>Department of Physics, University of Toronto, Toronto, Canada

<sup>26</sup>Deutsches Zentrum für Luft- und Raumfahrt (DLR), Institut für Physik der Atmosphäre, Oberpfaffenhofen, Germany

**Correspondence:** Michael Kiefer (michael.kiefer@kit.edu)

## Abstract.

Satellite data records of stratospheric water vapour have been compared to balloon-borne frost point hygrometer (FP) profiles that are coincident in space and time. The satellite data records of 15 different instruments cover water vapour data available from January 2000 through December 2016. The hygrometer data are from 27 stations all over the world in the same period.

5 For the comparison, real or constructed averaging kernels have been applied to the hygrometer profiles to adjust them to the measurement characteristics of the satellite instruments. For bias evaluation, we have compared satellite profiles averaged over the available temporal coverage to the means of coincident FP profiles for individual stations. For drift determinations, we analyzed time series of relative differences between spatiotemporally coincident satellite and hygrometer profiles at individual stations. In a synopsis we have also calculated the mean biases and drifts (and their respective uncertainties) for each satellite

10 record over all applicable hygrometer stations in three altitude ranges (10 – 30 hPa, 30 – 100 hPa, and 100 hPa to tropopause). Most of the satellite data have biases  $< 10\%$  and average drifts  $< 1\% \text{ yr}^{-1}$  in at least one of the respective altitude ranges. Virtually all biases are significant in the sense that their uncertainty range in terms of twice the standard error of the mean does not include zero. Statistically significant drifts (95% confidence) are detected for 35% of the  $\approx 1200$  time series of relative differences between satellites and hygrometers.

## 15 1 Introduction

Water vapour is the most potent greenhouse gas in the atmosphere (Kiehl and Trenberth, 1997). Its radiative effect per unit mass change is strongest around the tropical tropopause (Riese et al., 2012; Solomon et al., 2010). Trends of stratospheric water vapour are expected to be related to the temperatures of the tropical tropopause where air transporting water vapour enters the stratosphere (e.g. Fueglistaler and Haynes, 2005; Randel and Park, 2019). Rising troposphere and tropopause temperatures due

20 to global warming may lead to increasing stratospheric water vapour abundances, initiating a positive feedback-loop where global warming will be further accelerated due to increasing water vapour abundances in the lower stratosphere (e.g. Gettelman et al., 2010; Dessler et al., 2013, 2016). In addition, the major stratospheric source of water vapour is the oxidation of methane (e.g. le Texier et al., 1988) which has more than doubled since 1800 (Blunier et al., 1993) and is expected to continue rising in future (e.g. Lelieveld et al., 1998), further increasing stratospheric water vapour.

25 Since 1980, despite constant or slightly decreasing tropical tropopause temperatures (Gettelman et al., 2009; Hu et al., 2015), an increase in stratospheric water vapour was observed over Boulder, Colorado (Oltmans and Hofmann, 1995). This cannot be explained by the high positive correlation between tropical tropopause temperatures and water vapour in the lowermost tropical stratosphere (Fueglistaler and Haynes, 2005; Randel and Park, 2019). In consequence, numerous studies have been performed to better understand the stratospheric water vapour budget and trends (e.g. Oltmans and Hofmann, 1995; Oltmans et al., 2000;

30 Rosenlof et al., 2001; Nedoluha et al., 2003; Hurst et al., 2011b; Dessler et al., 2014; Hegglin et al., 2014; Brinkop et al., 2016). Vertically resolved profiles of atmospheric water vapour have been observed around the globe by satellite-based instruments in low Earth orbits since the mid 1970s. From the year 2000 on, 15 different satellite instruments have observed vertically resolved water vapour distributions from the middle troposphere to the mesosphere and above. More than two decades ago, a

first assessment of the quality of water vapour observations including ground-based, balloon-borne and satellite instrumentation  
35 was published as the WCRP/SPARC (World Climate Research Programme/Stratosphere-troposphere Processes And their Role  
in Climate) report no. 2 (Kley et al., 2000). The many new satellite instruments in orbit since 2000 have made it of great interest  
to reassess the quality and consistency of water vapour observations from space. Here we concentrate only on stratospheric  
measurements by satellites and balloon-borne FPs.

Many of the satellite data records included in this study are described in detail by their data providers in reports and scientific  
40 papers (a compilation of information relevant to this paper is presented in Walker et al., The SPARC Water Vapour Assessment  
II: Data characterisation, to be submitted to AMT, 2023). These reports and scientific papers also contain, in most cases,  
some information about validation activities. Frost point hygrometers have often been used for satellite data validation since  
they are considered to be most accurate and internally consistent water vapour instruments for stratospheric measurements.  
Comparisons of different instruments, including their calibrations and data processing routines, were the focus of several field  
45 campaigns (Vömel et al., 2007a,b; Hurst et al., 2011a; Rollins et al., 2014; Vömel et al., 2016; Hall et al., 2016). Despite  
differences between the measurements by instruments employing different sensing techniques, consistency was found within  
the data from FPs.

Each comparison of satellite data records to the FP soundings, however, has been done in a slightly different way by each  
validation team, resulting in a wealth of validation publications that are not consistent down to the last detail. This lack of  
50 consistency hampers activities where several satellite data records need to be merged to construct a long-term time series, e.g.,  
for trend assessments. For this reason, we decided for this WCRP/SPARC WAVAS-II (Water Vapor Assessment II) activity to  
perform the comparison of all available satellite data records obtained during the period of 2000 through 2016 to FP data in a  
fully consistent and reproducible way. We document here where the FP data came from, how we made them comparable to the  
satellite data, and how the comparisons were performed. Overall, all of our satellite-to-FP comparisons are done in a similar  
55 way. The result of this activity is the first fully self-consistent quality assessment of vertically resolved biases and drifts in the  
stratospheric water vapour measurements by numerous satellite instruments and FPs, along with the respective uncertainties.  
In order to be consistent with the other assessments within the WCRP/SPARC WAVAS-II activity (see ACP/AMT/ESSD  
special issue “Water vapour in the upper troposphere and middle atmosphere: a WCRP/SPARC satellite data quality assessment  
including biases, variability, and drifts”, [https://amt.copernicus.org/articles/special\\_issue10\\_830.html](https://amt.copernicus.org/articles/special_issue10_830.html)), we use the same data  
60 versions as used in other papers in the WAVAS-II special issue, even in cases where newer data versions have become available  
in the meantime.

The paper is structured as follows: In Section 2 we describe the FP data and the satellite data records, including their  
preparation for use within this study. Further we explain how we made the FP data comparable in terms of their vertical  
resolution, and how the biases and the drifts have been calculated. Section 3 presents the assessment of the biases between the  
65 satellite and FP data records, starting with each individual satellite data record versus the FP data at each site, then discussing  
comparisons of all satellite data versus one station, as well as one satellite data record versus all stations. We summarise these  
findings with a synopsis of the biases and their uncertainties for each satellite data set over all its associated FP sites, in three  
different altitude ranges. Section 4 presents the assessment of instrumental drifts of the satellite data records against FP records,

also including a synopsis of the drifts of each satellite data set, in three altitude ranges, over all its associated FP sites. Section 5  
70 summarises our findings and offers recommendations for the use of the satellite data records under assessment. The individual  
bias and drift figures for pairs of satellite records and FP stations are presented in the Supplement and Appendix to this paper,  
respectively.

## 2 Data and data handling

In this study, we compare the satellite data records under assessment in the WCRP/SPARC WAVAS-II activity to reference-  
75 quality FP soundings at 27 stations (79°N to 45°S latitude) during 2000 through 2016. 31 data records from 15 different  
satellite instruments provide a subset of measurements coincident with the FP soundings (for coincidence criteria see below)  
that can be evaluated against the profile data from FP balloon soundings. In the following, we briefly describe FP and satellite  
data, explain the adjustments of the vertical resolution of the FP data to each of the various satellite data records, and describe  
the methods for the bias and drift assessments.

### 80 2.1 Frost point hygrometer data

The chilled mirror technique (Brewer, 1949; Barrett et al., 1950) is based upon the well-known equilibrium thermodynamic  
relationship (Clausius-Clapeyron) between an ice or liquid water surface and overlying water vapour. Frost point hygrometers  
actively maintain the equilibrium of this two phase system by continuously adjusting the temperature of the condensate layer  
such that it remains stable. Both the NOAA (National Oceanic and Atmospheric Administration) Global Monitoring Labora-  
85 tory's Frost Point Hygrometer (NOAA FPH) and the Cryogenic Frost-Point Hygrometer (CFH) use optical detection of the  
condensate layer on a small mirror. A feedback loop actively regulates the mirror temperature to maintain a stable condensate  
layer, making the water vapour content of the overlying air directly calculable from the mirror temperature.

The balloon-borne NOAA FPH was first flown over Boulder, CO, in 1980 (Oltmans et al., 2000) and, to date, has produced  
a 43-yr record of stratospheric water vapour mixing ratios (Hurst et al., 2011b). It has also been flown routinely at Lauder, New  
90 Zealand since 2004, Hilo, Hawaii since 2010, and has been part of a number of tropical, mid-latitude and polar measurement  
campaigns (Kley et al., 1997). The NOAA FPH payload is configured to enable measurements not only during ascent, but  
also during controlled (5 m/s) descent of the balloon when water vapour contamination is improbable. The FPH measurement  
uncertainty is largely determined by the stability of the frost layer, and under satisfactory performance, is 0.1–0.3 K in frost-  
point temperature in the stratosphere, leading to a measurement uncertainty of < 6 % for stratospheric mixing ratios (Hall et al.,  
95 2016).

The CFH (Vömel et al., 2007a,b; Vömel et al., 2016) works along the same principle as the NOAA FPH, but uses a feedback  
controller with a continuously variable PID parameter schedule to make observations between the surface and the middle  
stratosphere (25 km). The uncertainty of the condensate phase in the temperature range below 0°C is largely eliminated,  
allowing continuous profiles over a wider range of frost-point temperatures to be measured. It suffers no artefacts in cirrus  
100 clouds and may only be limited in wet precipitating clouds with the detector lens getting wet. The measurement uncertainty of

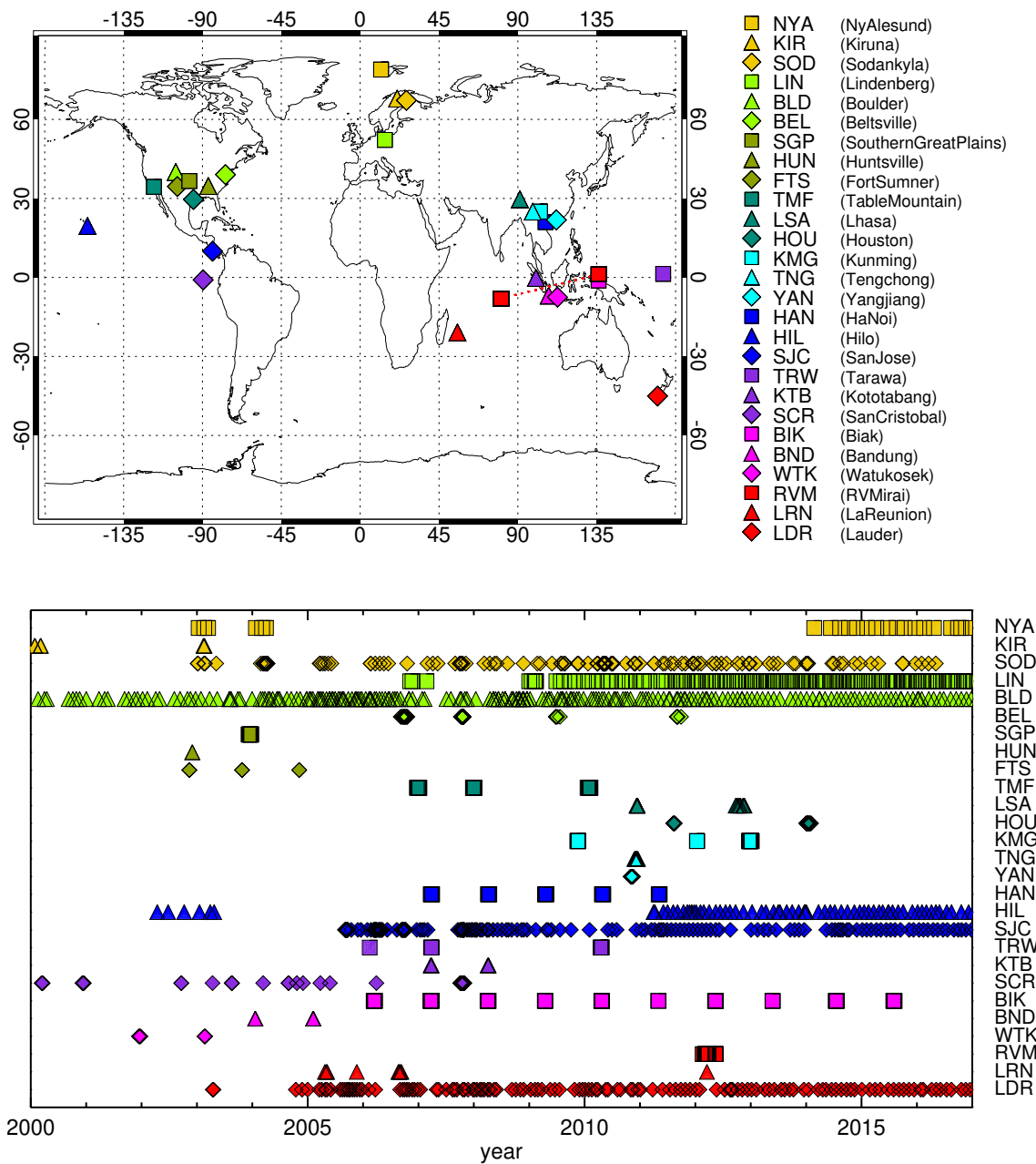


**Figure 1.** Locations of NOAA FPH and CFH stations that provided measurement data for these intercomparisons (top), and the temporal coverage of the data records at the respective stations (bottom). RVMirai was a measurement campaign based on a ship cruise. This is indicated by the dotted line connecting the respective symbols. In the lower plot each symbol represents at least one balloon-borne FP sounding. Note that some of the FP data sets began before 2000, but only the data from 2000 through 2016 are used here for bias and drift evaluations. FP record start dates are presented in Table 1.

**Table 1.** Overview of NOAA (National Oceanic and Atmospheric Administration) frost point hygrometer (NOAA FPH) and cryogenic frost point hygrometer (CFH) stations used for comparisons with satellite data.

#	Code	Site	Meas. period	Instrument type	Lat. / deg	Lon. / deg	Remark
1	BND	Bandung	2003 – 2004	CFH	-6.9	107.6	
2	BEL	Beltsville	2006 – 2011	CFH	39.0	-76.9	
3	BIK	Biak <sup>a</sup>	2006 – 2015	CFH	-1.2	136.1	
4	BLD	Boulder <sup>a</sup>	1980 – present	CFH/NOAA FPH	40.0	-105.2	
5	FTS	Fort Sumner	1996 – 2004	NOAA FPH	34.5	-104.3	
6	HAN	Hanoi	2007 – 2011	CFH	21.0	105.8	
7	HIL	Hilo <sup>a</sup>	2002 – present	CFH/NOAA FPH	19.7	-155.1	
8	HOU	Houston	2011, 2013	CFH/NOAA FPH	29.6	-95.2	
9	HUN	Huntsville	2002	NOAA FPH	34.7	-86.7	
10	KIR	Kiruna	1991 – 2003	NOAA FPH	67.8	20.2	
11	KTB	Kototabang	2007 – 2008	CFH	-0.2	100.3	
12	KMG	Kunming	2009 – 2012	CFH/NOAA FPH	25.0	102.7	
13	LRN	La Reunion	2005 – 2011	CFH	-20.9	55.5	
14	LDR	Lauder <sup>a</sup>	2003 – present	NOAA FPH	-45.0	169.7	
15	LSA	Lhasa	2010, 2013	CFH	29.7	91.1	
16	LIN	Lindenberg <sup>a</sup>	2006 – present	CFH	52.2	14.1	
17	NYA	Ny Alesund	2002 – 2004, 2013 – present	CFH/NOAA FPH	78.9	11.9	
18	RVM	Research Vessel Mirai	2011	CFH	-8.0/1.2	80.5/136.1	ship cruise
19	SCR	San Cristobal	1998 – 2007	CFH/NOAA FPH	-0.9	-89.6	
20	SJC	San Jose <sup>a</sup>	2005 – present	CFH	9.9	-84.1	incl. Alajuela, Heredia, San Pedro, and San Jose
21	SOD	Sodankyla <sup>a</sup>	1995 – present	CFH/NOAA FPH	67.4	26.6	
22	SGP	Southern Great Plains	2003	CFH	36.6	-97.5	
23	TMF	Table Mountain	2006 – 2009, 2013	CFH/NOAA FPH	34.4	-117.7	
24	TRW	Tarawa	2005 – 2010	CFH	1.4	172.9	
25	TNG	Tengchong	2010	CFH	25.0	98.5	
26	WTK	Wtukosek	2001 – 2003	NOAA FPH	-7.6	112.7	
27	YAN	Yangjiang	2010	CFH	21.9	112.0	

<sup>a</sup>) data from these sites were used for the drift analyses

the CFH is less than 0.5 K throughout the entire profile, which translates to conservative uncertainty values of 4 % in the lower troposphere and increasing to 9 % in the stratosphere.

Neither the CFH nor NOAA FPH require water vapour calibration standards or a water vapour calibration scale; only the mirror thermistor must be calibrated with high accuracy and this is accomplished using traceable standards of the US National  
105 Institute of Standards and Technology (NIST).

Temperature and pressure measurements used to convert frost point hygrometer data into relative humidity values and volume mixing ratios, respectively, are from the accompanying radiosondes on each balloon. Measurements of temperature and pressure have been provided by different radiosonde models throughout the years: Vaisala models RS80, RS92, and RS41, InterMet models iMet-1-RSB and iMet-4-RSB, and Meisei models RS-06G and RS-11G.

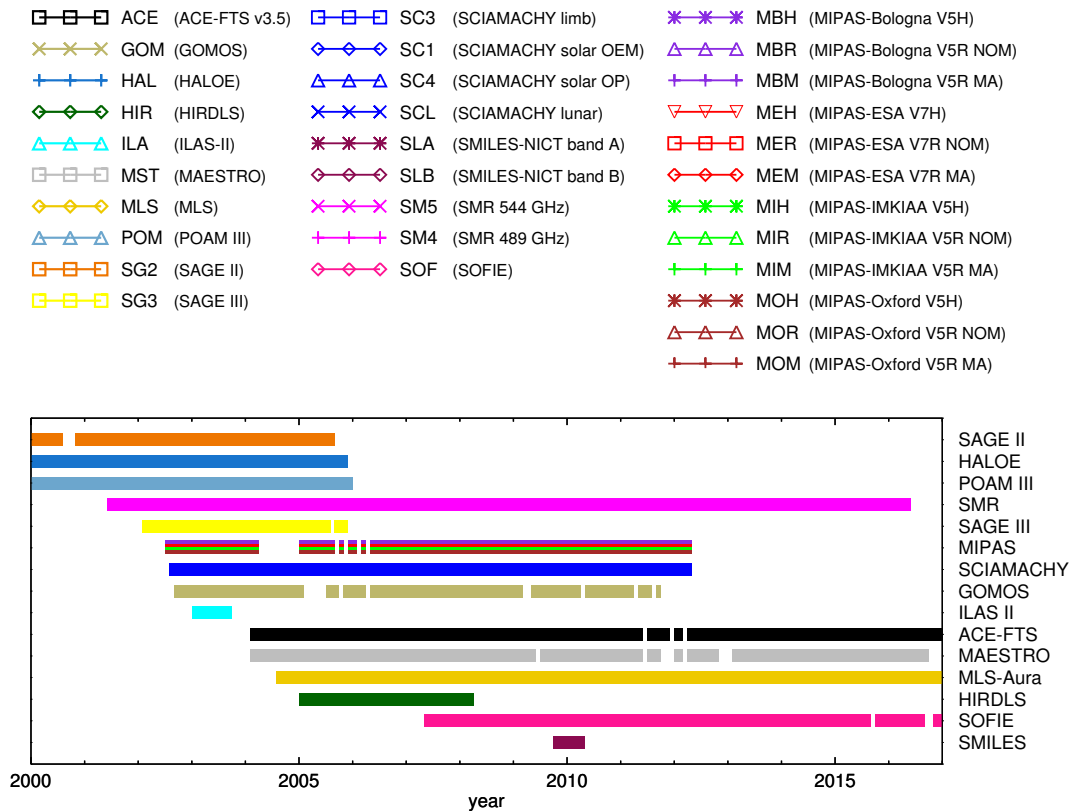
110 Offsets in the pressure measurements of radiosondes may bias the calculation of the mixing ratio in the stratosphere (Stauffer et al., 2014; Inai et al., 2015). To minimize this bias, the radiosonde pressure measurements are usually corrected using the radiosonde's acquisition of the geometric altitude by Global Navigation Satellite System (GNSS). In some radiosonde systems, the pressure is not measured directly but instead derived from the GNSS altitude. Only in older systems that precede the availability of GNSS observations on radiosondes starting in the late 1990s are pressures used without any corrections except  
115 those based on a simple pre-flight comparison at the surface with ground-based sensors. For this work we used FP mixing ratio averages on a fixed 250 m altitude grid. These are typically further reduced in vertical resolution as they are convolved with real or constructed averaging kernels for the different satellite instruments (see Section 2.3).

Table 1 lists the stations from which NOAA FPH or CFH data have been used for comparison with satellite data, together with their period of operation, the type of instrument launched, and the geographical coordinates of the site. Each station is  
120 given a 3-letter code to simplify its identification in the remainder of this paper. Fig. 1 provides an overview of the geographical locations and the measurement periods of the stations, together with the symbols and color codes that are used throughout this paper to mark the respective data of the stations.

In the remainder of this paper we do not distinguish between NOAA FPH and CFH so we continue to use the generic term "FP" for frostpoint hygrometer instruments and data.

## 125 **2.2 Satellite data**

Satellite data from all instruments providing measurements coincident with FP balloon soundings have been selected. Data quality filter criteria according to the original data descriptions from the data providers have been applied (for a summary of these data set specific criteria see Walker et al., The SPARC Water Vapour Assessment II: Data characterisation, to be submitted to AMT, 2023). No further bulk screening for data outliers surviving the previous data quality filtering has been applied. The  
130 31 satellite data records that are used in this comparison are listed in Table 2 along with their 3-letter codes. Fig. 2 shows the symbols and color codes for the satellite data sets used throughout this paper. The data versions we have assessed in this study are not the most recent ones to date for most of the satellite data sets. For reasons of consistency, the data versions used here are the same as those assessed by the other comparative studies of the SPARC WAVAS-II activity. It is left to future studies to evaluate if more recent data versions of water vapour satellite data are improved with respect to those assessed here. Such  
135 evaluations can also be done individually by comparing newer data versions to those assessed here to quantify any changes in the biases and drifts reported here.



**Figure 2.** Colors, symbols, and three-letter codes for the satellite data records used throughout the paper (upper part) and temporal distribution of available data of the respective satellite instruments on a monthly basis until the end of 2016 (lower part, not divided into measurement modes or data versions). Note that three of the SAT data sets began before 2000 (SAGE II 1984, HALOE 1991, POAM III 1998), but only the data from 2000 through 2016 are used here for bias and drift evaluations.

Two different sets of coincidence criteria were used in this paper: one for satellites providing data at high spatial and temporal densities, and one for lower density datasets. The criteria for dense samplers (HIRDLS, MIPAS, MLS/Aura, SCIAMACHY limb observations, SMILES, and SMR) were: time difference  $\Delta t \leq 24$  h, distance  $\Delta r \leq 1000$  km, latitudinal difference  $\Delta \text{lat} \leq 5^\circ$ . For less dense samplers (ACE-FTS, GOMOS, HALOE, ILAS-II, MAESTRO, POAM-III, SAGE-II, SAGE-III, SCIAMACHY occultation observations, and SOFIE) we relaxed the coincidence criteria to:  $\Delta t \leq 7 \times 24$  h,  $\Delta r \leq 2000$  km and latitudinal difference  $\Delta \text{lat} \leq 15^\circ$  to achieve enough coincidences for meaningful statistical evaluations of biases and drifts. For the troposphere, however, where high water vapour variability in smaller spatial and temporal scales is present, these criteria are too coarse. We have therefore restricted these analyses to water vapour measurements at altitudes above the local lapse rate tropopause determined from the radiosonde temperature profiles obtained simultaneously with the FP profiles using the WMO criterion (World Meteorological Organization, 1957). A companion paper (Read et al., 2022) comparing satellite data to FP and radiosonde measurements in the upper troposphere uses far stricter coincidence criteria.



**Table 2.** Overview of the water vapour data sets from satellites used in this study. Column “Retr. type” indicates whether the retrieval result was number density  $n_{\text{H}_2\text{O}}$  (marked ND) instead of vmr, and whether the retrieval was done in the  $\log(\text{vmr})$  or  $\log(n_{\text{H}_2\text{O}})$  domain. Column “Kernel type” holds the information whether a proper averaging kernel matrix (AK) or ad hoc smoothing kernels (SK) were used. The numbers in the last column indicate the FP stations that provided the data used for the drift analysis of the satellite data (compare to Table 1).

Code	Instrument	Data set version	Label	Retr. type	Kernel type	FP # for drift analyses
ACE	ACE-FTS	3.5	ACE-FTS v3.5		SK	4,7,16,20,21
GOM	GOMOS	LATMOS v6	GOMOS		SK	4,14,21
HAL	HALOE	v19	HALOE		SK	4
HIR	HIRDLS	v7	HIRDLS		SK	
ILA	ILAS-II	v3/3.01	ILAS-II		SK	
MST	MAESTRO	v31	MAESTRO		SK	4,14,16,21
MBH	MIPAS	Bologna V5H v2.3 NOM	MIPAS-Bologna V5H		AK	
MBR		Bologna V5R v2.3 NOM	MIPAS-Bologna V5R NOM		AK	3,4,14,20,21
MBM		Bologna V5R v2.3 MA	MIPAS-Bologna V5R MA		AK	4
MEH		ESA V7H v7 NOM	MIPAS-ESA V7H		AK	
MER		ESA V7R v7 NOM	MIPAS-ESA V7R NOM		AK	3,4,14,20,21
MEM		ESA V7R v7 MA	MIPAS-ESA V7R MA		AK	21
MIH		IMK/IAA V5H v20 NOM	MIPAS-IMKIAA V5H	log	AK	
MIR		IMK/IAA V5R v220/1 NOM	MIPAS-IMKIAA V5R NOM	log	AK	3,4,14,20,21
MIM		IMK/IAA V5R v522 MA	MIPAS-IMKIAA V5R MA	log	AK	4
MOH		Oxford V5H v1.30 NOM	MIPAS-Oxford V5H	log	SK	
MOR		Oxford V5R v1.30 NOM	MIPAS-Oxford V5R NOM	log	AK	3,4,14,20,21
MOM		Oxford V5R v1.30 MA	MIPAS-Oxford V5R MA	log	SK	21
MLS	MLS	v4.2	MLS	log	AK	3,4,7,14,16,20,21
POM	POAM III	v4	POAM III		SK	
SG2	SAGE II	v7.00	SAGE II		SK	4
SG3	SAGE III	Solar occ. v4	SAGE III		SK	
SC3	SCIAMACHY	Limb v3.01	SCIAMACHY limb	ND/log	AK	4,16,21
SCL		Lunar occultation v1.0	SCIAMACHY lunar	ND/log	SK	
SC1		Solar occ. - OEM v1.0	SCIAMACHY solar OEM	ND/log	AK	4,16,21
SC4		Solar occ. - OP v4.2.1	SCIAMACHY solar OP	ND	SK	4,16,21
SLA	SMILES	NICT v2.9.2 band A	SMILES-NICT band A		SK	
SLB		NICT v2.9.2 band B	SMILES-NICT band B		SK	
SM5	SMR	v2.0 544 GHz	SMR 544 GHz	log	AK	3,4,14,16,20,21
SM4		v2.1 489 GHz	SMR 489 GHz		AK	4,21
SOF	SOFIE	v1.3	SOFIE		SK	16,21

In our assessment of satellite measurements based on the occultation technique, we have not distinguished between sunset and sunrise measurements because the comparisons with FP profiles showed that there were only insignificant differences between sunrise and sunset measurements that could unequivocally be assigned to the respective satellite measurement mode.

In case of multiple coincidences of a given satellite water vapour profile with profiles of one FP data set we retain only the coincident profile pair with the lowest value of the sum of squares of spatial/temporal distances, normalized by the respective maximum allowed spatial/temporal distances from the appropriate coincidence criterion. Though this matching method slightly reduces the number of satellite profiles used for the bias assessment, there are usually enough coincidences during the 2000–155 2016 time period to work with. Therefore we have decided to minimize the contribution of natural variability using this method, i.e. considering the closest coincidences in space and time only.

We shall use the comprehensive term “SAT” for generic statements about the satellite data.

### 2.3 Adaptation of the vertical resolution of FP profiles to the satellite data and interpolation to a common grid

The vertical grids of all satellite data sets are coarser than the vertical grids of the FP profiles. More importantly, the vertical resolution of the satellite data is never as fine as the 250 m averages calculated from the 5–10 m native resolution of FP measurements. Therefore, prior to comparison, the vertical resolution of the FP data was necessarily adjusted to that of the satellite instrument. This was ideally done by application of the averaging kernel matrix (AK) and a priori profile of the latter for each satellite data set. However, in many cases, averaging kernels are not provided with the satellite data, so ad hoc averaging kernels were constructed. These constructed kernels were Gaussian-shaped smoothing kernels (SK) with the local vertical resolution of the satellite profile as full width at half maximum. The kernel type column of Table 2 shows whether AK or SK were applied to FP profiles for each satellite dataset. The modified FP profiles, and also the satellite profiles, were then interpolated on a common vertical grid, essentially defined by the respective satellite measurement grid. Technically, the pressure grid of all involved quantities (FP profiles and SAT profiles and kernels) was used to construct an altitude grid, which essentially represents  $\log P$ . This pseudo-altitude grid was used as a basis for all operations. The inverse transformation, i.e. from pseudo-altitude back to pressure was then used before the plotting and comparing of data. 170

For these steps, we have followed widely the method described in Stiller et al. (2012) as is briefly summarised here. As a first step, the FP profile on the finer grid is resampled on the coarser grid of the coincident satellite profile. Resampling of a coarse profile  $\mathbf{x}_c$  on a fine grid can be written as

$$\mathbf{x}_{cf} = \mathbf{W}\mathbf{x}_c, \quad (1)$$

where  $\mathbf{W}$  is an interpolation matrix. However, the mapping of a high-resolved profile  $\mathbf{x}_f$  on a less dense grid is not a unique operation, but a reasonable method to achieve this is (Rodgers, 2000, Chapter 10.3.1)

$$\mathbf{x}_{fc} = \mathbf{V}\mathbf{x}_f, \quad (2)$$

where

$$\mathbf{V} = (\mathbf{W}^T \mathbf{W})^{-1} \mathbf{W}^T, \quad (3)$$

which satisfies  $\mathbf{V}\mathbf{W} = \mathbf{I}$ ,  $\mathbf{I}$  = unity, and  $\mathbf{W}$  being an interpolation matrix. The application of the averaging kernel  $\mathbf{A}_c$  of the low-resolved profile  $\mathbf{x}_c$  to the better-resolved profile  $\mathbf{x}_f$  under consideration of the a priori profile  $\mathbf{x}_a$  of the low-resolved

retrieval is then performed on the coarse grid

$$\tilde{\mathbf{x}}_{fc} = \mathbf{A}_c \mathbf{V} \mathbf{x}_f + (\mathbf{I} - \mathbf{A}_c) \mathbf{x}_a \quad (4)$$

For some satellite data records there is another complication: instead of mixing ratios the logarithms of water vapour mixing ratios are retrieved (see column **Ret.type** of Table 2). The averaging kernels hence refer to the logarithms of the water vapour mixing ratios. The application of the averaging kernels of these specific measurements to the better resolved profile of the FP data on the basis of the coarse-grid averaging kernel  $\mathbf{A}_{inc}$  of the logarithm of the water vapour mixing ratio then is

$$\tilde{\mathbf{x}}_{fc} = \exp(\mathbf{A}_{inc} \mathbf{V} \ln(\mathbf{x}_f) + (\mathbf{I} - \mathbf{A}_{inc}) \ln(\mathbf{x}_a)). \quad (5)$$

For the cases that use an ad hoc smoothing kernel generated from information on the vertical resolution, there is also no a priori information available. Hence the equations 4 and 5 become

$$\tilde{\mathbf{x}}_{fc} = \mathbf{B}_c \mathbf{V} \mathbf{x}_f \quad \text{and} \quad \tilde{\mathbf{x}}_{fc} = \exp(\mathbf{B}_{inc} \mathbf{V} \ln(\mathbf{x}_f)). \quad (6)$$

with  $\mathbf{B}_c$  and  $\mathbf{B}_{inc}$  being the smoothing kernel on the coarse grid for the linear and logarithmic retrievals, respectively.

A common technical problem in convolving measured profiles with kernels of retrieved data is that the altitude ranges do not fit. Hence we extended the FP profile above and below its upper and lower boundaries by offset-corrected, climatological water vapour data from HAMMONIA (Hamburg Model of the Neutral and Ionized Atmosphere, Schmidt et al. (2006)) as a function of month and latitude. After the convolution step, the smoothed FP profile was cut to its original upper boundary. Since there is a possibly strong influence of the climatological HAMMONIA profile at the lower boundary, due to the rapidly increasing vmr-values below the hygropause, the FP profile was cut at one (local) vertical resolution distance above the original lower boundary to minimize the mapping of climatology information into the altitude range used for comparison.

Fig. 3 demonstrates the effect of the transformation on the comparison between the MIR satellite data and FP profiles at the equatorial station BIK. Due to the finer 250 m vertical resolution, there is a sharper and deeper minimum in the FP profile near 90 hPa than in the satellite profile. From this example it becomes clear that the use of the averaging kernel can have a strong effect on the result of the comparison of profiles of different vertical resolutions: Comparison of the two profiles, with the FP data simply interpolated to the coarser grid of the satellite instrument, but not smoothed (black diamonds), is misleading since the MIPAS instrument is unable to resolve the sharp feature in the profile. By application of the averaging kernel and a priori profile to the FP profile according to Eq. 5 (in the MIR data the logarithm of water vapour mixing ratio is retrieved, and the a priori is a profile of constant nonzero value) the FP profile is transformed into the profile the satellite instrument would measure if the hygrometer profile was the truth (black squares). Convolution of the FP profiles like this is the only way the two profiles can be compared in a meaningful manner. If averaging kernels and a priori profiles are not provided along with the satellite data record, the vertical resolution of the hygrometer profile can at least be adjusted using the constructed Gaussian-shaped averaging kernels. The effect of this smoothing is demonstrated by the profiles with black triangles in Fig. 3, and is notably different from the application of the MIPAS-specific averaging kernel and a priori information (black squares), which is particularly obvious for the averaged profiles (lower row of Fig. 3) and the corresponding differences. Clearly the application of

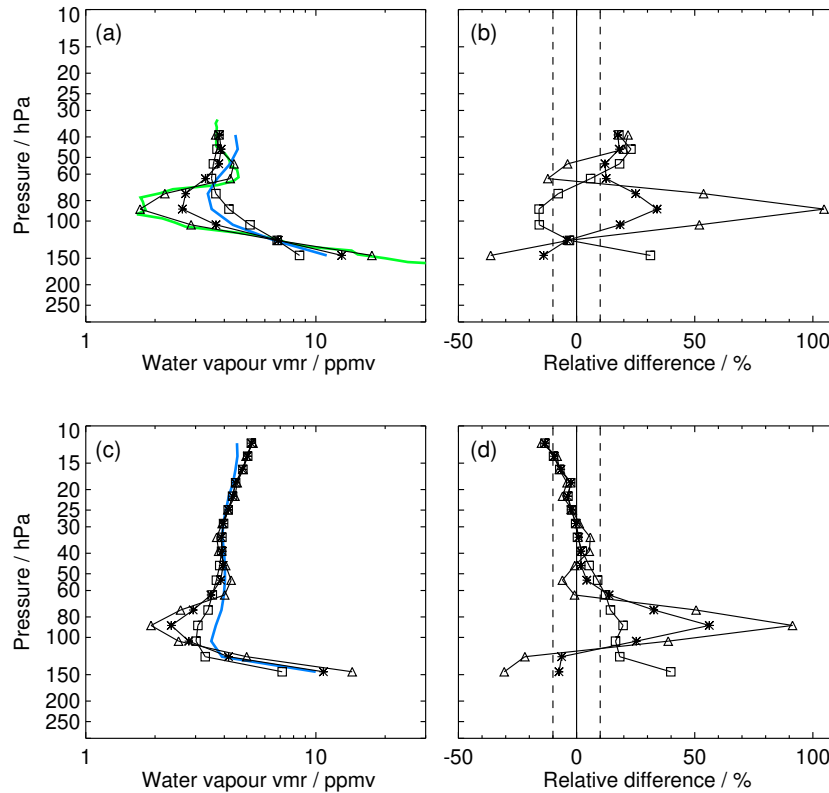


**Figure 3.** Impact of the different methods for adjustment of the vertical grid and resolution of FP profiles (here: BIK) to those of the satellite data records (here: MIR). Panel a: Sample single profiles of satellite (blue) and collocated FP data (green). Black diamonds: FP profile directly interpolated onto the coarse common grid, black triangles: FP profile smoothed with a Gaussian kernel (details see text), black squares: proper averaging kernels and a priori information applied to FP profile. Panel b: Corresponding relative differences for the three variants in terms of satellite profile minus FP profile. Panel c: Averaged profiles for coincident MIR (blue) and FP data at BIK (black, symbols as for data shown in panels a, b). Panel d: Corresponding relative differences of averaged profiles for the three variants in terms of satellite profile minus FP profile, divided by FP profile.

the correct vertical averaging kernels and a priori profiles adds further information on the altitude displacement and the content  
 215 of a priori information in the retrieved profiles to the FP profiles. In contrast, the application of ad hoc smoothing kernels alone  
 has a much weaker effect, nevertheless it reduces the large resolution-based differences between satellite and FP measurements  
 to a considerable degree. For this reason, we have employed the constructed smoothing kernels in all comparisons where no  
 kernel/a priori information for the satellite profiles was available.

### 3 Bias assessment from vertical profile comparisons

#### 220 3.1 Method of calculation of bias and standard error of the mean bias

We assess the bias between satellite data and the FP measurements as the mean difference between the satellite profiles and the coincident transformed FP profiles. For profile data of a given satellite instrument there is a set of  $J_s$  FP locations/stations with coincident profiles. At station  $j$  the bias for each grid point  $i$  is:

$$b_{j,i} = \frac{\sum_{n=1}^{N_{j,i}} (x_{c;j,n,i} - \tilde{x}_{fc;j,n,i})}{N_{j,i}} = \frac{\sum_{n=1}^{N_{j,i}} x_{c;j,n,i}}{N_{j,i}} - \frac{\sum_{n=1}^{N_{j,i}} \tilde{x}_{fc;j,n,i}}{N_{j,i}}, \quad (7)$$

225 i.e. it does not matter whether the individual differences are calculated first and then are averaged, or whether the difference of the appropriate averages are calculated. The bias  $b_{j,i}$  is calculated independently for each grid point  $i$  and FP station  $j \in \{1 \dots J_s\}$  from the available  $N_{j,i}$  coincident observations. For given  $j$ ,  $N_{j,i}$  can be different for different altitudes because the altitude coverage of a measurement system under assessment may vary from profile measurement to profile measurement. The standard error of the mean (SEM) of the bias, which is also the bias-corrected root mean squares (rms) difference of the  
230 profiles, is calculated as:

$$\sigma_{\text{bias};j,i} = \sqrt{\frac{\sum_{n=1}^{N_{j,i}} (x_{c;j,n,i} - \tilde{x}_{fc;j,n,i} - b_{j,i})^2}{N_{j,i}(N_{j,i} - 1)}}. \quad (8)$$

We consider the bias  $b_{j,i}$  as statistically significant if the interval  $b_{j,i} \pm 2\sigma_{\text{bias};j,i}$  does not include zero.

The mean relative bias (in percent) or percentage bias is calculated by dividing the mean bias  $b_{j,i}$  by the mean of the involved FP measurements and multiplying by 100. In all of the following figures, the differences provided are satellite profiles minus  
235 FP data. The latter was adapted to the vertical resolution of the satellite data according to Sec. 2.3 and Table 2 and, as well as the satellite data, brought to a common coarser vertical grid.

For a given satellite data set the mean bias over all stations and for a specific altitude range (e.g. 10–30 hPa, 30–100 hPa, and 100 hPa–tropopause as presented in Section 3.5) is calculated as follows:

$$b = \frac{\sum_{j=1}^{J_s} \sum_{i \in \mathbf{I}_j} w_{j,i} b_{j,i}}{\sum_{j=1}^{J_s} \sum_{i \in \mathbf{I}_j} w_{j,i}}. \quad (9)$$

240 Here  $\mathbf{I}_j$  represents the set of indices for all the altitudes from the given altitude range and FP comparison data set. The weights  $w_{j,i}$  are calculated from the SEM of the bias  $\sigma_{\text{bias};j,i}$  and the ratio of the width  $\Delta z_{j,i}$  of the common coarse grid to the vertical resolution  $r_{v;j,i}$  of the satellite measurement, according to

$$w_{j,i} = \frac{1}{\sigma_{\text{bias};j,i}^2} \frac{\Delta z_{j,i}}{r_{v;j,i}}. \quad (10)$$

The factor  $\frac{\Delta z_{j,i}}{r_{v;j,i}}$  in the weight is used to compensate for the discrepancy between actual vertical resolution and grid width.  
245 Without this factor, the SEM of the mean bias would directly depend on the grid width via the number of data points which are available in a given altitude range.

Finally the SEM of this mean bias over an altitude range is given by

$$\sigma_b = \sqrt{\frac{\sum_{j=1}^{J_s} \sum_{i \in \mathbf{I}_j} w_{j,i}^2 \sigma_{\text{bias};j,i}^2}{(\sum_{j=1}^{J_s} \sum_{i \in \mathbf{I}_j} w_{j,i})^2}}. \quad (11)$$

Again, the mean relative bias (in percent) or percentage bias is calculated by dividing the mean bias  $b$  by the mean of the  
 250 involved FP measurements and multiplying by 100.

### 3.2 Individual comparisons between satellite data records and FP stations

In this section we report on bias profiles of the satellite data records against the FP data from all the stations listed in Table 1. When using terms like, e.g., “above 100 hPa”, we always refer to altitudes above 100 hPa, i.e. “above” always means “higher up in the atmosphere”. The same applies to terms like, e.g., “below 30 hPa”; here, altitudes below the 30 hPa level are meant.  
 255 For the selected collocations within the coincidence criteria, SAT minus FP differences have been averaged for each satellite data record’s full period of coincident measurements. The comparisons for the individual SAT records vary considerably with respect to their measurement periods and numbers of coincidences. Some of the FP stations have operated their balloon soundings only during campaigns; others provide long-term measurement series based on soundings conducted at regular intervals, like LDR, SJC, BLD, and LIN. We have not separated the available comparisons into long-term and short-term  
 260 series, nor have we tried to detect any temporal variation in biases for the comparisons described in this section. Drifts of satellite data sets will be tackled in Section 4.

Fig. 4 shows, as an example, the comparison of one SAT data set, namely MLS, to one balloon station, namely TMF, to demonstrate the procedure of bias determination. For this figure, every individual collocated FP profile was treated according to Eq. 5, making use of the MLS averaging kernel and a priori data; since MLS data are provided on a fixed pressure grid,  
 265 further interpolation to a common vertical grid for calculation of the means over all collocations was not necessary. The comparison was limited to the vertical range above the local tropopause, with the tropopause pressure information estimated from the radiosonde temperature profiles accompanying the FP profiles. The mean SAT and FP profiles, calculated from the closest coincident data pairs, are shown in the left panel of Fig. 4, together with the standard deviations of the respective ensembles, which are displayed as shaded areas. In this example, the mean water vapour profile of the satellite data compares  
 270 well to the sonde data. Even the variability of SAT and FP mixing ratios are similar, indicating that the random uncertainties of the two measurement types are similar. Further, the deviation between the two measurements due to natural variability appears to be relatively small, i.e. the chosen coincidence criteria are stringent enough to avoid unwanted large differences that could result from location and/or time mismatches between the profiles. The mean bias of the two data sets (middle panel of Fig. 4) above 100 hPa is positive or zero, except for the uppermost data point, i.e. MLS on average has a positive bias relative to the  
 275 FP, which is at maximum +5 %. Below 100 hPa, close to the tropopause it has a sharp peak of -25 %. The standard error of the mean bias is very small at all satellite reporting levels, i.e. the bias assessment is quite accurate throughout the entire profile. The number of comparisons, in this case between  $\approx 30$  at the upper and lower ends of the profiles and about 350 for the central

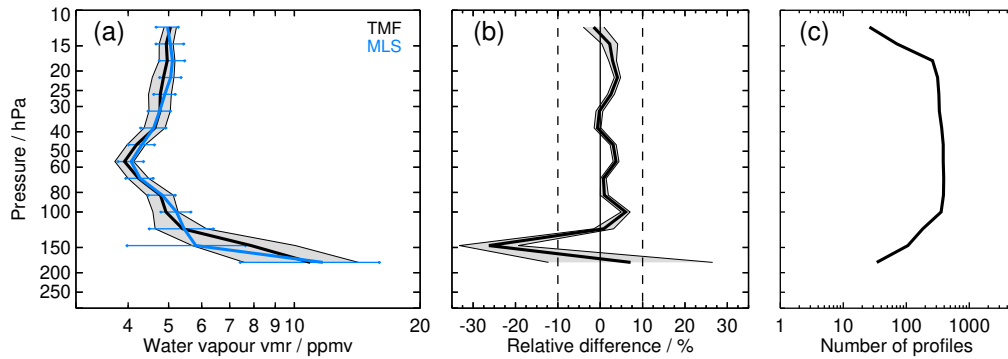


**Figure 4.** Comparison of MLS water vapour profiles with FP profiles at TMF; mean profiles over all coincidences are shown. The individual profiles were cut at the respective tropopause before averaging. Panel a: mean profiles (TMF: black, MLS: blue) and their standard deviations (grey shading for TMF and horizontal blue lines for MLS). Panel b: Relative mean bias and twice its standard error of the mean (grey shading,  $2\sigma_{\text{bias}}$ ), calculated as the mean differences SAT-FP divided by the mean FP profile and multiplied by 100; the vertical dashed lines enclose the  $\pm 10\%$  range. Panel c: number of data points along the vertical grid. This number can vary over the vertical range, depending on the altitude coverage of the individual coincident SAT and FP profiles, respectively.

part of the profiles, is high and provides the good accuracy of the bias determination. Similar figures for other SAT–FP pairings are provided in the supplement to this paper.

### 280 3.3 Mean biases of the satellite data records by FP stations

In the following, the comparison of all available satellite data records to one specific FP station is discussed. This comparison provides some insight into potential latitudinal dependencies of the satellite data records’ biases. Peculiarities specific for certain FP stations may also show up.

As an example for the comparison of all satellite data to one specific balloon sonde station, Fig. 5 presents the mean relative differences of all available satellite data records to the FP station at BLD ( $40^\circ$  N). All satellite records having collocations with BLD balloon soundings are shown in this comparison. The presentation is similar to the middle panel of Fig. 4, but for multiple satellites. For the color coding we refer to Fig. 2. The biases of the SAT data records are shown in two panels in order not to overload the figures. We follow Nedoluha et al. (2017) and separate the data sets in non-MIPAS and MIPAS satellite data.

We find that for most of the satellite data records, the bias with respect to the BLD FP data is less than 10% in the stratosphere between 100 hPa and the upper end of the FP soundings around 10 hPa. Between 100 hPa and the respective tropopause (i.e. the lower end of the profiles), the differences for some SATs become far larger, and for many tend to be negative. This is a typical behaviour that can be observed for many stations, mainly in the mid and high latitudes (see Appendix Figs. A4–A10). In the tropics, however, such a systematic behaviour of the biases is not obvious. Maybe this is because the profiles cut at the

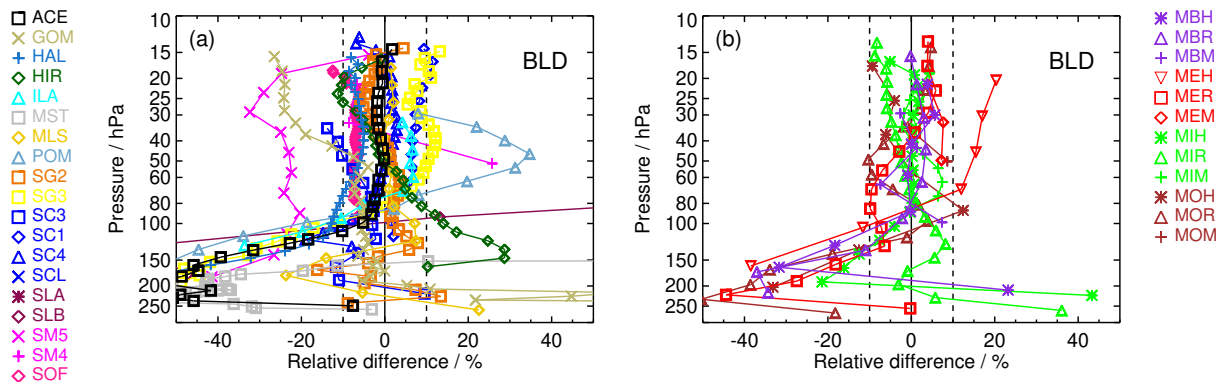


**Figure 5.** Mean relative differences between satellite and BLD FP profiles ( $40^{\circ}$  N). Panel a: all data records except MIPAS; panel b: all MIPAS data records. Details of color coding and symbols for the satellite records are provided in Fig. 2 and Tab. 2. The profiles were cut at the respective local tropopause before averaging.

local tropopause for tropical sites scarcely reach below 100 hPa (again, see figures in Appendix A2). It is currently unclear what causes these large deviations at the extra-tropical FP sites.

In case of the comparison to BLD soundings, we identify some large biases that more consistently exceed  $\pm 10\%$  in the stratosphere above 100 hPa. These are SM5 and GOM, which both show negative biases, and POM and MEH, showing positive biases. All other satellite data sets are largely within 10% relative difference to the BLD FP data above 100 hPa.

Fig. 6 presents an example for HIL ( $20^{\circ}$  N), a subtropical northern hemisphere station. Generally, we observe some of the same characteristics as for BLD. Due to the higher tropopauses at the lower latitude sites, the profiles contain little data at pressures  $> 100$  hPa. Nevertheless, the negative deviations from the FP data again become larger at the lower end of the profiles. SM5, GOM, HAL, SG2, SC3, MBR, MEH, MEM, MIH, MIM, MOH, MOM exhibit biases larger than 10% at multiple altitudes. The biases of the MIPAS data are mostly positive above 100 hPa.

The SAT data records that have large and repetitive biases identified in the BLD and HIL comparisons have larger deviations in most, if not all, FP stations, too. However, the comparisons to many FP stations having a smaller number of coincidences with SAT data due to shorter and/or less dense measurement records, have a large spread (not shown in the figures), and the bias determination is less accurate. In general, we can state that the satellite data records that perform well (i.e., virtually all biases  $< 10\%$ ) do so with FP stations having both large and small number of collocations. These are, in alphabetical order, ACE, HAL (except for the well-known 10% bias over the entire profile above 100 hPa, Randel et al. (2006); Scherer et al. (2008)), MIPAS ESA and IMK/IAA, MLS, SG2, SG3, SC1, SC4, and SOFIE (see Figs. A1–A3).

### 3.4 Mean biases of the satellite data by data record

Comparison of one satellite data set to several balloon sounding stations provides some insight on how the agreement between SAT and FP may be dependent on latitude. Fig. 7 provides, as an example, the comparison of HIR data to all FP stations for



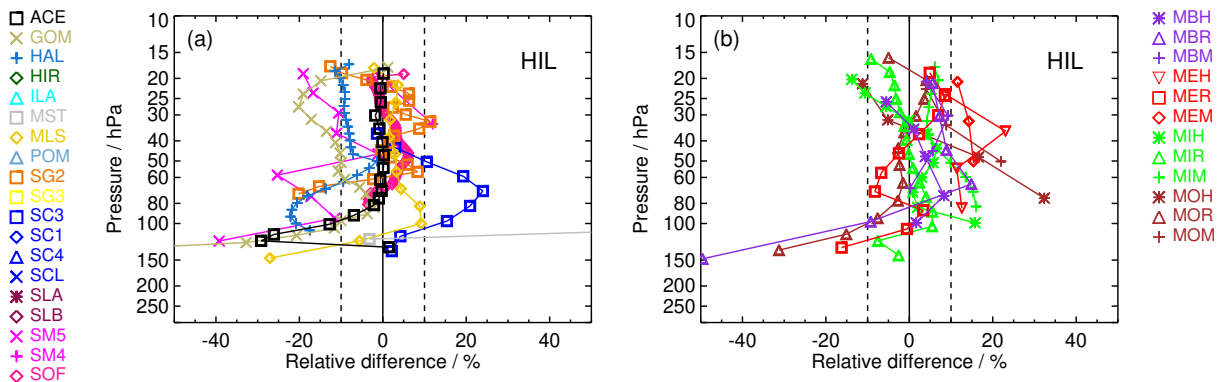


**Figure 6.** Same as Fig. 5 but FP profiles from HIL (20° N).

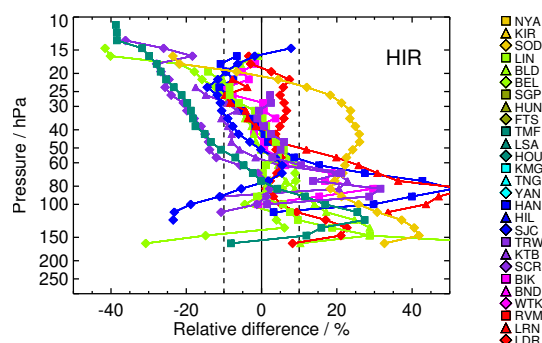


**Figure 7.** Mean relative differences between all the FP stations and the HIR satellite data record. The frost point hygrometer data were adjusted to the vertical grid and resolution of HIRDLS by a smoothing kernel, and the profiles were cut at the tropopause before averaging. Details of color coding and symbols for the FPs are provided in Fig. 1 and Tab. 1.

which coincident measurements were available (discussion, see below). Similar figures for all satellite data sets are presented in the appendix (Figs. A1–A3). In the following, we discuss the typical bias behaviour for all these satellite data sets.

### ACE-FTS v3.5 (ACE)

ACE (Fig. A1) is in the  $\pm 10\%$  range for most of the stations above 100 hPa. Larger negative deviations in this altitude range are found in the lower stratosphere for the southeast Asian stations LSA and KMG. At the upper end of the bias profiles, deviations are negative and the satellite data deviate by more than  $-10\%$  from stations BEL and TMF. The overall impression is that the ACE biases follow a bent curve with slight negative deviations at the upper end and stronger negative deviations at the lower end of the profiles, and shows excellent agreement with the frost point hygrometer profiles between approximately 20 and 80 hPa. For stations in the middle to high latitudes of the Northern hemisphere, where ACE has its densest sampling, the agreement with frost point hygrometer data is, with deviations within  $\pm 5\%$ , excellent (e.g. LIN, SOD). The uncertainties of the mean biases (in terms of twice the standard error of the mean,  $2 \cdot \text{SEM}$ ,  $2\sigma_{\text{bias}}$ ) are very small in the stratosphere between

325 100 and 30 hPa, leading to significant biases, at least in the middle to high latitudes, with the exception of BLD where the biases are small and insignificant. In the low latitudes, the uncertainties of the biases are larger, leading to insignificant biases between 60 and 30 hPa.

### **GOMOS (GOM)**

330 Deviations from frost point hygrometer data for GOM (Fig. A1) vary strongly and cover, except for the comparison to the HAN and the LDR stations, all the range between -40 % to 0 %. Above 100 hPa the biases have a tendency to be on the negative side, and to show increasingly larger negative values with increasing altitude. The comparison to the station data of LDR and HAN are significant outliers within this comparison, with large positive biases. The biases are all significant at the  $2\sigma_{\text{bias}}$  level, except for a few single points where the bias profiles show zero-crossings. The large spread between the stations indicate a significant latitude dependence of the GOMOS data which might be due to the different stars used as occultation light sources  
335 during measurement.

### **HALOE (HAL)**

For HALOE v19 data (Fig. A1), the well-known negative bias in the order of -10 %, seen in measurements after 2001 (Randel et al., 2006; Scherer et al., 2008) over large parts of the stratosphere is confirmed by the comparisons presented here. Except for some altitudes, at HUN, KIR, SOD, and SGP the deviations from the frost point hygrometers always stay on the negative  
340 side, with smallest deviations between -5 and -10 % in the 20 to 60 hPa range, and larger deviations of up to -30 % above and below. The biases are almost all significant, the only exceptions are rare zero-crossings of the bias profiles, for example for comparisons to the KIR station data. The compactness of the biases of all the stations indicates that HALOE data have a very similar performance over all covered latitudes and related atmospheric conditions.

### **HIRDLS (HIR)**

345 For most of the stations — with the exceptions of LDR and SOD — the comparison demonstrates a general positive to negative tilt in the bias with increasing altitude for HIR (Fig. A2): Obviously the HIR observations have a positive bias in the order between 0 to 40 % near 100 hPa and end with a similarly strong negative bias around 10 hPa. The difference with respect to the LDR balloon soundings is more or less constant between 0 and +10 % above 100 hPa, while the difference to SOD is roughly constant at about +25 % up to 30 hPa, and decreases to -20 % from 30 hPa to the upper end of the profile. Below 100 hPa, the  
350 biases show a wide spread with some focus around +20 %. The collection of mean difference profiles confirms that the tilted bias, from >20 % near the tropopause to <-20 % around 10 hPa is a distinct property of the HIRDLS water vapour observations. The  $2\sigma_{\text{bias}}$  uncertainties of the biases are small which makes the biases significant everywhere except near the zero-crossings of the bias profiles.

### **ILAS-II (ILA)**

355 ILA (Fig. A1), could be compared to three stations only; the agreement above 100 hPa is within  $\pm 10$  % for BLD and SOD,

while ILAS-II deviates from the frost point hygrometer soundings at NYA by -30 to -40 %. Below 100 hPa, the deviations cover the range between > -40 % and +30 %. The biases are all significant except near the zero-crossings of the bias profiles.

### **MAESTRO (MST)**

MAESTRO (Fig. A1) has very few measurements of water vapour above the tropopause. The bias profiles mostly change from  
360 -40 % at about 200 hPa to +40 % around 90 to 100 hPa, with large uncertainties, but nevertheless significant deviations. Since we are at the upper limit of MAESTRO's measurement range, we refer to a more appropriate comparison that is provided in a companion paper dealing with upper tropospheric humidity (Read et al., 2022).

### **MIPAS (MBR, MER, MIR, MOR)**

For MIPAS, all observation modes and data versions from the four processors are shown in Fig. A3. Above 70 hPa, the compar-  
365 ison to the frost point hygrometer data for the NOM RR modes remains within  $\pm 10\%$  for most cases. The MOR data set is the most compact one, with biases for most stations between +10 and -10 % for the altitude range of 80 to 20 hPa. Above 20 hPa, a tendency to larger negative biases exists, while below 80 hPa, the profiles develop an increasingly negative bias. The MOH data set is less compact, and it shows a pronounced high bias in the range of 70 to 100 hPa. The MOM data set has a bias > 10 % at the lower end of the profiles, and a smaller, almost zero bias at the upper end of the profiles. The MIR bias is also quite  
370 compact, however it has a rather pronounced tilt from positive values around +20 % near the tropopause to -10 to -20 % above 30 hPa. Again, for MIH the biases to the various FP sites are less compact, but follow in general the characteristics of the MIR data set. The biases for the MIM data set show S-shaped profiles with positive biases >+10 % at the lower and much smaller positive biases at the upper end, similar to MOM. For MER and MBR, the biases with respect to the frost point hygrometer stations have a somewhat larger scatter than that of MOR and MIR. Most of their biases remain between  $\pm 10\%$ , however,  
375 some prominent outliers below 60 hPa and above 20 hPa exist.

MBR biases for the Northern mid and high latitudes have mostly small uncertainties and are significant except near the zero-crossings of the bias profiles. In contrast, the number of comparisons for the low latitudes is lower, therefore the bias uncertainties are higher, leading very often to insignificant biases. For the LDR FP site (the only in the Southern mid to high latitudes), the biases above 100 hPa are small, and despite small uncertainties, they are insignificant. MER and MOR behave  
380 similar to MBR for all FP sites except LDR; deviations from the LDR FP measurements are larger than for MBR and they are significant over the full altitude range of the profiles. MIR biases are more often significant (although small) than for the other MIPAS data sets. In particular, in the tropics where the biases of the other MIPAS data sets often have higher uncertainties, the MIR biases are significant except for the region of the zero crossings of the profiles. The bias profile with respect to the LDR station is significant except in the troposphere below 200 hPa and at its zero crossing. The biases for MIPAS HR and MA  
385 observations have, in general, larger uncertainties, mainly due to the smaller number of coincidences, and are therefore more often insignificant. Very often, the biases are below  $\pm 10\%$  and the uncertainties are larger than that. Consistently significant biases can be found, in general, for larger biases. This is the case for MBH in the comparisons with Northern high and mid latitude stations, larger parts of the MEH profiles in all latitudes, and for all MIH and MIM biases that are larger than 2 or 3 %

(absolute). MBM biases are mostly not significant, while MEM biases mostly are. MOH and MOM behave very much like  
390 MEH and MEM in terms of significance of their biases.

### **MLS (MLS)**

MLS (Fig. A2) reveals a very compact set of biases that are almost all in the  $\pm 10\%$  range from 70 to 10 hPa. Exceptions are  
the comparisons to stations of the maritime continent, i.e. BIK, BND, Tawara, KTB, and RVM. For these stations, MLS shows  
a high bias up to  $+30\%$  in the altitude range of 100 to 70 hPa. Below 100 hPa, MLS tends to develop a low bias with a peak  
395 at  $-25\%$  around 200 hPa, and a better consistency to frost point hygrometer data, again in the  $\pm 10\%$  range, close to the local  
tropopause. In the Northern high and mid latitudes, the uncertainties of the biases are extremely small, leading to significant  
but small (mostly  $+5$  to  $10\%$ ) deviations from the FP data in the stratosphere above 100 hPa. Even in the low latitudes, the  
uncertainties are small enough to make most of the deviations significant, in particular the deviations from FP stations in the  
maritime continent. The bias with respect to the LDR FP site is below  $5\%$  above 70 hPa and significant, due to the extremely  
400 small uncertainty. The larger biases below 100 hPa are mostly significant, too.

### **POAM-III (POM)**

POM3, as an instrument covering the Northern high latitudes only, has coincidences with the most Northern stations NYA,  
SOD, KIR and BLD (Fig. A1). The biases to the three former stations are rather small, providing curved bias profiles with  
negative values around  $-20\%$  below 100 hPa and above 20 hPa, and positive values of up to  $+20\%$  between 100 and 40 hPa.  
405 The comparison with the sonde data of BLD gives a somewhat different picture: here the biases increase from extreme negative  
values beyond  $-40\%$  below 100 hPa to  $+35\%$  around 50 hPa and remain in the 10 to 35% range above. The hygropause in  
the POM3 profiles near BLD, i.e. the altitude with lowest water vapour vmr, is much lower than in the frost point hygrometer  
data, and the mean profile below the hygropause is displaced towards lower altitudes which both contribute to the increasingly  
larger negative bias below 100 hPa. All biases are significant except near the zero-crossings.

### **410 SAGE-II (SG2)**

SG2, as another instrument besides HALOE, providing water vapour observations for decades, has been used a lot for con-  
struction of longer-term global water vapour data time series. The comparisons to frost point hygrometer station data (Fig. A1)  
provide some scatter, however the most data points lie within  $\pm 20\%$  deviation, and a larger part also within  $\pm 10\%$ . The com-  
parisons to SOD form an exception with positive deviations of approximately  $25\%$  over a larger part of the stratosphere (90 to  
415 35 hPa). The number of coincidences, however, is very small (around 10) for this FP site. The uncertainties of the bias profiles  
are often in the order of  $\pm 5\%$  which makes some deviations in the Northern high and mid latitudes insignificant. The bias with  
respect to BLD FP observations, however, is significant in the stratosphere above 100 hPa despite the deviations being less than  
 $5\%$  over a large part of the profile. The same is true, although to a lesser part of the profile, for the comparison to the LDR  
FP site (the altitude near the zero-crossings of the profiles always excluded). For the low latitude FP sites, a general comment  
420 is difficult to make because of strongly oscillating bias profiles and sometime considerable uncertainties. Nevertheless, also in  
this latitude region significant biases can be found despite larger uncertainties.

### **SAGE-III (SG3)**

SG3 data (Fig. A1) could be compared to the most Northern stations (NYA, KIR and SOD), BLD and LDR only. The comparisons agree well, indicating a bias within the  $\pm 10\%$  range, with two outliers in the order of  $+20\%$  at about 70 and 15 hPa. 425 The comparison to the BLD balloon data indicates, similar to POM3, a too low lying hygropause and displacement towards lower altitudes of the profile part below as the reason for the increasingly large negative bias below 80 hPa. Uncertainties of the biases are small enough to make the biases significant over the full altitude range, except near the zero-crossings.

### **SCIAMACHY (SC3, SC1, SC4, SCL)**

The SC3 observations (Fig. A2) cover the altitude range from the tropopause up to approx. 30 hPa. Above 100 hPa, the comparisons to the FP stations provide a large scatter from  $-40\%$  to more than  $+50\%$ . The stations at the Maritime continent and the Indian ocean (pink, purple and partly red colours) seem to provide the highest positive biases, while for Northern midlatitude stations the biases tend to be in the  $\pm 10\%$  range and rather on the negative side. Near to the upper end of the SCIAMACHY profiles, around 30 hPa, the deviations to the sonde station data converge to a bias range of  $-20\%$  to  $+5\%$ , with only two outliers, and most of the biases within the  $\pm 10\%$  range. The biases with respect to the BLD FP site are significant below 150 hPa and 435 above 70 hPa. Other sites for which the biases turn out to be significant, at least over a large part of the profiles, are SOD, LIN, and SGP, all revealing negative biases. Biases for HIL, SJC, TRW, BIK, RVM, and LRN are significant for at least a part of the profile, and positive, while the comparison to LDR shows insignificant and rather small biases. The SC1 and SC4 data sets, both solar occultation observations, have in common that only stations from moderate to high northern latitudes contribute to the comparisons (Fig. A1). The SC1 relative biases are within  $\pm 10\%$  between 100 and 20 hPa, and above and directly below 440 this altitude range tend towards more negative values. Biases and uncertainties are rather small and in the same order of magnitude for KIR and NYA. Therefore the biases are largely insignificant. The other stations reveal significant biases. SC4 shows biases within  $\pm 10\%$  between 100 and 20 hPa for 4 out of 6 FP sites. Biases with respect to NYA and KIR, however, are at about  $10\%$  at 100 hPa, but decrease to about  $-20\%$  at 30 hPa. All biases except near the zero-crossings of the bias profiles are significant. The SCIAMACHY lunar occultation data set has coincidences with the FP station of LDR only (Fig. A1). The bias 445 for this site is between 10 and 20% and significant at all altitudes.

### **SMILES (SLA, SLB)**

The comparison of SMILES water vapour observations from their channel A and B (Fig. A2) to frost point hygrometer sonde data shows a large scatter, and prominent biases reaching from  $-40\%$  and more below 100 hPa to  $+40\%$  and more between 40 and 30 hPa. Due to the short mission lifetime of SMILES, the number of coincidences with frost point hygrometer soundings is, however, very limited. As a consequence, uncertainties of biases are rather large. Nevertheless, the biases are significant 450 except near the zero-crossings of the profiles.

### **SMR (SM5, SM4)**

SMR 544 GHz comparisons with frost point hygrometer data reveal a large scatter of the biases over  $\pm 40\%$  and more (Fig. A2). Most of the bias profiles are negative, and there seems to be a certain concentration of biases around  $-30\%$ . There is

455 no latitude dependence obvious. Despite the long lifetime of the SMR mission (which is still operational at the time of this writing) and its rather dense global coverage, the number of coincidences range between 10 and 100 for most of the stations only. The spread of the coincident SM5 profiles is, however, far larger than the spread of the frost point hygrometer profiles, indicating that the SM5 profiles have a considerable measurement error (see Fig. S29 in the Supplement). The SMR 489 GHz observations of water vapour are available above 50-60 hPa only. They are more compact than the 544 GHz observations, with  
460 biases between -20 and +20 %, and most data points falling into the  $\pm 10$  % range. However, for this observation channel, a much smaller amount of stations providing coincident balloon soundings is available, and the number of coincidences per station is often below 10. Therefore, the biases have often large uncertainties. Nevertheless, most of the biases are significant.

### **SOFIE (SOF)**

For SOFIE, comparisons with frost point hygrometer data from SOD, BLD, LIN, HIL, SJC, and LDR are available (Fig. A1).  
465 The comparisons to all frost point hygrometer data are very compact. Above 100 hPa, almost all data points of the biases fall into the  $\pm 10$  % range, and many of them are even closer than  $\pm 5$  % to the frost point hygrometer data. The uncertainties are small, making even the tiny deviations from FP measurements at BLD or LDR significant.

### **3.5 Synopsis of the bias assessment**

For the overall assessment of biases of SAT records against FP profiles we have averaged the results from all stations in each  
470 of the following three pressure ranges: tropopause to 100 hPa, 100 to 30 hPa, and 30 to 10 hPa. The average biases and their standard errors were calculated with Eqs. 9 and 11, respectively. They are listed in Tables 3 and 4. In Fig. 8 thick horizontal bars show average biases plus/minus twice the respective standard errors to indicate the 95 % confidence limits. Additionally, the 5- % and 95- % percentile values are marked in the plots and listed in the tables.

In the 10–30 hPa altitude range, most of the satellite data records have mean biases within the  $\pm 10$  % range, and some of  
475 them show even better overall agreement with the FP data. ACE, MLS, SG2, SG3, SC1, SC4, and SOF have very accurately determined biases of smaller than  $\pm 5$  %. Data records with mean biases larger than  $\pm 5$  % but less than  $\pm 10$  % are HAL, POM, and SM4. For all three, the bias accuracy is very good. Data records with biases larger than  $\pm 10$  % are ILA, MST, SLA, SLB, SM5, GOM, and HIR. Except for MEM and MIH, the MIPAS data records are all within the  $\pm 10$  % range regarding their bias in the 10 to 30 hPa altitude range with the majority of these being within the  $\pm 5$  % range. The three ESA data products have  
480 all a positive bias, while the three IMK/IAA data records have all a negative bias. Except for the ESA product, water vapour derived from the MIPAS middle atmosphere measurement mode shows agreement with FP data of better than 5 %.

In the altitude range of 30–100 hPa, HIR, SG2, SG3, SOF, SM4, SLB, SC3, SC4, SC1, ACE, and MLS have biases less than  $\pm 5$  %. However, SM4 and SLB have very large uncertainties of the biases. HAL and ILA have biases less than  $\pm 10$  %. POM, GOM have biases just greater than 10 % in the 30 to 100 hPa altitude range, while the biases of SM5, SLA, and MST  
485 far exceed 10 %. Except MOM, MEM, and MEH, MIPAS data sets fall into the  $\pm 10$  % bias range. MOR, MOH, MBR, MBH, MER, MIR, and MIH show even biased lower than  $\pm 5$  %.

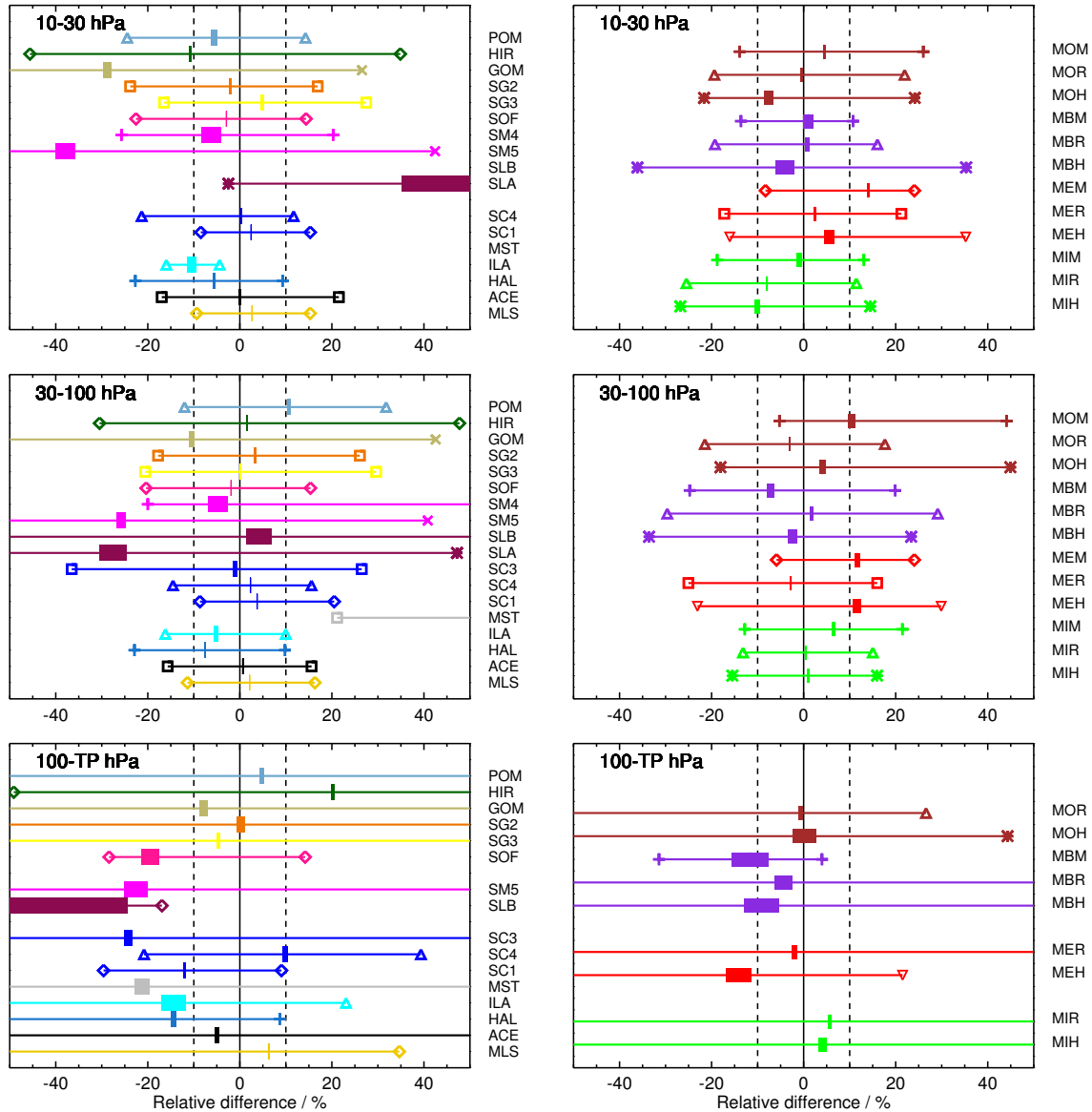


**Figure 8.** Relative differences of satellite and FP data averaged over all sites and the three pressure ranges 10–30 hPa (top row), 30–100 hPa (middle row), and 100 hPa to tropopause (bottom row). The panels on the left show comparisons for all satellite instruments except MIPAS. In the right column all MIPAS comparisons are displayed. For color coding and symbols see Fig. 2. Thin lines between symbols span the 5–95 % range of the data, while thick bars indicate the range of twice the standard errors ( $2 \times \text{SEM}$ ) around the mean biases. The actual average bias values are given by the center of the thick bars. For the 10–30 hPa panel, SMB and MST biases and the 5–95 % range of data are completely beyond the relative difference scale (see Table 3 for the actual values).

**Table 3.** Tabulated data used in the left columns of Fig. 8 for the non-MIPAS data sets. 100–TP means the pressure range from 100 hPa down to the tropopause. Statistically significant biases are presented in boldface text. Note that the column “Rel. std.err.” does not give the relative value for  $2 \times \text{SEM}$  used for the plots in Fig. 8, but only the relative value for the SEM.

SAT label	P range / hPa	Rel. bias / %	Rel. std.err. / %	5-% percentile	95-% percentile
ACE	10–30	-0.026	0.144	-16.971	21.514
	30–100	<b>0.638</b>	0.065	-15.678	15.584
	100–TP	<b>-5.013</b>	0.209	-380.964	117.333
GOM	10–30	<b>-28.762</b>	0.434	-74.006	26.549
	30–100	<b>-10.539</b>	0.279	-62.126	42.556
	100–TP	<b>-7.969</b>	0.441	-128.002	104.097
HAL	10–30	<b>-5.606</b>	0.146	-22.702	9.299
	30–100	<b>-7.520</b>	0.080	-22.894	9.806
	100–TP	<b>-14.403</b>	0.284	-267.165	8.682
HIR	10–30	<b>-10.836</b>	0.121	-45.594	34.876
	30–100	<b>1.509</b>	0.061	-30.474	47.731
	100–TP	<b>20.139</b>	0.188	-49.116	101.612
ILA	10–30	<b>-10.512</b>	0.472	-15.973	-4.401
	30–100	<b>-5.160</b>	0.238	-16.187	9.974
	100–TP	<b>-14.386</b>	1.304	-56.345	23.072
MST	10–30	<b>261.870</b>	51.987	158.897	2602.118
	30–100	<b>105.646</b>	1.795	21.137	383.422
	100–TP	<b>-21.142</b>	0.793	-217.222	168.084
MLS	10–30	<b>2.634</b>	0.043	-9.359	15.280
	30–100	<b>2.147</b>	0.022	-11.376	16.314
	100–TP	<b>6.257</b>	0.058	-150.251	34.656
POM	10–30	<b>-5.568</b>	0.325	-24.457	14.260
	30–100	<b>10.644</b>	0.191	-12.016	31.779
	100–TP	<b>4.689</b>	0.236	-99.721	179.944
SG2	10–30	<b>-2.113</b>	0.152	-23.830	16.922
	30–100	<b>3.387</b>	0.149	-17.764	26.080
	100–TP	0.121	0.447	-111.409	56.102
SG3	10–30	<b>4.824</b>	0.160	-16.489	27.473
	30–100	0.138	0.092	-20.543	29.615
	100–TP	<b>-4.751</b>	0.181	-175.203	92.155
SC3	30–100	<b>-0.975</b>	0.232	-36.536	26.485
	100–TP	<b>-24.304</b>	0.466	-106.064	64.791
SC1	10–30	<b>2.440</b>	0.046	-8.474	15.293
	30–100	<b>3.769</b>	0.029	-8.665	20.503
	100–TP	<b>-12.099</b>	0.103	-29.608	9.048
SC4	10–30	<b>0.238</b>	0.077	-21.325	11.679
	30–100	<b>2.327</b>	0.044	-14.521	15.566
	100–TP	<b>9.746</b>	0.286	-20.819	39.344
SLA	10–30	<b>45.905</b>	5.340	-2.487	82.150
	30–100	<b>-27.460</b>	1.469	-231.510	47.187
SLB	10–30	<b>160.216</b>	9.478	131.965	522.533
	30–100	<b>4.142</b>	1.394	-185.750	202.804
	100–TP	<b>-60.679</b>	18.084	-174.678	-16.925
SM4	10–30	<b>-6.263</b>	1.073	-25.716	20.280
	30–100	<b>-4.710</b>	1.055	-20.002	64.179
SM5	10–30	<b>-37.846</b>	1.047	-79.713	42.433
	30–100	<b>-25.821</b>	0.486	-72.709	40.834
	100–TP	<b>-22.650</b>	1.261	-160.116	107.726
SOF	10–30	<b>-2.923</b>	0.046	-22.563	14.389
	30–100	<b>-1.906</b>	0.044	-20.371	15.347
	100–TP	<b>-19.456</b>	0.970	-28.404	14.192



**Table 4.** Tabulated data used in the right columns of Fig. 8 for the diverse MIPAS data sets. 100–TP means the pressure range from 100 hPa down to the tropopause. Statistically significant biases are presented in boldface text. Note that the column “Rel. std.err.” does not give the relative value for  $2 \times \text{SEM}$  used for the plots in Fig. 8, but only the relative value for the SEM.

SAT label	P range / hPa	Rel. bias / %	Rel. std.err. / %	5-% percentile	95-% percentile
MBH	10–30	<b>-4.094</b>	1.003	-36.112	35.307
	30–100	<b>-2.386</b>	0.495	-33.585	23.368
	100–TP	<b>-9.228</b>	1.900	-236.371	62.386
MBM	10–30	1.043	0.566	-13.619	10.737
	30–100	<b>-7.233</b>	0.378	-24.762	19.895
	100–TP	<b>-11.620</b>	2.010	-31.430	3.986
MBR	10–30	<b>0.784</b>	0.250	-19.268	16.029
	30–100	<b>1.690</b>	0.174	-29.630	29.141
	100–TP	<b>-4.344</b>	0.969	-221.124	78.809
MEH	10–30	<b>5.630</b>	0.535	-16.050	35.212
	30–100	<b>11.597</b>	0.413	-23.067	29.887
	100–TP	<b>-14.034</b>	1.376	-116.286	21.503
MEM	10–30	<b>14.065</b>	0.111	-8.291	24.056
	30–100	<b>11.649</b>	0.301	-5.897	24.034
MER	10–30	<b>2.424</b>	0.155	-17.250	21.233
	30–100	<b>-2.766</b>	0.095	-25.041	15.995
	100–TP	<b>-1.983</b>	0.260	-152.016	51.576
MIH	10–30	<b>-10.083</b>	0.274	-26.791	14.477
	30–100	<b>1.105</b>	0.151	-15.490	15.954
	100–TP	<b>4.162</b>	0.456	-84.822	54.517
MIM	10–30	<b>-1.044</b>	0.269	-18.790	13.070
	30–100	<b>6.569</b>	0.180	-12.795	21.461
MIR	10–30	<b>-7.997</b>	0.102	-25.466	11.439
	30–100	<b>0.398</b>	0.053	-13.176	15.017
	100–TP	<b>5.608</b>	0.159	-68.337	78.580
MOH	10–30	<b>-7.522</b>	0.472	-21.631	24.156
	30–100	<b>4.056</b>	0.358	-18.068	44.929
	100–TP	0.252	1.251	-89.854	44.318
MOM	10–30	<b>4.440</b>	0.121	-13.914	25.995
	30–100	<b>10.517</b>	0.363	-5.259	44.089
MOR	10–30	<b>-0.495</b>	0.154	-19.394	21.946
	30–100	<b>-3.035</b>	0.078	-21.461	17.647
	100–TP	<b>-0.714</b>	0.225	-194.747	26.589

In the tropopause to 100 hPa altitude range, the biases, and especially the data spread, become large for many of the SATs. Data records with biases below  $\pm 10\%$  are POM, GOM, SG2, SG3, SC4, ACE, and MLS. Of these, POM, SG2, and SG3

show biases below  $\pm 5\%$ . ACE just misses this value. For the MIPAS data sets, MOR, MOH, MBR, MBH, MER, MIR, and  
490 MIH are within  $\pm 10\%$  bias. MOR, MOH, MBR, MER, and MIH even stay within the  $\pm 5\%$  range. For all data records, the  
uncertainties of the biases increase compared to the other altitude ranges.

#### 4 Assessment of drifts in satellite-FP differences

Linear temporal trends in the relative differences between stratospheric water vapour mixing ratios reported for satellite (SAT)  
and frost point hygrometer (FP) measurements are hereinafter referred to as “drifts”, expressed in units of  $\% \text{ yr}^{-1}$ . Relative  
495 differences in SAT and FP mixing ratios ( $100\% \times (\text{SAT} - \text{FP}) / \text{FP}$ ) were calculated using FP mixing ratios as the divisors. As the  
bias analyses above, this investigation of drifts is based on FP and satellite-based profile measurements that are coincident in  
space and time according to the criteria provided in Section 2.2. Also analogous to the bias evaluations, before comparing to  
SAT profiles, the vertical resolution of each FP profile was degraded to that of the corresponding satellite’s reporting levels and  
placed on its grid of reporting pressures (i.e., convolved) using satellite-specific averaging kernels or more generic Gaussian-  
500 shaped smoothing kernels (see Section 2.3 and Table 2). To minimise the influences of tropospheric air on this evaluation of  
stratospheric measurements, the reporting levels of SATs were limited to those above the local tropopause (Section 2.2). Similar  
analyses of biases and drifts between SAT and FP measurements of tropospheric water vapour have already been published by  
Read et al. (2022).

Several of the methods employed here to evaluate drifts are slightly different from those used above for the bias analyses.  
505 In cases where multiple profiles from a given SAT were identified as coincident with a FP profile (a “coincident cluster”), the  
median SAT mixing ratio and standard error of the mean SAT mixing ratio were calculated for each cluster, as was done in  
Hurst et al. (2014). The convolved or smoothed FP mixing ratio profile (see Section 2.3) was then subtracted from the median  
SAT mixing ratio profile. The advantage gained using median mixing ratios instead of averages is that they are much more  
resistant to skew by statistical outliers. The SAT – FP mixing ratio differences (in ppmv) were divided by the FP mixing ratios,  
510 then multiplied by 100% to produce the SAT – FP relative differences analysed here. For each unique pair of FP sites and  
satellites, the drift at each SAT reporting level was independently determined using a weighted linear regression fit to the time  
series of SAT – FP relative differences, with statistical weights based on the standard error of the mean SAT mixing ratio for  
each coincident cluster.

##### 4.1 Evaluation of data records for drift analysis

515 Unlike the bias evaluations, an analysis of drift in SAT – FP relative differences requires a sufficient number of differences  
over an adequately long period of time to detect and determine statistically robust trends. The unique pairs of SATs and FPs  
evaluated for biases (see Tables 1 and 2) included many with short and/or sparse time series of relative differences. Typically,  
the statistical uncertainties of drifts determined for these pairs were large and the calculated drifts were very sensitive to the  
removal of one data point from the time series. Simple tests of drift uncertainties and sensitivities for time series with varying  
520 lengths and data densities were performed. The results revealed that robust drift statistics were consistently produced for time

series >5 years in length and composed of at least one difference in 67% of the years covered. Of all the unique SAT – FP pairs analysed for biases, only 64 provided difference time series that met these more stringent criteria for drift analysis. This excluded several time series >5 years in length but with only short-term “bursts” of FP data from intensive measurement campaigns.

525 Table 1 identifies the seven FP sounding sites that paired with SATs to provide at least one time series of differences that met the record length and data density criteria. Table 2 identifies the 20 SAT retrievals that paired with FP sites to produce at least one qualifying time series. Of these 20 SAT retrievals, 8 were for MIPAS, 3 for SCIAMACHY, 2 for SMR and one each for 7 other SATs. In total, 1146 time series of SAT – FP relative differences were analysed for drift at each SAT reporting pressure ranging from 275 to 13.1 hPa. These time series are based on several thousand satellite profiles and just over 900 unique FP  
530 profiles over 7 sites.

The numbers of reporting levels for each unique SAT–FP pair that met the drift analysis criteria are presented in Tables 5 and 6. Each SAT–FP pair provided difference time series at an average of 18 reporting levels over an average of 3 FP sites, though the individual coverages ranged widely from 1 to 74 reporting levels and 1 to 7 sites. For example, MIPAS Bologna V5R v2.3 MA (“MBM”) retrievals produced only a single qualifying time series of differences at 43 hPa over the BLD site,  
535 while MAESTRO (“MST”) retrievals produced qualifying difference time series at an average of 50 reporting levels over each of 4 FP sites. Since the records for HAL and SG2 extend only 5–6 yrs into the new millenium, they overlap adequately only with the the FP record at BLD. The MLS is the only SAT that paired with all 7 FP sites.

## 4.2 Methods for quantifying drifts

Each time series of SAT – FP differences was examined for statistical outliers by performing a preliminary standard linear  
540 regression analysis. Data points with residuals from the fit line that were >2.5 times the mean of the absolute values of the residuals were omitted from further analysis. This method of outlier filtering removed an overall average of 5.7% of the data points from the time series before they were analysed for drift.

Drifts in SAT – FP differences were determined using weighted linear regression analyses (Fig. 9). The weight  $W_i$  applied to each difference was computed as the squared reciprocal of its uncertainty (Eq. 12). The uncertainty  $\lambda_i$  of each difference  
545 was calculated (in quadrature) from the relative standard error ( $\sigma_i$ ) of the mean mixing ratio of the “coincidence cluster” of satellite profiles (in %) and the  $\pm 6\%$  uncertainty of stratospheric water vapour measurements by FPs (Hall et al., 2016; Vömel et al., 2016). Each fitting weight was then scaled to the 95% level of confidence using the student-t value for the number ( $n - 1$ ) of satellite profiles in each coincidence cluster. In this way, differences with smaller uncertainties had greater weights and therefore stronger influences on the linear regression fits.

$$550 \quad W_i = \lambda_i^{-2}, \text{ where } \lambda_i = t_{0.95,i} \sqrt{\sigma_i^2 + 0.06^2} \quad (12)$$

SAT – FP differences based on only a single coincident satellite profile (a rare occurrence) were assigned the smallest weight calculated for the entire time series. Consequently, these single profile differences had the weakest influence on the linear regression analyses of drift.

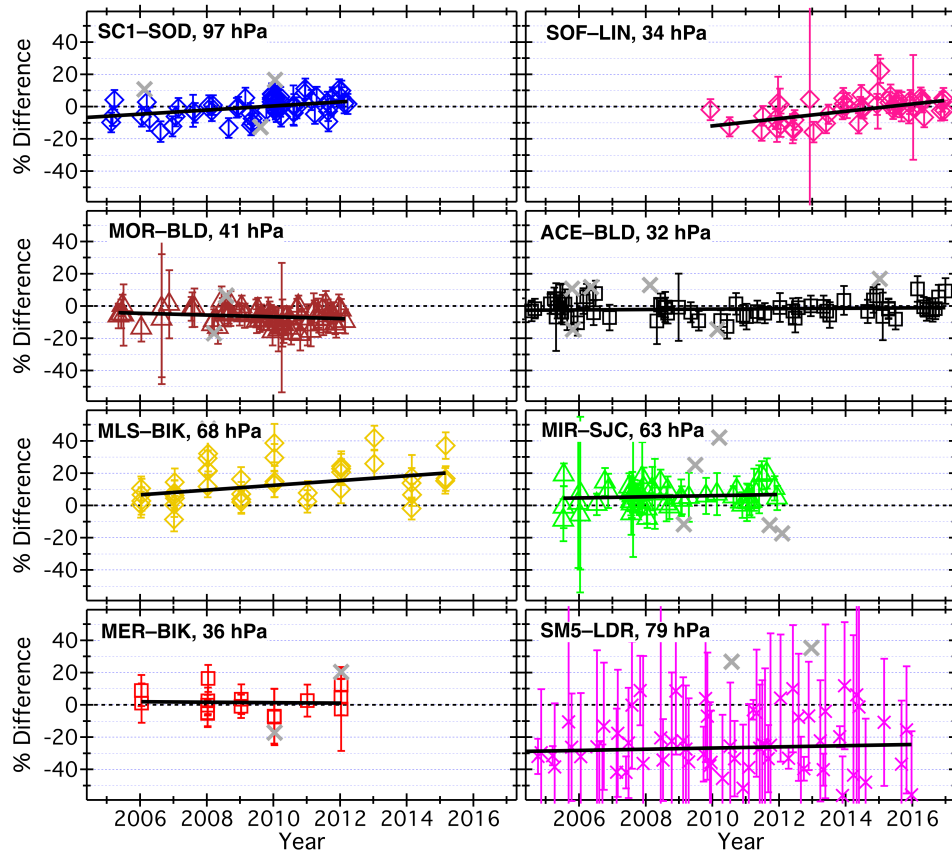


**Figure 9.** Time series of SAT-FP relative differences for 8 unique pairs of satellite retrievals and FP sites. See Tables 1 and 2 for the 3-letter codes that represent the relevant FP sites and satellite retrievals. The SAT reporting pressure for the time series shown is given in each panel. Vertical error bars depict the uncertainties in SAT-FP differences that factor into the weighted linear regressions used to calculate the black trend lines. Gray crosses are data points identified as outliers and omitted from the analyses.

The slope of the weighted regression fit line for each time series of relative differences was utilised as the best statistical estimator of the linear temporal drift ( $\% \text{ yr}^{-1}$ ) in the differences. Similarly, the 95% confidence limits of calculated slopes were considered the best estimates of drift uncertainty and thus used to evaluate the statistical significance of the drifts. In this analysis, a drift in SAT – FP differences at a given reporting pressure is considered to be statistically significant if the 95% confidence interval of the regression line slope does not include zero.

The vertical profiles of drifts determined for 4 unique SAT-FP pairs (Figs. 10) and all SAT-FP pairs (Figs. B1–B5) illustrate how the 95% confidence intervals determine statistical significance. In these plots, if the 95% confidence interval (full span of the error bar) does not intersect the vertical line for zero drift, the drift is labeled significant. Red (blue) markers indicate the statistical significance (non-significance) of the drifts at all reporting pressures. Fig. 10 also shows that the reporting pressures

for some SAT – FP pairs span only very limited ranges (e.g., 100 – 15 hPa for SOF at LIN), while those for other pairs cover much wider intervals (e.g., 196 – 18 hPa for MIR at BLD). The ranges of reporting pressures were typically smaller over tropical FP sites because their tropopause cut-offs were at lower pressures than the extratropical sites.

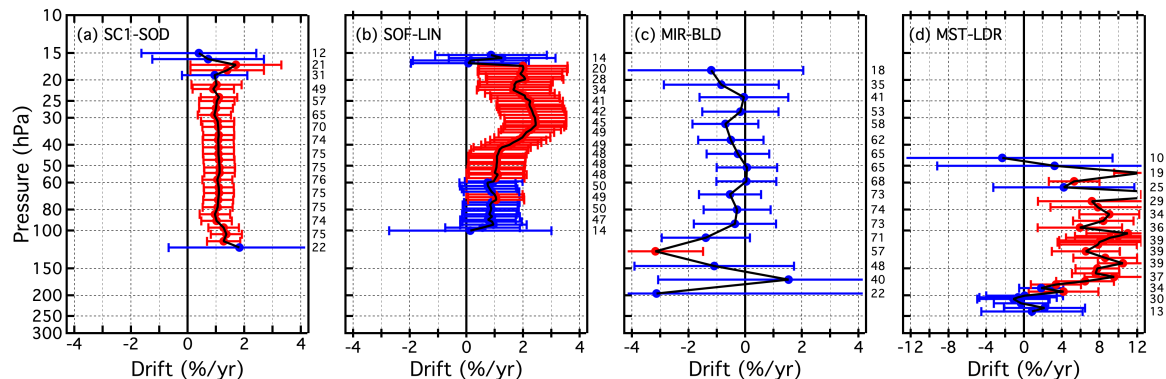


**Figure 10.** Vertical profiles of drifts (filled circles) and their 95 % confidence intervals (horizontal error bars) for 4 different SAT-FP pairs. Blue error bars denote drifts that are not significantly different from zero, while red error bars indicate statistically significant drifts. Numbers in black text to the right of each panel present the number of SAT-FP differences in the time series analyzed for drift at the corresponding pressure levels. Note that the x-axis scale is different for panel d.

#### 4.2.1 Special case of MLS drifts

The data, trend lines and correlation coefficients produced by weighted linear regression fits of all 1146 SAT – FP difference time series were visually checked for consistency and quality. The abnormalities most often revealed were the poorer fits (and lower correlation coefficients) associated with MLS – FP differences over most of the FP sites. Visually, many of the  
 570 MLS – FP time series show little or no evidence of drift until  $\sim 2010$ , after which positive trends in the differences become readily apparent (Fig. 11). These positive, post-2010 drifts in MLS – FP differences were previously reported from similar drift evaluations above the BLD, HIL, LIN, LDR and SJC sites (Hurst et al., 2016).

The alternative methodology used here, analogous to that described by Hurst et al. (2016), is a piecewise continuous weighted linear fitting procedure for each time series of relative MLS – FP differences. The fitting algorithm divides each time series  
 575 into two distinct periods by identifying the point in a record when a statistically significant change in the trend occurred, the “change point” as described by Lund and Reeves (2002). The optimal change point is the date for which linear fits before and after it yield the smallest root mean square (RMS) of residuals. In the case of MLS – FP differences, the piecewise continuous weighted linear fits substantially improve the “goodness of fit” for each time series (Fig. 11). Compared to the full time series regression fits of MLS – FP differences, the two-piece linear fits decrease the RMS of residuals at each of the 5 FP sites by 1 to  
 580 8%, with an average reduction of 4%. For the MLS – BIK time series, no statistically significant change points were identified because the FP record at BIK is dominated by data obtained during intensive but short-lived, annual measurement campaigns

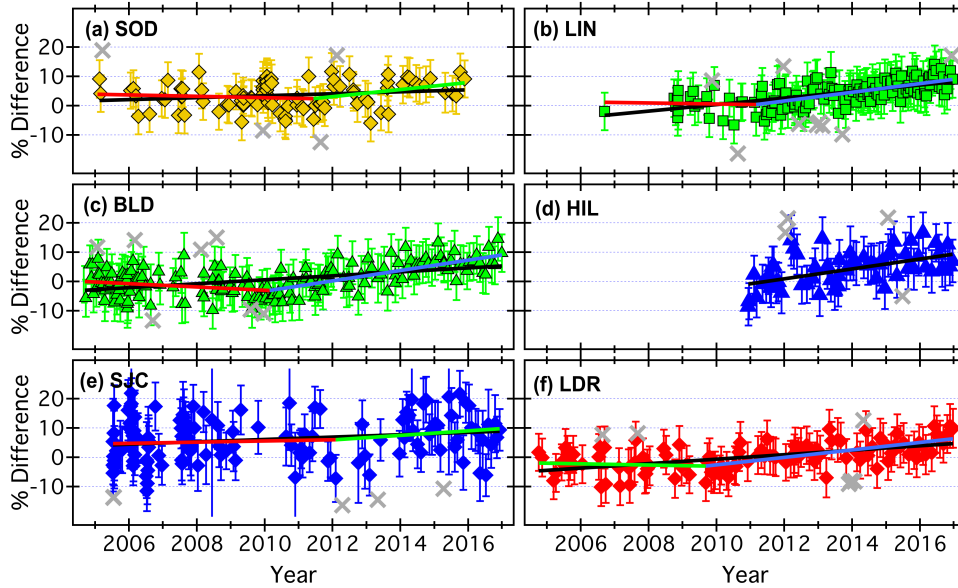


**Figure 11.** Time series of relative MLS-FP differences at 68 hPa over 6 different FP sites. As in Fig. 9, vertical error bars represent the uncertainties in differences and gray crosses are data points identified as outliers and omitted from the drift analyses. Black lines depict the trends determined by weighted linear regression fits to the entire records of differences. Colored lines show the linear trends in two distinct time periods (except at HIL) that are separated by a statistically significant change point, as determined by piecewise continuous weighted linear regression fits (see section 4.2.1).

(Fig. 9). For HIL, the records of MLS – HIL differences lack adequate data before  $\approx 2010$  for the time series to be analysed by this method (Fig. 11). The piecewise continuous fits were therefore performed only on the MLS – FP time series at SOD, LIN, BLD, SJC and LDR. The drifts and other statistics reported for the post-change point fits to MLS – FP difference time series are denoted by the SAT code MLS\*.

MLS retrievals at 31 of 70 pressure levels (44%) in the 121 – 18 hPa range over 7 FP sites exhibited full-record drifts that are positive and statistically significant (Fig. 12). When piecewise continuous linear fits were performed on the same MLS-FP differences, excluding those at HIL and BIK, pre-change point drifts were positive and statistically significant at 4 of the 52 (8%) reporting levels (Fig. 12b), while 46 of the 52 (88%) post-change point drifts were significant and positive (Fig. 12c). The vast majority (90%) of the positive post-change point MLS\* drifts were stronger than the full record MLS drifts (Fig. 12). For MLS reported pressures from 68 to 22 hPa over all FP sites except HIL and BIK, post-change point drifts were an average  $\pm\sigma$  of  $2.4 \pm 1.0$  times stronger than full record drifts. Though the piecewise fits better represent the MLS – FP time series and reduce the RMS of residuals compared to full- record fits, their uncertainties are larger than for the full-record drifts because the pre- and post-change point records have substantially smaller data populations.

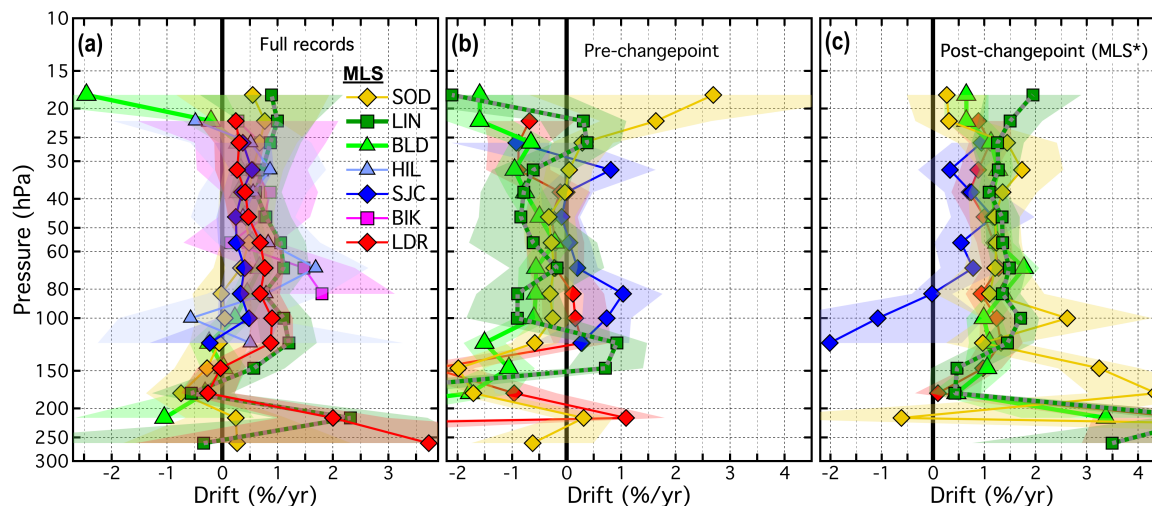


**Figure 12.** Vertical profiles of drifts in (a) MLS-FP differences spanning the entire records (2004–2016), (b) for the 2004 to  $\approx$ 2010 pre-changepoint period, and (c) for the  $\approx$ 2010 through 2016 post-changepoint period (i.e., MLS\*). The legend applies to all three panels, but drifts at HIL and BIK are not available for panels (b) or (c). The colored-matched shading surrounding each profile represents the 95% confidential intervals of the drifts over that site.

### 595 4.3 Drift profiles for the unique SAT-FP pairs

The drifts determined for all 21 SATs (MLS\* included), each paired with 1 to 7 FP sites, are presented as vertical profiles in Fig. 13 and in Figs. B6 and B7. Similarly, Figs. 14 and B8–B9 show the drifts of all paired SATs at each of the 7 FP sites. Both sets of figures are analogous to Fig. 10 except each panel of Fig. 13 shows the drifts of a unique SAT over multiple FP sites using the coloured symbol scheme from Fig. 1, while each panel of Fig 14 shows the drift profiles of multiple SATs over each FP site using the coloured symbol scheme from Fig. 2. In some panels of Figs. 13, B6, and B7, the colours and symbols for some SAT – FP pairs were slightly adjusted to help differentiate between the drift profiles at specific FP sites, for example LIN and BLD. Another modification to Figs. 13, B6, and B7 is that the 95% confidence intervals are represented by shaded, symmetric envelopes that match the colours of the drift profile markers and connecting lines. For some SATs the drifts were relatively uniform with pressure while the drifts of others were much more variable. Note that the reporting pressure for some SATs are the same for each FP site while for other SATs they are not.

There is a general tendency for the uncertainties of drifts to broaden at the extremes of the reporting pressure ranges. This often occurred because there were sharp drop-offs in data populations of the difference time series at the highest and lowest pressures, and therefore fewer data points for the weighted regression fits. Two factors affecting uncertainties at the high and low pressure ends of drift profiles are the annual cycles in extratropical tropopause pressures that reduce the data populations

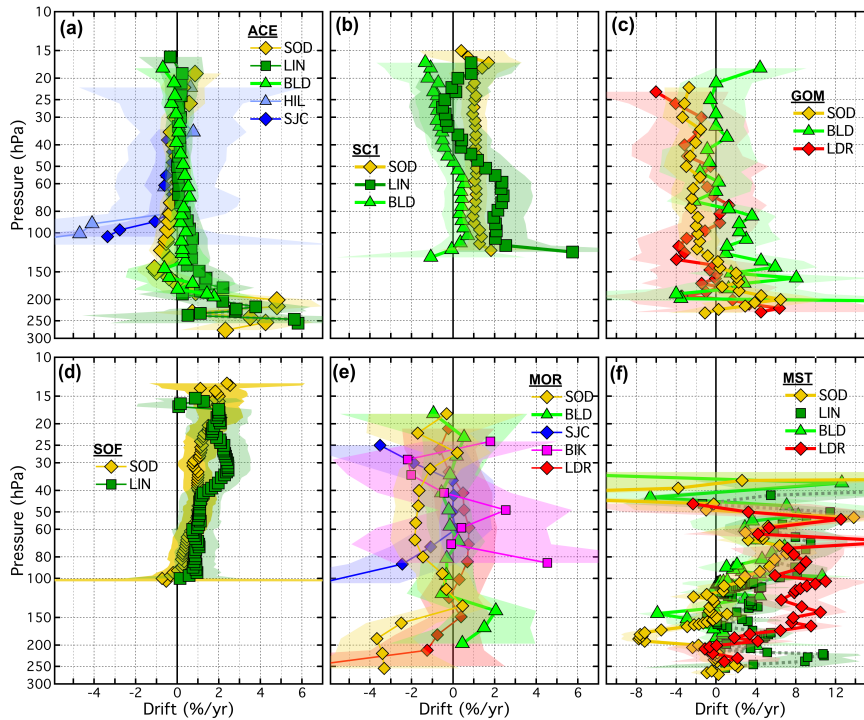


**Figure 13.** Vertical profiles of drifts in SAT-FP differences. Each panel displays the drifts for one SAT paired with 2-5 different FP sites. Drifts over each FP site (connected colored markers) are presented with their 95 % confidential intervals (colored-matched shading). Shading that does not cross the black vertical line at 0 % drift indicates drifts that are statistically significant. Note that the x-axis scale for the far right column is expanded to show the drifts with greater clarity.

610 at the highest reporting pressures during summer months, and the altitude ceilings of balloon-based FP profiles that limit data populations at the lowest reporting pressures.

Of the 21 different SATs analysed here, some have drift profiles over multiple FP sites that are statistically equivalent when the drift uncertainties are considered. For example, the ACE drift profiles  $\leq 85$  hPa are statistically the same over all 5 FP sites (Fig. 13a). Drift profiles for SC1 (Fig. 13b) at LIN and BLD also statistically overlap over their entire pressure ranges, although  
 615 the drifts  $\geq 51$  hPa are significant over LIN but not BLD. Drifts for SOF over SOD and LIN (Fig. 13d) also statistically overlap over their entire pressure ranges, with all drifts in the 58–17.2 hPa interval over both sites being positive and significant. Drift profiles for SATs at other FP sites are not always statistically the same, as exemplified by the absence of statistical overlap in SC1 drifts at 10 reporting levels over SOD and BLD in the 45 – 23 hPa interval (Fig. 13b), MST drifts at 6 reporting levels (170–140 hPa) over SOD and BLD (Fig. 13f) and SC4 drifts at 4 levels (35–25 hPa) over SOD, LIN and BLD (Fig. B7d).

620 Given the vertical profiles of drifts in Figs. 12, 13 and 14, plus those provided in the appendix (Figs. B1–B9), it is evident that a few SATs exhibit statistically significant drifts at many reporting levels over multiple FP sites. Of the 1213 time series of



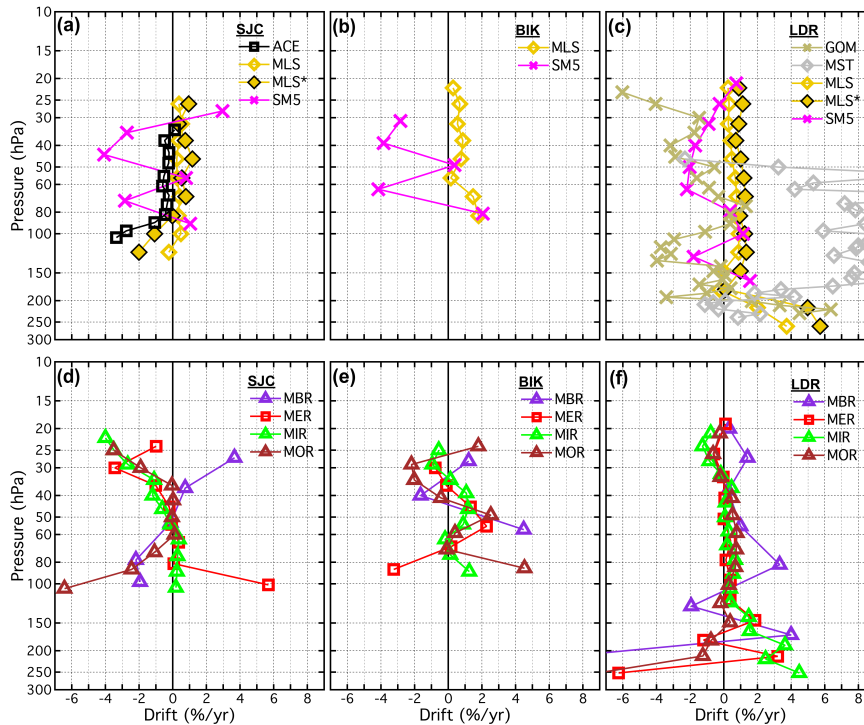


**Figure 14.** Vertical profiles of drifts in SAT-FP differences. Each panel displays the drifts for the multiple SATs paired with each FP site. Profiles for non-MIPAS SATs appear in the top row and for MIPAS SATs appear in the bottom row. Drifts for each SAT are represented by unique coloured markers according to Fig. 2. MLS\* refers to drifts in MLS from ~2010 through 2016, as discussed in Section 4.2.1.

SAT-FP differences analyzed here for drift (includes analyses of MLS\*), 419 (35 %) of the drifts were statistically significant. Of the 21 SATs examined here, MLS\* and SOF had the highest percentages of reporting levels (84 % and 70 %, respectively) with statistically significant drifts over their associated FP sites. The percentages for 4 other SATs were >40 %: MST (47 %), SC1 (46 %), SC4 (41 %) and MLS (41 %). Overall, these 6 SATs were associated with 339 (81 %) of the 419 statistically significant drifts.

Though the identification of statistically significant drifts is an important result, a more critical metric is the strength of a drift, as this limits the utility of a satellite data set when trying to detect temporal trends in stratospheric water vapor. For this work, a drift of  $-1 \text{ \% yr}^{-1}$  ( $\approx -0.5 \text{ ppmv decade}^{-1}$  in the middle stratosphere) in a data set would either completely mask a real trend of  $+0.5 \text{ ppmv decade}^{-1}$  or double a real trend of  $-0.5 \text{ ppmv decade}^{-1}$ , effectively rendering the data set unusable for detecting a trend of this magnitude. With this in mind, we focus on identifying statistically significant drifts with magnitudes  $> 1 \text{ \% yr}^{-1}$ , which are hereinafter called “large significant drifts”.

For many SATs, the numbers of large significant drifts are nearly as great as their numbers for statistically significant drifts. Overall, large significant drifts were identified for 349 (29 %) of the 1213 difference time series. Percentages of large significant

635 drifts were again greatest for MLS\* (63 %) and SOF (56 %), followed by MST (47 %), SC1 (43 %) and SC4 (32 %). These 5 SATs are associated with 264 (76 %) of the 349 large significant drifts.

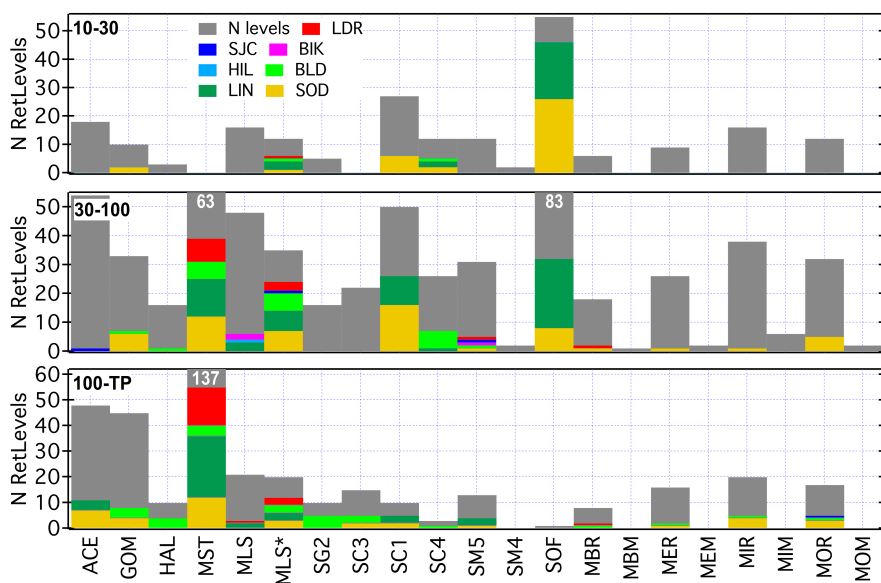


**Figure 15.** Numbers of total reporting levels (gray) and those with large ( $> 1 \text{ \% yr}^{-1}$ ) significant drifts at the paired FP sites (colors) for each SAT. The counts are divided into three distinct pressure intervals: 10–30 hPa, 30–100 hPa, and 100 hPa to the local tropopause (TP) pressure. Colored bars are stacked in front of gray bars to show the fractions of reporting levels with large significant drifts across all the FP sites relative to all reporting levels. Values for the three gray bars exceeding the y-axis limits are given in white text at the top of the bar.

The pressure dependence of the drifts of each SAT-FP was investigated by separating them into three pressure intervals: 10–30 hPa, 30–100 hPa and from 100 hPa down to the local tropopause pressure (100–TP). For the 21 SATs and 7 FP sites there were a total of 215, 604 and 394 SAT-FP time series in the 10–30, 30–100 and 100–TP pressure ranges (Fig. 15). In these pressure intervals, 76 (35 %), 209 (35 %) and 134 (34 %) of the drifts were statistically significant and 65 (30 %), 157 (26 %) and 127 (32 %) were large and significant. The uniformity of these overall percentages across the three pressure intervals suggests a general lack of pressure dependence of the significant drifts, but these bulk statistics do not provide conclusive evidence for individual SATs.

645 MLS\* drifts in the 100–TP pressure interval were large and significant for 60 % of the reporting levels across its 5 paired FP sites (Fig. 15). In this lowest layer of the stratosphere, 50 % of the SG2 and SC1 drifts and 40 % of the HAL and MST drifts were also large and significant. Interestingly, all large significant SC1 drifts in the 100–TP interval were over SOD and LIN while none were over BLD. For MST the highest percentages of large significant drifts (100–TP) were over LIN (50 %) and LDR (68 %). It is difficult to assess if the large significant drifts of a specific SAT were latitude dependent in any of the pressure intervals because most SATs paired with only 3 or fewer FP sites.

650 For reporting pressures 30–100 hPa, 39 % to 69 % of the drifts of SOF, SC1, MST, and MLS\* (in increasing order) were large and significant. All large and significant SC1 drifts were over SOD and LIN, with none over BLD, the same as for SC1 drifts in the 100–TP interval. The greatest fractions of large significant drifts for MST were again at LIN (81 %) and LDR (73 %), although there was also a high percentage at SOD (67 %). Large significant drift percentages for MLS were highest at LIN (43 %), while for MLS\* they were 100 % at SOD and LIN, 86 % at BLD and 43 % at LDR. The fractions of large  
655 significant SOF drifts were considerable at LIN (61 %), one of the only two FP sites with enough SOF-coincident soundings to permit statistically robust analyses of drift.

In the 10–30 hPa interval, only two SATs had large significant drifts at  $\geq 50$  % of their reporting levels, MLS\* (50 %) and SOF (84 %). For MLS\*, 100 % and 50 % of drifts in this pressure range were large and significant over LIN and LDR, respectively. Large significant drift percentages for SOF were again high at SOD (84 %) and LIN (83 %). Interestingly, 55 % of the drifts in  
660 SC1 retrievals at SOD were large and significant while none were at LIN or BLD.

Some SATs were associated with high percentages of large significant drifts at only one FP site. For GOM drifts at SOD, BLD and LDR, 8 of the 9 large significant drifts at 43 total reporting levels in the 10–30 hPa and 30–100 hPa intervals were at SOD. In the two highest pressure intervals, 8 of 10 large significant drifts in MOR were at SOD, with one each at BLD and SJC and none at BIK or LDR. In the 100–TP interval, 7 of 11 large significant drifts for ACE were at SOD (48 reporting  
665 levels over 5 sites) and 4 of 5 large significant drifts for MIR were at SOD (20 levels over 4 sites). In total, 134 (38 %) and 122 (35 %) of 349 significant drifts were identified over SOD and LIN. However, when interpreting these high percentages, it should be considered that 359 (29 %) and 260 (21 %) of all the SAT-FP time series analyzed for drift were over SOD and LIN, respectively.

#### 4.4 Mean drifts for the unique SAT-FP pairs

670 Statistics for the drifts at all reporting levels in the same three pressure intervals are presented for each SAT-FP pair in Fig. 16. Each horizontal bar denotes the weighted average of drifts for a specific SAT-FP pair over all reporting levels in the given pressure interval, while the vertical bars depict the 95 % confidence intervals of the weighted means. Weights were calculated using Eq. 10 that scales the standard errors of drifts by the SAT-dependent compensation factors (i.e., grid width vs vertical resolution) that were employed in the bias analyses. Uncertainties of the weighted averages were determined from the weights  
675 and the standard errors of the computed drifts using Eq. 11. The mean drift for a given SAT-FP pair is statistically significant if its 95 % confidence interval (vertical bar) does not include zero (horizontal black line at zero drift).

For some SATs there are large ( $>1$  % in magnitude) and statistically significant mean drifts in multiple pressure intervals (Fig. 16). GOM has large negative mean drifts at SOD in both the 10–30 hPa and 30–100 hPa intervals. HAL has positive and significant mean drifts over BLD in all three pressure ranges but only those for 10–30 hPa and 100–TP are  $>1$  %  $\text{yr}^{-1}$ . For  
680 MST, there are large significant mean drifts in the 30–100 hPa and 100–TP intervals over LDR, LIN and SOD. These mean drifts at LDR and LIN are positive, while those at SOD are opposite in sign. Large positive mean drifts in SC1 are indicated for all three pressure intervals at SOD and for the 30–100 hPa and 100–TP intervals at LIN. For SC4 there are large negative

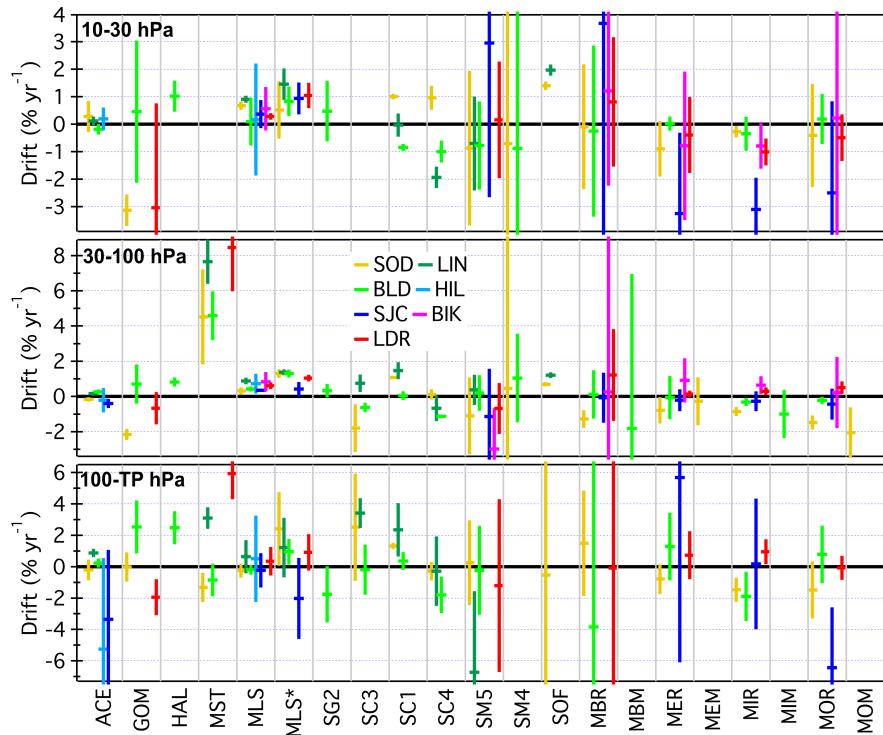


**Figure 16.** Mean drifts (horizontal bars) and their uncertainties (vertical bars) for each SAT-FP pair across all reporting levels within each of the three pressure intervals. The x-axis bins separate results for the 21 different SATs, with color-coded bars presenting statistics for the individual FP sites.

mean drifts in all three pressure intervals over BLD. Of the eight MIPAS retrievals evaluated here, none have large significant mean drifts in more than one of the three pressure intervals.

685 Another way to utilize Fig. 16 is to look for uniformity in the mean drifts of a SAT across all its paired FP sites, in one or more pressure intervals. Consistency in the drifts of a given SAT over multiple FP sites, especially those at widely separated latitudes in different hemispheres, provides evidence that the drifts are not latitude dependent. For example, the mean drifts of MLS\* over its 5 paired FP sites, ranging in latitude from 45°S to 67°N are relatively uniform in both the 30–100 and 10–30 hPa intervals (Fig. 16). Mean drifts for ACE, SC4, SM5, MBR, MER and MIR in the 10–30 hPa range are also consistent across  
 690 their paired FP sites when the uncertainties are considered. Other examples of SATs with consistent mean drifts over wide latitude ranges can be found in Fig. 16.

#### 4.5 Mean drifts at each FP site across all SATs

When viewed across each panel of Fig. 16, uniformity in the large significant mean drifts of multiple SATs at a specific FP site (marker color) may be indicative of a drift in the FP time series at that site rather than in the SAT time series. However,

695 this is conclusive only if the mean drifts for a given FP site are consistent across several different SATs, not just for multiple  
retrievals of the same satellite instrument (e.g., MIPAS). For example, in the 10–30 hPa interval, there are relatively uniform  
large negative mean drifts at SJC when paired with 3 different MIPAS retrievals (MER, MIR and MOR), but the mean drifts at  
SJC for another MIPAS retrieval (MBR) and 2 non-MIPAS instruments (MLS and SM5) are neither negative nor significant.  
Similarly, in the 30–100 hPa interval, mean drifts for SOD paired with 7 SATs are negative and statistically significant, but 5  
700 of those 7 drifts involve MIPAS retrievals and the mean drifts for 10 other SATs at SOD are either positive or not significantly  
different from zero.

This interpretation of the mean drifts shown in Fig. 16 is supported by the visible inconsistencies between the drift profiles  
of the various SATs paired with each FP site (Figs. 14 and B8–B9). For example, the drift profiles of GOM, MST, MLS and  
SM5 at LDR (Fig. 14c) are all notably different. Similar inconsistencies between different SATs are present at other FP sites  
705 for both the non-MIPAS and MIPAS SATs. Preliminary calculations of mean drift profiles across all SATs, non-MIPAS and  
MIPAS SATs included, at a specific FP site, revealed that their large uncertainties rarely produce mean drifts with statistical  
significance. This is not surprising given the uniqueness of each SAT instrument and its retrieval methods for water vapor  
measurements, so no further analyses of the multiple SAT mean drifts at each FP site were performed. Such an analysis could  
be performed on a subset of the most stable SATs, but that would be somewhat subjective and beyond the scope of this paper.

#### 710 **4.6 Mean drifts for each SAT across all FP sites**

Mean drifts for each SAT across all FP sites paired with it were calculated in the three pressure intervals defined above,  
employing the same method used to calculate the mean drifts of each unique SAT-FP pair (Fig. 16). Specifically, weighted  
means of drifts were computed using all the drifts in the appropriate ranges of reporting pressures, not by averaging the  
mean drifts at different FP sites. Averaging weights were based on the standard errors of drifts and the same SAT-dependent  
715 compensation factors employed in the site-specific mean drift computations. Uncertainties of the mean drifts of SATs across  
their paired FP sites were calculated from the averaging weights and standard errors of drifts using Eq. 11. Mean drifts for each  
SAT in the three pressure intervals are presented in Fig. 17 and listed in Tables 5 and 6.

Fig. 17 is analogous to Fig. 8 except it presents statistics for drifts instead of biases. Here, each thick horizontal bar represents  
the 95 % confidence interval of the mean drift. Since these confidence intervals are symmetric about the mean, the value at the  
720 center of each thick horizontal bar is the mean drift. Thin horizontal lines show the inter-90 % range of drifts, with markers  
denoting the 5<sup>th</sup> and 95<sup>th</sup> percentiles. In the text below, the terms “variability” and “range” are used when discussing the 95 %  
confidence intervals (e.g., variability of  $\pm x \% \text{ yr}^{-1}$ ) and inter-90 % ranges (e.g., range of  $y$  to  $z \% \text{ yr}^{-1}$ ).

#### **4.7 Synopsis of the drift assessments**

A brief statistical synopsis of the drifts in the three pressure intervals for each SAT is now presented, including relevant  
725 information about the fractions of reporting levels with large and statistically significant drifts, and where possible, statements  
about the uniformity, signs and magnitudes of drifts in specific pressure intervals. In most cases the information can be visually

**Table 5.** Drift statistics in three pressure intervals for each non-MIPAS SAT across all paired FP sites.

SAT Code	P range (hPa)	N Levels	FP site #	Drift Mean (% yr <sup>-1</sup> )	Drift Uncertainty ( $\pm$ % yr <sup>-1</sup> )	Drift 5 <sup>th</sup> percentile (% yr <sup>-1</sup> )	Drift 95 <sup>th</sup> percentile (% yr <sup>-1</sup> )
ACE	10–30	18	4,7,16,21	0.03	0.15	-0.40	0.67
	30–100	54	4,7,16,20,21	0.07	0.09	-0.77	0.56
	100–TP	48	4,7,16,20,21	0.20	0.32	-2.57	4.80
GOM	10–30	10	4,14,21	<b>-2.12</b>	1.41	-5.15	2.44
	30–100	33	4,14,21	<b>-1.14</b>	0.60	-2.93	2.34
	100–TP	45	4,14,21	0.18	0.69	-3.70	6.46
HAL	10–30	3	4	<b>1.02</b>	0.56	0.78	1.27
	30–100	16	4	<b>0.82</b>	0.26	0.17	1.49
	100–TP	10	4	<b>2.49</b>	1.05	1.16	4.61
MST	30–100	63	4,14,16,21	<b>6.14</b>	1.06	-3.65	15.41
	100–TP	137	4,14,16,21	<b>0.74</b>	0.67	-5.58	9.13
MLS	10–30	16	3,4,7,14,16,20,21	<b>0.38</b>	0.21	-0.98	0.91
	30–100	48	3,4,7,14,16,20,21	<b>0.51</b>	0.08	0.08	1.35
	100–TP	21	4,7,14,16,20,21	0.11	0.30	-0.75	2.31
MLS* <sup>a</sup>	10–30	12	4,14,16,20,21	<b>0.95</b>	0.24	0.29	1.70
	30–100	35	4,14,16,20,21	<b>1.18</b>	0.12	0.22	1.74
	100–TP	20	4,14,16,20,21	<b>1.11</b>	0.56	-0.69	6.80
SG2	10–30	5	4	0.48	1.10	-0.92	1.40
	30–100	16	4	0.33	0.38	-0.91	1.21
	100–TP	10	4	-1.76	1.79	-14.37	0.63
SC3	30–100	22	4,16,21	<b>-0.67</b>	0.32	-3.24	1.18
	100–TP	15	4,16,21	0.25	1.01	-1.11	9.00
SC1	10–30	27	4,16,21	<b>0.46</b>	0.33	-1.17	1.31
	30–100	50	4,16,21	<b>0.84</b>	0.18	-0.52	2.32
	100–TP	10	4,16,21	<b>1.07</b>	0.47	-0.62	4.30
SC4	10–30	12	4,16,21	0.19	0.74	-2.03	1.11
	30–100	26	4,16,21	-0.25	0.28	-1.42	0.76
	100–TP	3	4,16,21	-0.59	1.38	-1.64	-0.28
SM5	10–30	12	4,14,16,20,21	-0.66	0.80	-2.74	2.41
	30–100	31	3,4,14,16,20,21	-0.50	0.57	-3.96	1.36
	100–TP	13	4,14,16,21	-1.10	1.86	-12.32	3.19
SM4	10–30	2	4,21	-0.75	2.58	-0.87	-0.71
	30–100	2	4,21	1.01	4.33	0.49	1.02
SOF	10–30	55	16,21	<b>1.58</b>	0.14	0.79	2.38
	30–100	83	16,21	<b>0.86</b>	0.11	0.14	2.26
	100–TP <sup>b</sup>	1	21	-0.53			

Statistically significant drifts are presented in boldface text.

<sup>a</sup>MLS\* is a special case for which the MLS dataset is evaluated for drifts after a significant changepoint in each time series that typically occurred in  $\sim$  2010 (see Sec. 4.2.1).

<sup>b</sup> No uncertainty or percentiles for the mean drift are presented because only one time series of SOF-FP differences in the 100–TP pressure interval (at 103 hPa over SOD) was available for drift analysis.

**Table 6.** Drift statistics in three pressure intervals for each MIPAS SAT across all paired FP sites.

SAT Code	P range (hPa)	N Levels	FP site #	Drift Mean (% yr <sup>-1</sup> )	Drift Uncertainty (±% yr <sup>-1</sup> )	Drift 5 <sup>th</sup> percentile (% yr <sup>-1</sup> )	Drift 95 <sup>th</sup> percentile (% yr <sup>-1</sup> )
MBR	10–30	6	3,4,14,20,21	0.48	0.89	-0.21	3.11
	30–100	18	3,4,14,20,21	-0.16	0.67	-1.98	3.49
	100–TP	8	4,14,21	0.19	2.95	-9.91	5.42
MBM	30–100 <sup>a</sup>	1	4	-1.82			
MER	10–30	9	3,4,14,20,21	<b>-0.53</b>	0.49	-2.50	0.09
	30–100	26	3,4,14,20,21	-0.15	0.30	-1.52	1.62
	100–TP	16	4,14,20,21	0.12	0.78	-4.20	4.79
MEM	30–100	2	21	-0.27	1.36	-0.59	-0.02
MIR	10–30	16	3,4,14,20,21	<b>-0.69</b>	0.39	-3.62	-0.06
	30–100	38	3,4,14,20,21	<b>-0.25</b>	0.19	-1.17	1.09
	100–TP	20	4,14,20,21	<b>-0.75</b>	0.71	-3.23	3.67
MIM	30–100	6	4	-1.00	1.36	-2.83	0.44
MOR	10–30	12	3,4,14,20,21	-0.35	0.67	-2.79	1.10
	30–100	32	3,4,14,20,21	<b>-0.48</b>	0.33	-1.92	1.56
	100–TP	17	4,14,20,21	-0.54	0.87	-6.57	1.61
MOM	30–100	2	21	<b>-2.05</b>	1.43	-2.37	-1.77

Statistically significant drifts are presented in boldface text.

<sup>a</sup> No uncertainty or percentiles for the mean drift are presented because only one time series of MBM-FP differences in the 30–100 hPa pressure interval (at 43 hPa over BLD) was available for drift analysis.

confirmed in one of more of Figs. 15, 16 and 17. Drifts for the 12 non-MIPAS retrievals are discussed first, then drifts for the 8 different MIPAS retrievals.

### ACE

730 Drifts for ACE were large and statistically significant at 12 of the 120 (10%) reporting levels over its 5 paired FP sites, of which 11 were at pressures >100 hPa over SOD and LIN. However, in this pressure range, only the mean drift at LIN was significant (Fig. 16). In the 30–100 hPa interval, only one drift at 54 reporting levels was large and significant over SOD, LIN, BLD, HIL and SJC. Across all paired FP sites, ACE drifts spanned a wide range in the 100–TP interval, but the variability was much smaller and the mean drift was not statistically different from zero (Fig. 17). In the two pressure intervals ≤100 hPa, both  
735 the variability and ranges of drifts across all sites were small and the mean drifts were not statistically significant.

### GOM (GOMOS)

Of the 16 large and statistically significant drifts at 88 GOM reporting levels over its 3 FP sites (SOD, BLD, LDR), 12 were over SOD and 4 were over BLD. There were significant negative mean drifts in the 10–30 and 30–100 hPa intervals over SOD (Fig. 16) because drifts at all 13 reporting pressures were negative and 8 were large and significant. Of the 11 reporting levels over

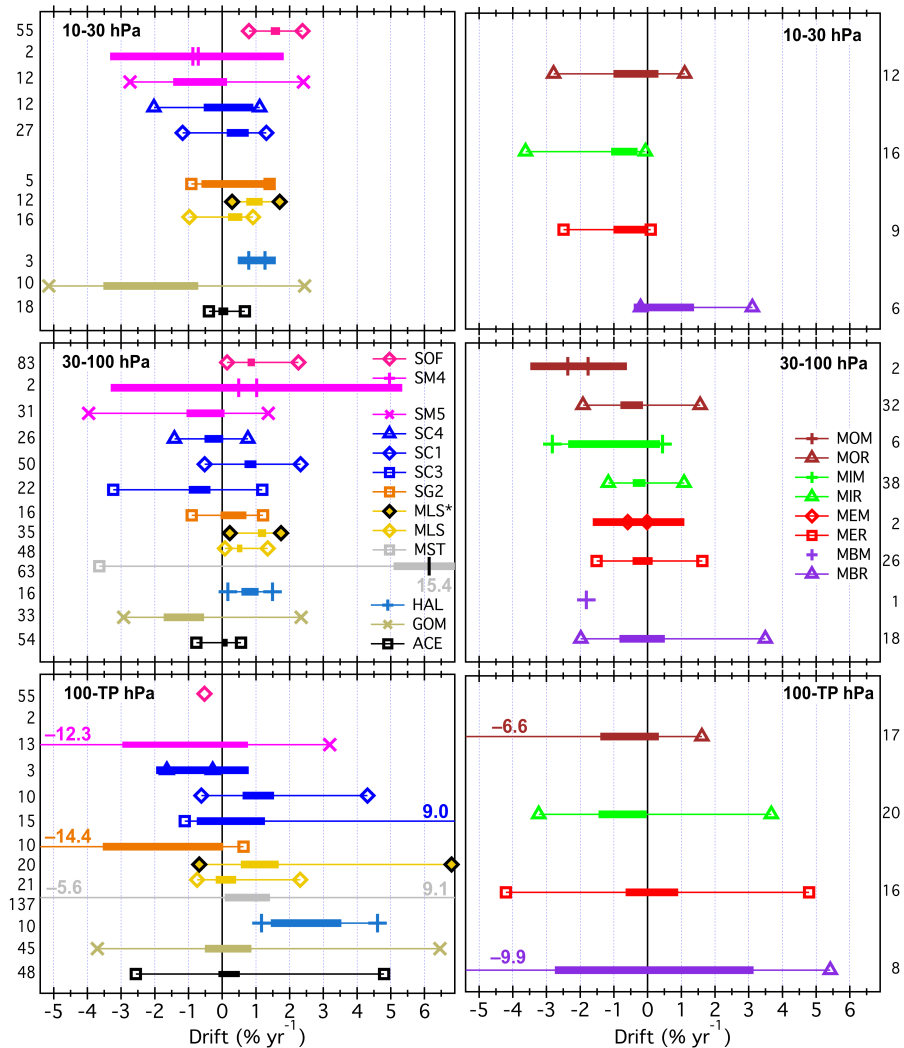


**Figure 17.** Drift statistics for each SAT across all paired FP sites, separated into the 3 pressure intervals (analogous to Fig. 8 for biases). Left and right panels are for the SATs of non-MIPAS and MIPAS instruments, respectively. Mean drifts are the values at the left-to-right centers of the 95 % confidence intervals (thick horizontal bars). Markers connected by thin horizontal lines show the 5th and 95th percentiles of the drifts for each SAT. Values of 5th and 95th percentiles that exceed the x-axis limits are enumerated as colored text. In some cases, markers for the 5th and 95th percentiles are well within the 95 % confidence intervals because of large Student-t values for data sets with small populations. In the left 30–100 hPa panel, a small black vertical bar denotes the mean drift for MST. Only a mean drift value is presented for SOF (100–TP) and MBM (30–100) because only one retrieval pressure for each provided time series of differences met the criteria for drift analysis. Values presented to the left of the left panels and to the right of right panels indicate the number of retrieval levels with difference time series that were used to determine the statistics shown.



740 BLD in the 100–TP interval, 9 were uniformly positive, of which 3 were large and significant, yielding a significant positive mean drift. Several large negative drifts in the 100–TP range over LDR resulted in a significant negative mean drift. Mean drifts across all 3 sites were negative and significant in the 30–100 and 10–30 hPa intervals, but not in the 100–TP interval (Fig. 17).

#### **HAL (HALOE)**

Measurements by HAL ceased in mid-November 2005, so its record has a >5 yr overlap with only the FP record at BLD. The  
745 HAL instrument began measurements in October 1991, but only the last 5.9 yr of its record (since Jan 2000) are analyzed here since the first WAVAS report covered HAL data through 1999 (Kley et al., 2000). Though large and significant drifts were determined for only 5 of 29 reporting levels, all 29 drifts were positive and relatively uniform. This uniformity resulted in positive and significant mean drifts of  $0.8 \pm 0.3 \text{ \% yr}^{-1}$  to  $2.5 \pm 1.0 \text{ \% yr}^{-1}$  over BLD in all three pressure intervals.

#### **MST (MAESTRO)**

750 The MST data analyzed here cover 200 reporting pressures over 4 FP sites, but only as high as 33 hPa. Large significant drifts were determined for 94 (47 %) reporting levels, with 39 and 55 in the 30–100 and 100–TP intervals, respectively. MST time series were not available at pressures  $\leq 30$  hPa for drift analysis. Drifts were large and significant at 23 of 33 (70 %) reporting levels over LDR (Fig. 10d) and 37 of 64 (58 %) reporting levels over LIN (Fig. B3h). Between these two sites, 94 % of all MST drifts were positive, producing large significant mean drifts at LIN and LDR in the 100–TP and 30–100 hPa ranges (Fig. 16).  
755 Drifts over SOD and BLD were large and significant at 40 % and 23 % of all reporting levels (Figs. B3d,l), with 17 of 18 large significant drifts being positive in the 30–100 hPa range over both sites and 12 of 16 large significant drifts being negative in the 100–TP interval. Consequently, over SOD and BLD there were significant positive mean drifts in the 30–100 hPa interval and negative mean drifts in the 100–TP interval, of which the SOD mean drift was significant. Mean MST drifts across all 4 FP sites were positive and significant in both the 30–100 and 100–TP intervals (Fig. 17).

#### **760 MLS and MLS\***

Drifts were calculated separately for the full MLS records (2004-2016) at all 7 FP sites and for shorter records from their  
change point dates ( $\sim 2010$ ) through 2016 (represented by MLS\*) at all sites except HIL and BIK. Across their paired FP sites, drifts for full MLS records and MLS\* were large and significant at 9 (11 %) of 85 reporting levels and 42 (63 %) of 67 reporting levels, respectively. In the 30–100 hPa range, the mean drifts for MLS and MLS\* across their paired FP sites were positive and  
765 significant, as were their mean drifts in the 10–30 hPa interval (Fig. 17). In the 100–TP range, mean drifts for MLS and MLS\* across their paired FP sites were weakly positive and not significant, and strongly positive and significant, respectively. Figs. 16 and 17 show not only the uniformity of the MLS and MLS\* mean drifts across their associated FP sites, but also how the MLS drifts in the 10–30 and 30–100 hPa intervals increase by 120-140 % when they are determined for the shorter post-change point records (MLS\*) instead of the full records (MLS).

#### **770 SG2 (SAGE II)**

SAGE II measurements began in September 1984 and ended in mid-2005, but only the SG2-BLD time series spanning 2000

through mid-2005 are analyzed here for drift. Large significant negative drifts were found for 5 of the 10 reporting levels in the 100–TP interval (Fig. B3m), but the mean drift was not significant. None of the drifts at pressures  $\leq 100$  hPa were significant, and neither were the mean drifts for the 30–100 hPa and 10–30 hPa intervals (Fig. 17).

#### 775 **SC3 (SCIAMACHY limb)**

Drifts were large and significant at only 5 of 37 reporting levels over SOD, LIN and BLD, and all 5 were in the 100–TP interval (Figs. B3b,f,j). However, relatively uniform positive drifts at 11 of 12 reporting levels in the 100–TP and 30–100 hPa intervals over LIN produced significant positive mean drifts (Fig. 16). SC3 time series were not available at pressures  $\leq 30$  hPa for drift analysis. Interestingly, drifts over SOD and BLD in the 30–100 hPa range were negative at 14 of 15 reporting levels, resulting  
780 in significant negative mean drifts. Across the three FP sites, there was a significant negative mean drift in the 30–100 hPa interval.

#### **SC1 (SCIAMACHY solar OEM)**

Drifts over SOD at 24 of 31 (77 %) reporting levels were uniform, positive, large and significant (Fig. 10a), as were the mean drifts over SOD for all three pressure intervals. Drifts at all 13 SC1 reporting levels  $>50$  hPa over LIN (Fig. B3e) were also  
785 uniform, positive, large and significant, as were the mean drifts in the 100–TP and 10–30 hPa intervals. Over BLD, none of the drifts at all 28 reporting levels were large and significant, yet the uniformly negative drifts at the 8 levels  $\leq 30$  hPa produced a significant negative mean drift in the 10–30 hPa range. SC1 mean drifts across the 3 sites were positive and significant for all three pressure intervals (Fig. 17).

#### **SC4 (SCIAMACHY solar OP)**

790 Drifts over BLD were uniformly negative at all 13 reporting pressures and large and significant at 10 levels (Fig. B3k), producing significant negative mean drifts for all three pressure intervals (Fig. 16). Mean drifts in the 10–30 hPa range over LIN and SOD were also significant, but of opposite sign. Mean drifts in the 100–TP range were based on only one reporting pressure at each site, and only the negative drift at 115 hPa over BLD was significant. The mean drift across all three sites was statistically different from zero only for the 30–100 hPa interval.

#### 795 **SM5 (SMR 544 GHz)**

Only 9 of the drifts at 56 reporting levels across 6 paired FP sites were large and significant, and these were dispersed across the 6 sites. At LIN, 3 large significant negative drifts in the 100–TP interval produced a large significant negative mean drift. Mean drifts at each FP site were relatively uniform in all three pressure intervals, but none of the mean drifts across the FP sites were significant.

#### 800 **SM4 (SMR 489 GHz)**

Drifts were determined at only 4 SM4 reporting pressures over 2 FP sites, SOD (23 and 35 hPa) and BLD (21 and 33 hPa). No drifts were statistically significant. With only one reporting pressure per site in each of the 10–30 and 30–100 hPa pressure

ranges, the two mean drifts for each site have large uncertainties and are therefore not significant. Similarly, mean drifts across the two FP sites were highly uncertain and not statistically significant (Fig. 17).

#### 805 **SOI (SOFIE)**

Vertical profiles of drifts at SOD and LIN were similar (Figs. B3n,o), with large significant positive drifts at 76 of the 100 combined reporting pressures between 14 and 60 hPa. Drifts in the 30–100 hPa and 10–30 hPa intervals over each site were fairly uniform and positive, producing significant positive mean drifts for SOD and LIN (Fig. 16). Over the two sites, there was only one reporting pressure in the 100–TP range, and this singular drift at 103 hPa over SOD was highly uncertain and not  
810 significant. Therefore, mean drifts across the 2 FP sites were not significant in the 100–TP interval but positive and significant in both the 30–100 and 10–30 hPa intervals.

#### **MBR and MBM (MIPAS Bologna V5R NOM and MA)**

Drifts of MBR, large and significant at only 4 of 32 reporting levels over 5 FP sites, were dispersed across 3 sites (Fig. B4). Only the mean drift at SOD in the 30–100 hPa interval was significant, the result of uniform negative drifts at all 5 reporting  
815 levels (Fig. B4a). One large, significant negative drift in the 100–TP interval over each of BLD and LDR substantially increased the variability and range of drifts over all sites (Fig. 17). For MBM, the drift was not significant at 43 hPa over BLD, the only MBM time series analyzed for drift, so the resulting mean drift was highly uncertain and not significant.

#### **MER and MEM (MIPAS ESA V7R NOM and MA)**

There were 3 large and significant drifts at 51 MER reporting levels scattered over 5 sites (Fig. B5). In general, drifts were not  
820 uniformly positive or negative in any of the pressure intervals over any site except for the 2 reporting levels  $\leq 30$  hPa above SJC, and for 4 of 5 reporting levels in the 30–100 hPa interval above SOD. Significant negative mean biases were determined for both. The variability of MER drifts across all sites was small in each pressure interval. Drift results for MEM were available for only 2 reporting pressures over SOD, 34 and 52 hPa. Neither drift was significant or resulted in a significant mean drift for the 30–100 hPa interval.

#### 825 **MIR and MIM (MIPAS IMK/IAA V5R NOM and MA)**

There were 6 large and significant drifts at the 74 MIR reporting levels over 5 FP sites, and all were negative (Fig. B4). Five were over SOD, of which 4 were in the 100–TP interval, producing a significant negative mean drift. In the same pressure range, there were fairly uniform positive drifts at all 7 reporting levels over LDR and negative drifts at 4 of 5 reporting pressures over BLD, including one large, significant negative drift, and these produced significant mean drifts at both sites (Fig. 16). In the  
830 30–100 hPa range, mean drifts over SOD, BLD, BIK and LDR were significant due to relatively consistent but rarely significant negative (SOD, BLD) and positive (BIK, LDR) drifts. Similarly, consistent negative drifts at the 2–4 MIR reporting levels in the 10–30 hPa range over each of SOD, SJC and LDR resulted in significant negative mean drifts. Across the 5 FP sites, mean drifts for MIR were negative and significant in all three pressure intervals (Fig. 17). For MIM, only six time series of differences

in the 30–100 hPa range over BLD were analyzed. None of the 6 drifts or the mean drift for 30–100 hPa were statistically  
835 significant.

### **MOR and MOM (MIPAS Oxford V5R NOM and MA)**

Drifts in MOR retrievals were large and significant at 10 of 61 levels over 5 FP sites, of which 8 were negative and over SOD  
(Fig B5). Five of the 8 significant negative drifts over SOD were in the 30–100 hPa range, producing a significant negative  
mean drift (Fig. 16). Consistent positive drifts at 5 of 6 reporting levels in the same pressure interval over LDR resulted in a  
840 positive significant mean drift. At SJC, there was a large significant negative drift at the lone reporting pressure >100 hPa, so  
the mean drift was significant and negative (Fig. 16). In the 10–30 hPa pressure interval, none of the individual or mean drifts  
over the 5 FP sites were significant, so neither was the mean drift across all 5 sites. There was a significant negative mean drift  
at SOD and across all 5 FP sites in the 30–100 hPa pressure interval due to the 5 large and significant negative drifts over SOD.  
For the 2 MOM reporting pressures in the 30–100 hPa range over SOD, neither of the negative drifts were significant, but they  
845 were large and consistent enough to produce a significant negative mean drift.

## **5 Summary and conclusions**

We have compared satellite data records of stratospheric water vapour recorded since 2000 to FP profiles from 27 stations  
spanning a wide range of latitudes (45° S to 79° N). For the comparison, we applied the same approach to all satellite data  
products. In particular, we applied a priori and averaging kernels of the satellite data to the FP profiles in order to adjust them  
850 to the retrieval characteristics of each satellite data set. If averaging kernels were not available we smoothed the FP profiles with  
ad hoc Gaussian-shaped smoothing kernels to account for the vertical resolution of the satellite instruments. Two consistent  
sets of collocation criteria were utilised based on two classes of instruments: for the dense samplers we used a time difference  
< 24 hours, a distance < 1000 km, and a latitudinal difference < 5°, while for occultation instruments we used 7x24 hours,  
2000 km, and latitudinal difference < 15°.

855 We determined the profiles of the biases and drifts and their uncertainties (in terms of the standard error of the mean, SEM,  
and of the linear regressions fits) of every instrument versus each FP station by averaging over all available collocations. By  
analysing the bias and drift profiles of one satellite instrument across all hygrometer stations we obtained insight in the general  
behaviour of the satellite instruments, including general information indicating an absence of obvious latitudinal dependencies  
of their biases and drifts. Similarly, a comparison of all satellite instruments to each specific FP station provided some insight  
860 into any peculiarities of the FP record at each station. We have concentrated on the satellite data analysis and have, as a final  
synopsis of the comparisons, averaged the biases and drifts of each individual satellite instrument over all FP stations within  
three different pressure ranges, namely 10 to 30 hPa, 30 to 100 hPa, and 100 hPa to the local tropopause pressure.

Most SAT data records have biases < 10% and drifts < 1% yr<sup>-1</sup> relative to FPs that are considered the most accurate  
and best-characterized instruments for the measurement of stratospheric water vapour. Satellite instruments with biases below  
865 10% over the complete altitude range analysed here are ACE, MLS, SG2, SG3, SC4, MBR, MER, MIH, MIR, MOH, and

MOR. SATs with mean drifts  $< 1 \text{ \% yr}^{-1}$  in all three pressure intervals were ACE, MLS, SC4, MBR, MER, MIR and MOR. Of the 1213 time series of relative differences between 21 SATs and 7 FP sites that were analysed for drifts, 419 (35 %) had statistically significant drifts at the 95 % level of confidence. Of these 419 significant drifts, 349 (83 %) were also large drifts, with magnitudes  $> 1 \text{ \% yr}^{-1}$ . Five SATs were together associated with 76 % of the large significant drifts: MLS\*, SOF, MST, 870 SC1, and SC4. Eleven SATs had large significant drifts at 15 % or less of their reporting levels: ACE, MLS, SC3, SM4, MBR, MBM, MER, MEM, MIR, MIM, and MOM. GOM, HAL, MST and MOM had mean drifts with magnitudes  $> 2 \text{ \% yr}^{-1}$  in one pressure interval that makes their measurement time series unsuitable for the detection of stratospheric water vapor trends as large as  $20 \text{ \% decade}^{-1}$ .

In the 10 to 30 hPa range, most satellite data have a relative bias within the  $\pm 10 \text{ \%}$  range versus the mean of all FP data. 875 Exceptions are GOM, ILA, HIR (however, the latter two are close to  $-10 \text{ \%}$ ), MST (which does nominally not measure in this altitude range), SLA, SLB, and SM5 (nominally restricted to the UTLS). Among the well-performing instruments, ACE, MBR, MBM, MER, MIM, MOR, MOM, MLS, SG2, SC1, SC4, and SOFIE have biases within the  $\pm 3 \text{ \%}$  range. Also in the 10–30 hPa interval there were 8 SATs with statistically significant mean drifts across all of their associated FP sites, but of these, only GOM, HAL and SOF had large significant mean drifts ( $> 1 \text{ \% yr}^{-1}$ ). Of the SATs that reported data in this pressure 880 range, ACE, HAL, MLS, SG2, SM5, SM4, MBR, MER, MIR and MOR had no large significant drifts at any of their reporting levels.

The 30 to 100 hPa range is where most instruments perform best. Only GOM, MST, MEH, MEM, MOM, POM, SLA, and SM5 show biases larger than 10% (while GOM and POM are close to  $\pm 10 \text{ \%}$ , and MST does nominally not cover this altitude range). The least biased water vapour data records in this altitude range are ACE, HIR, MLS, SG3, SC4, SOF, MBH, MBR, 885 MER, MIH, and MIR, again with biases within the  $\pm 3 \text{ \%}$  range. SG2 and MOR just miss the  $\pm 3 \text{ \%}$  mark. All 21 SATs provided data for drift analysis at one or more pressure levels in the 30–100 hPa interval over at least one FP site. Most SATs had their smallest mean drifts in this pressure range relative to those above and below. Mean drifts were significant for 11 SATs in this pressure range, but only those for GOM, MST, MLS\* and MOM were large and significant.

The situation is worse in the 100 hPa to tropopause range. Here, most instruments have larger biases and drifts. Nevertheless, 890 the following SATs have biases within the  $\pm 10 \text{ \%}$  range even in this altitude range: MLS, ACE, SC4, SG2, SG3, GOM, POM, MOR, MOH, MBR, MBH, MER, MIR, and MIH. The biases are significant for almost all data sets in the three altitude ranges in the sense that the range  $\pm 2\sigma_b$ , i.e. twice their SEM (thick horizontal bars in Fig. 8), around the bias does not include zero. The large numbers of collocations that were available in most cases result in this high proportion of bias significance. The 5%- and 95%-percentiles, however, are very wide in most cases, which indicates a large spread in the individual bias profiles. Mean 895 drifts in the 100–TP pressure interval were almost always associated with larger uncertainties than those for the two pressure ranges above. Consequently, only 34 % of the mean drifts in this interval were significant, but 95 % had magnitudes  $> 1 \text{ \% yr}^{-1}$ . Overall, only 5 SATs had significant mean drifts and 3 of these (HAL, MLS\*, SC1) were large and significant.

In summary, these assessments of mean biases and drifts against FP profiles from a widespread, worldwide array of FP sites demonstrate that the satellite data records are generally very valuable sources of information on atmospheric water vapour 900 abundance from the tropopause to about 30 km altitude (10 hPa pressure). Even with their inherent biases and drifts, these

satellite records have the advantages of near-global coverage and higher spatial and temporal data densities relative to the current sparse network of FP sites. Though independently valuable within their data density limitations, the network of FP sites provides “reference points” to which the satellited data sets can be anchored. In this sense, the optimal observation system for stratospheric water vapor is based on simultaneous measurements by both types of instruments, with any detected discrepancies  
905 between them being critical information.

Finally, continuing efforts to improve stratospheric water vapor measurements include the refinement of satellite retrieval algorithms, even for instruments that are no longer operational. Indeed, new data sets have been produced since 2017 for some of these satellite instruments. Obviously, the information provided by this type of assessment is invaluable to satellite instrument teams, but will almost always lag behind the most current data sets. Therefore, we recommend routinely performing  
910 these assessments at least every 10 years.

*Data availability.* The satellite data records used in this study are publicly available from <https://publikationen.bibliothek.kit.edu/1000093970> and have the doi: 10.5445/IR/1000093970.

## Appendix A: Bias related plots

### A1 Biases per SAT dataset

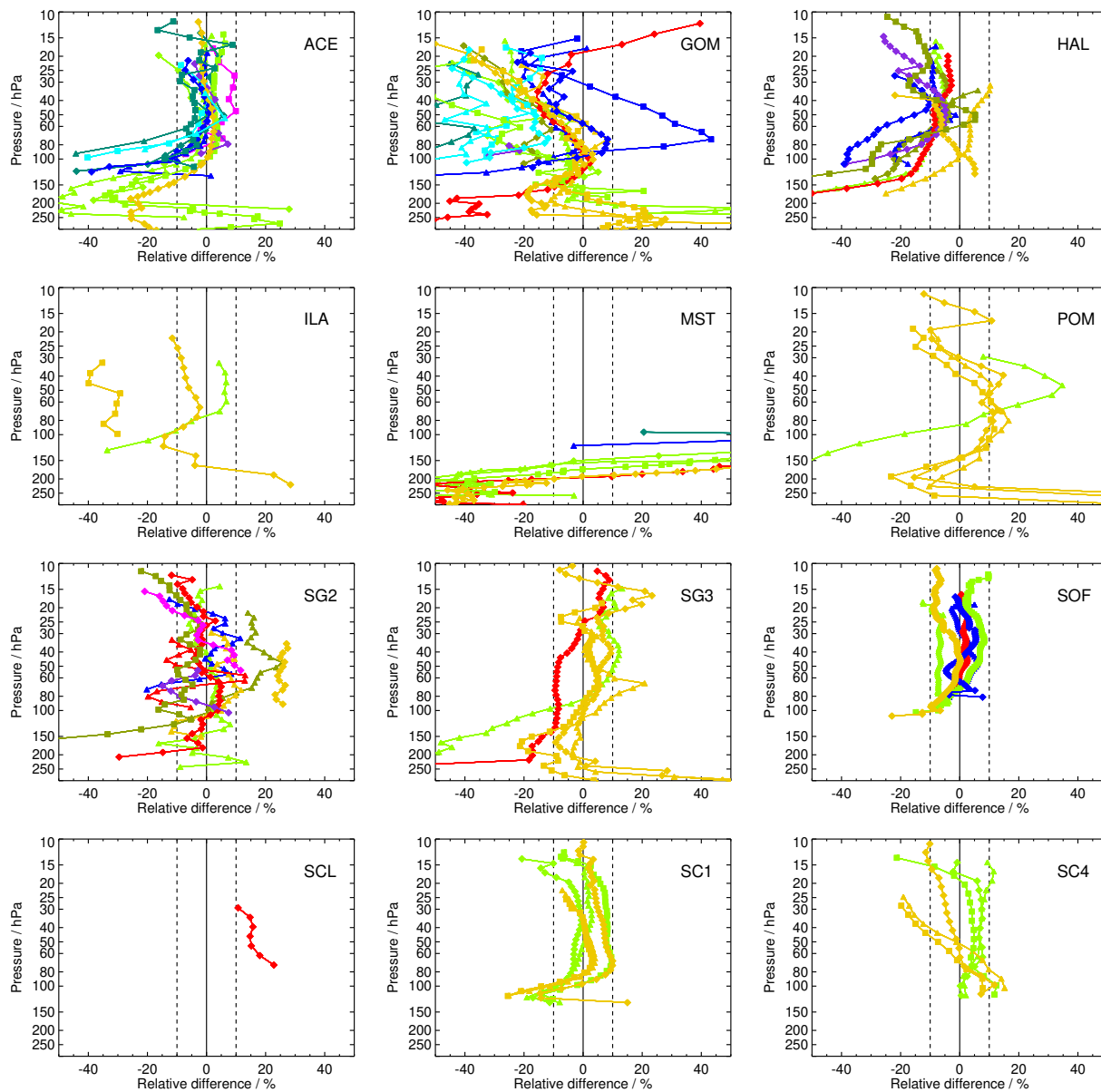


**Figure A1.** Mean relative differences between coincident SAT (no MIPAS) and FP records. Color coding of FP data according to Fig. 1.

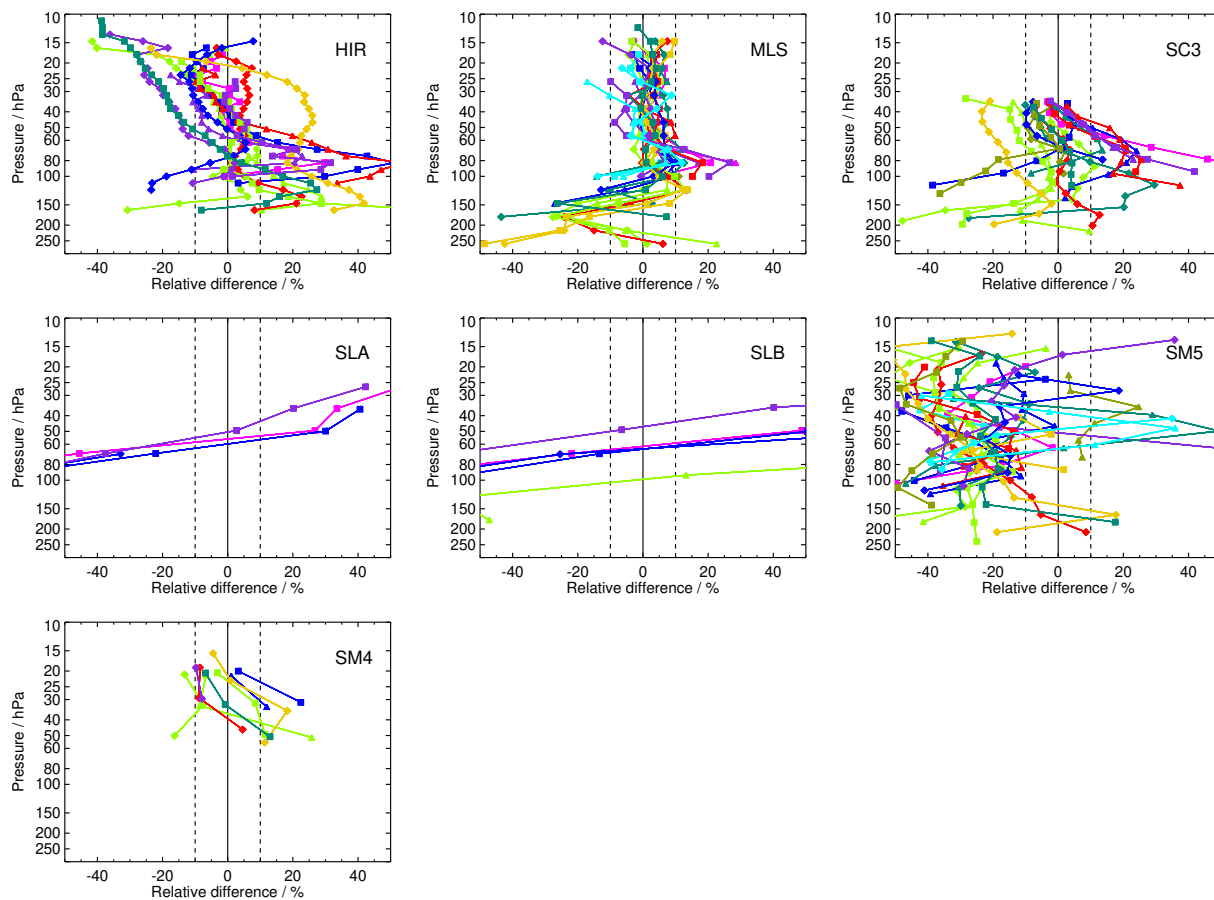


**Figure A2.** Same as Fig. A1 but for dense samplers (no MIPAS).



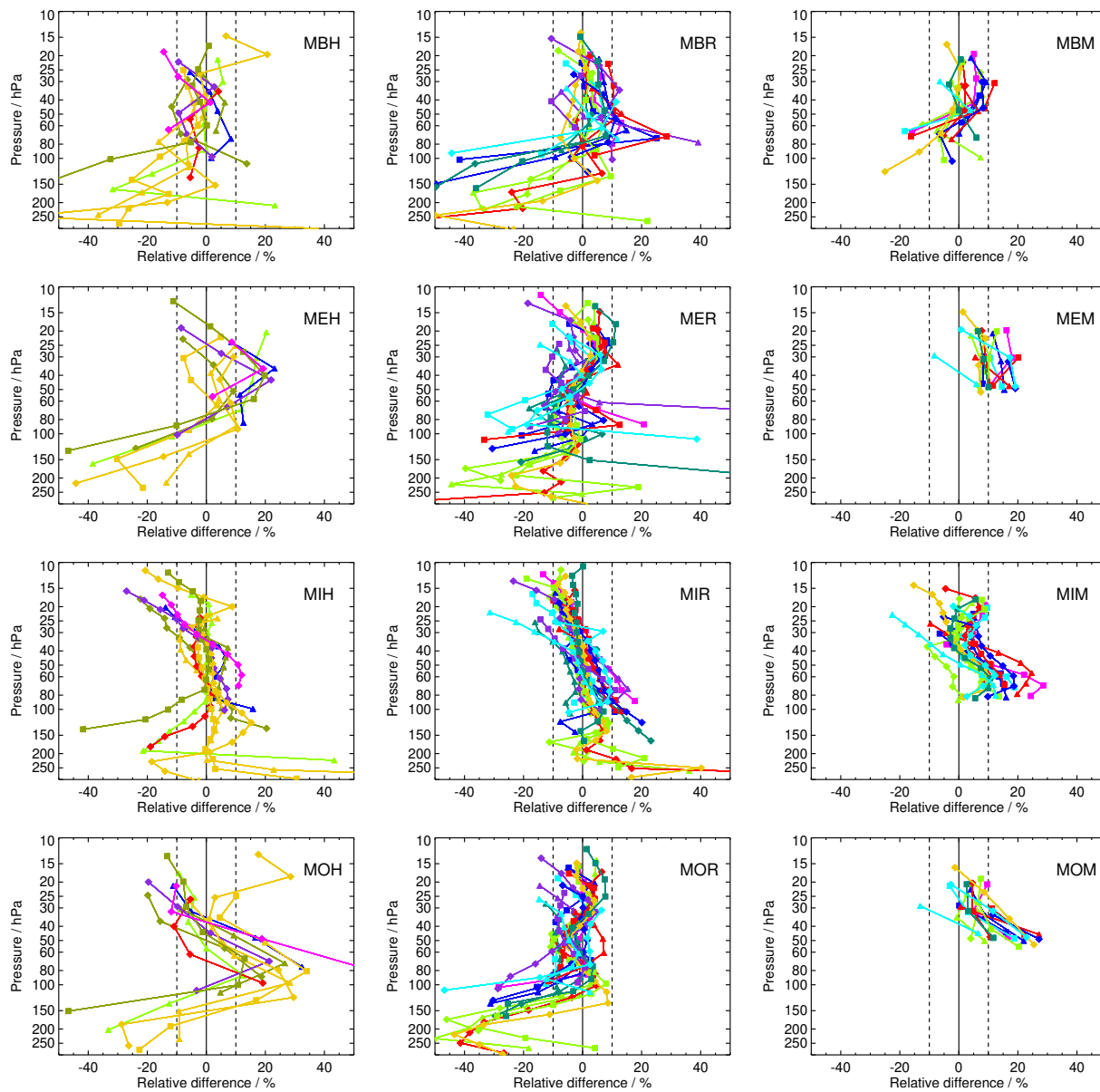


**Figure A3.** Same as Fig. A1 but MIPAS records only.

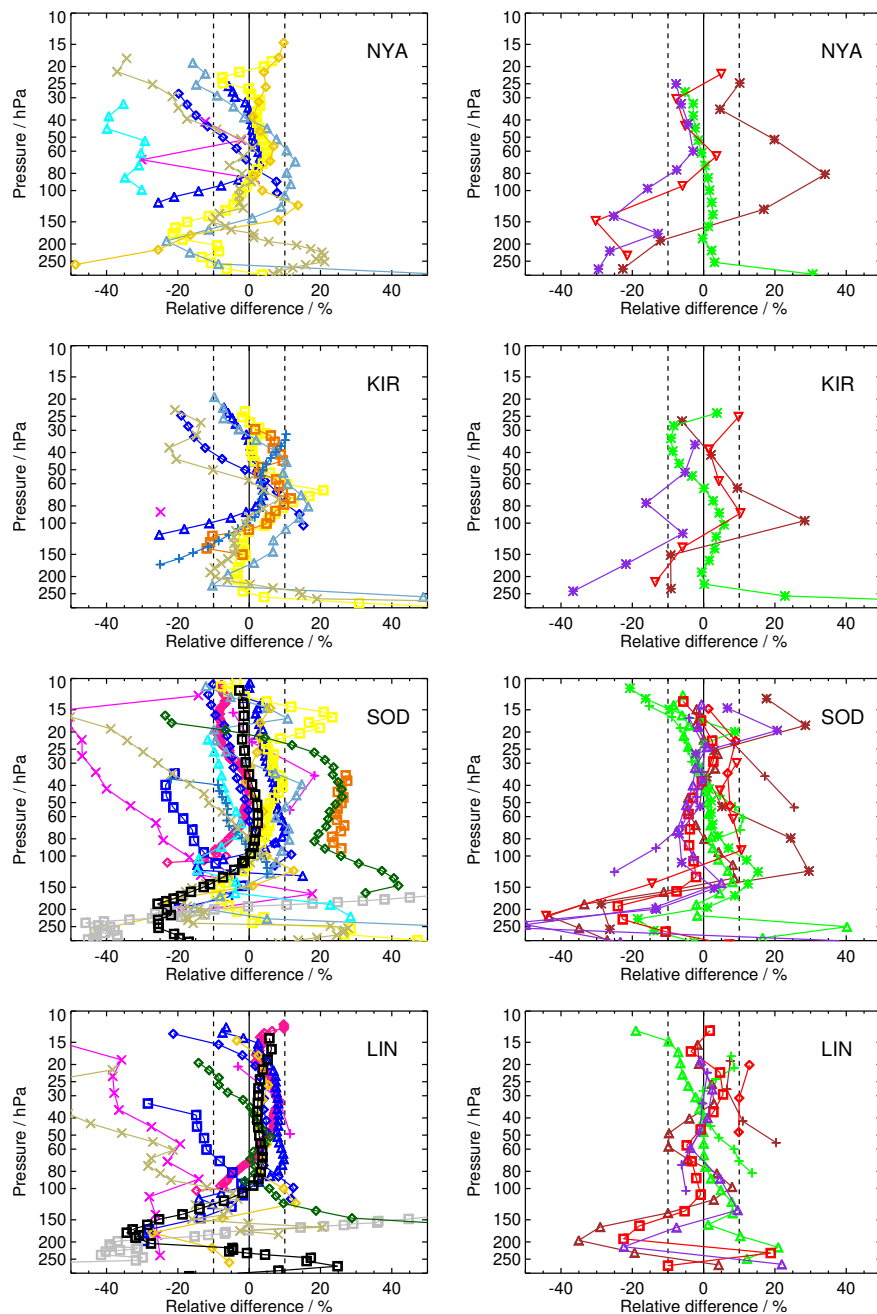


**Figure A4.** Mean relative differences between the FP stations NYA, KIR, SOD, LIN and coincident SAT records (left: data records except MIPAS; right: only MIPAS data records). Color coding of the SAT data according to Fig. 2.

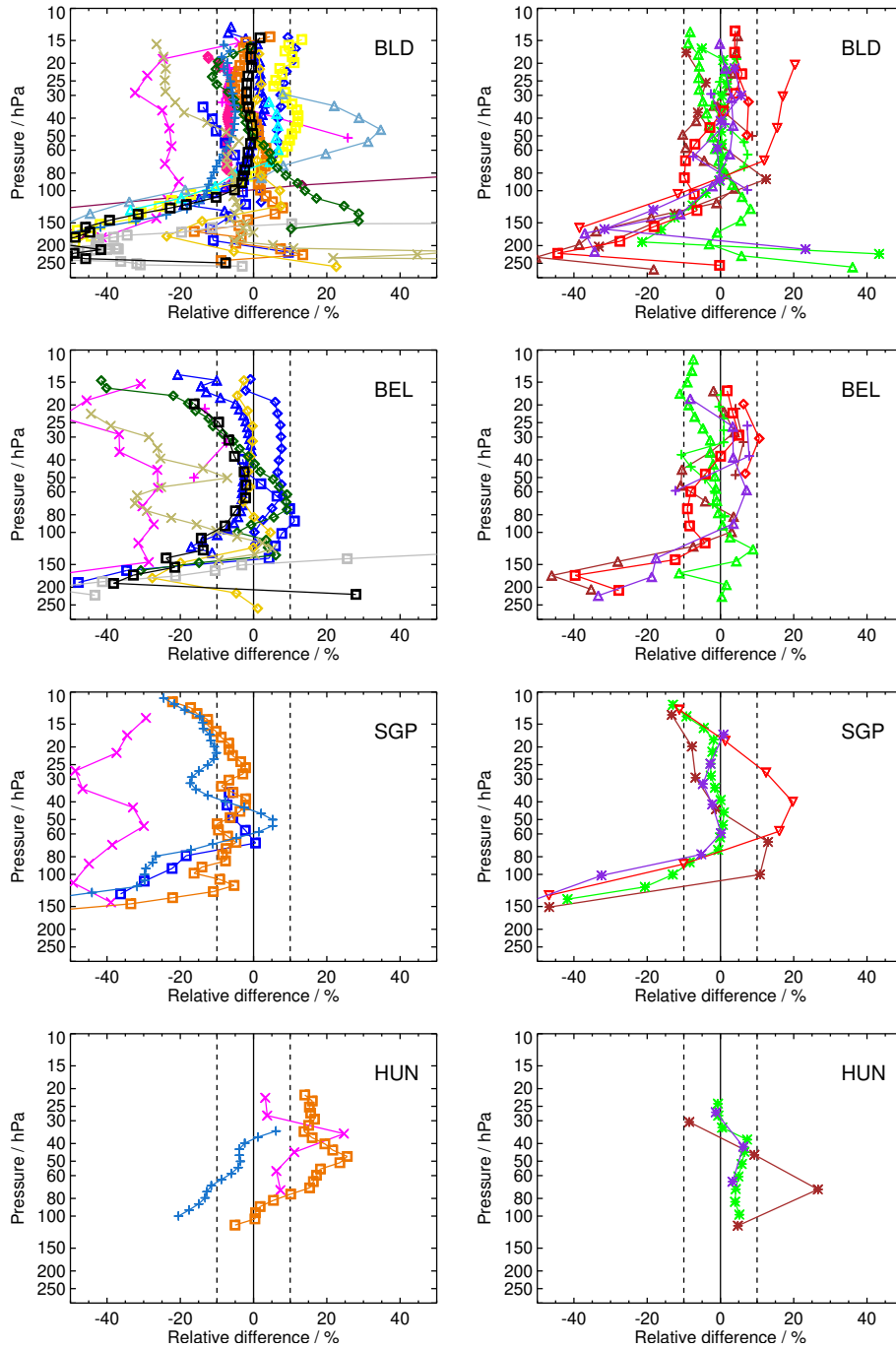


**Figure A5.** Same as Fig. A4 but for BLD, BEL, SGP, and HUN (left: non-MIPAS, right: MIPAS only).

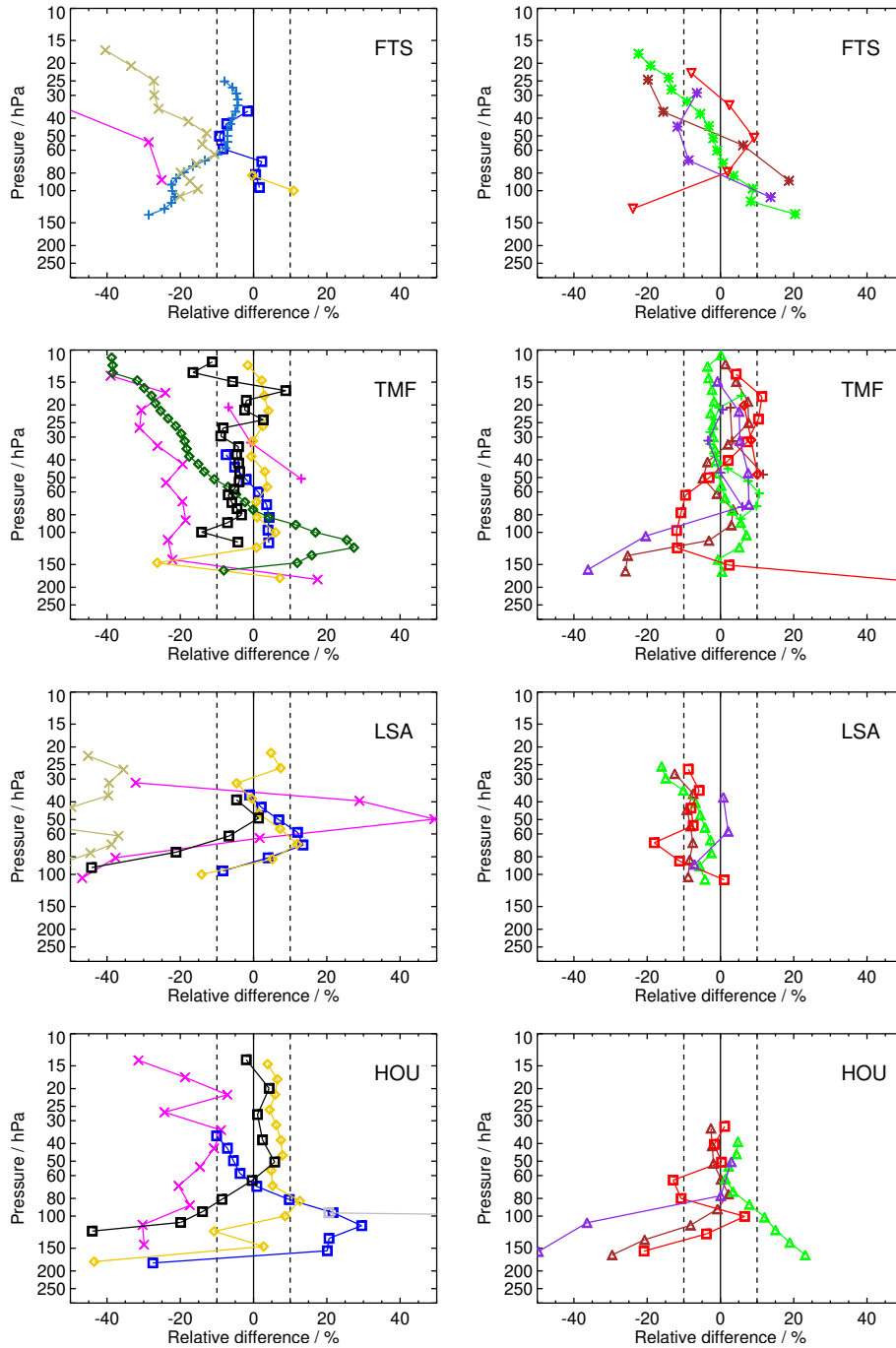


**Figure A6.** Same as Fig. A4 but for FTS, TMF, LSA, and HOU (left: non-MIPAS, right: MIPAS only).

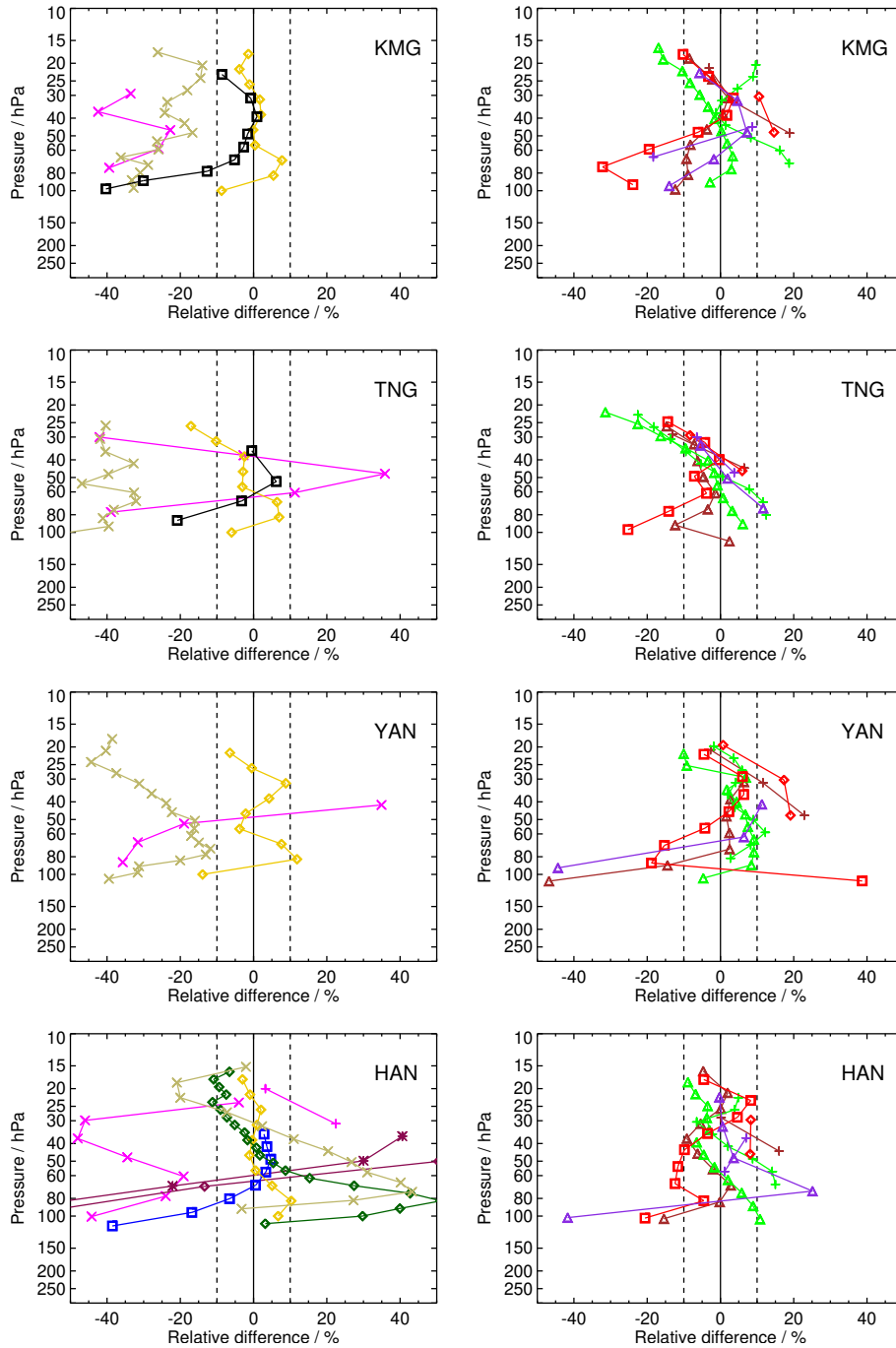


**Figure A7.** Same as Fig. A4 but for KMG, TNG, YAN, and HAN (left: non-MIPAS, right: MIPAS only).

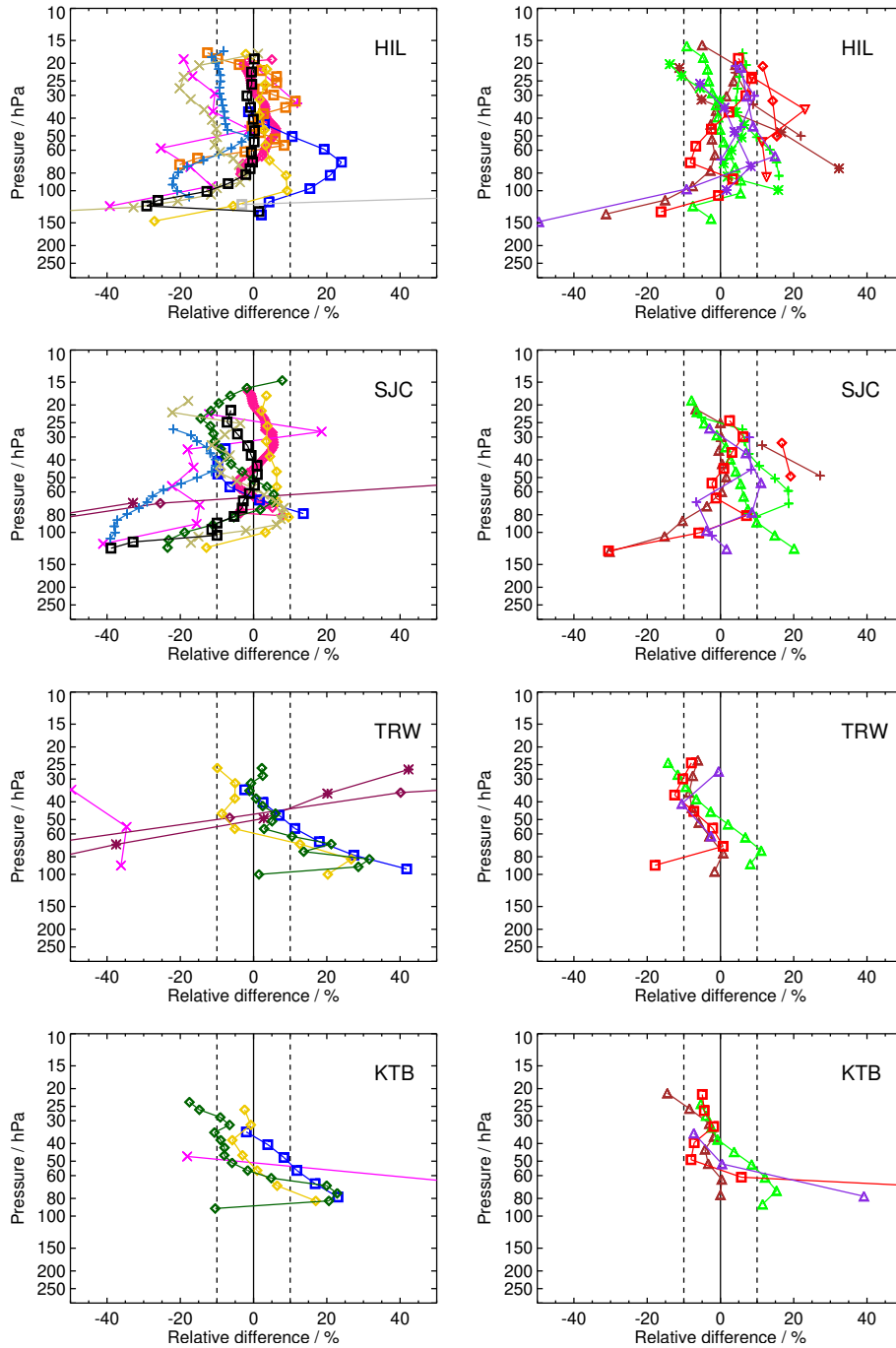


**Figure A8.** Same as Fig. A4 but for HIL, SJC, TRW, and KTB (left: non-MIPAS, right: MIPAS only).

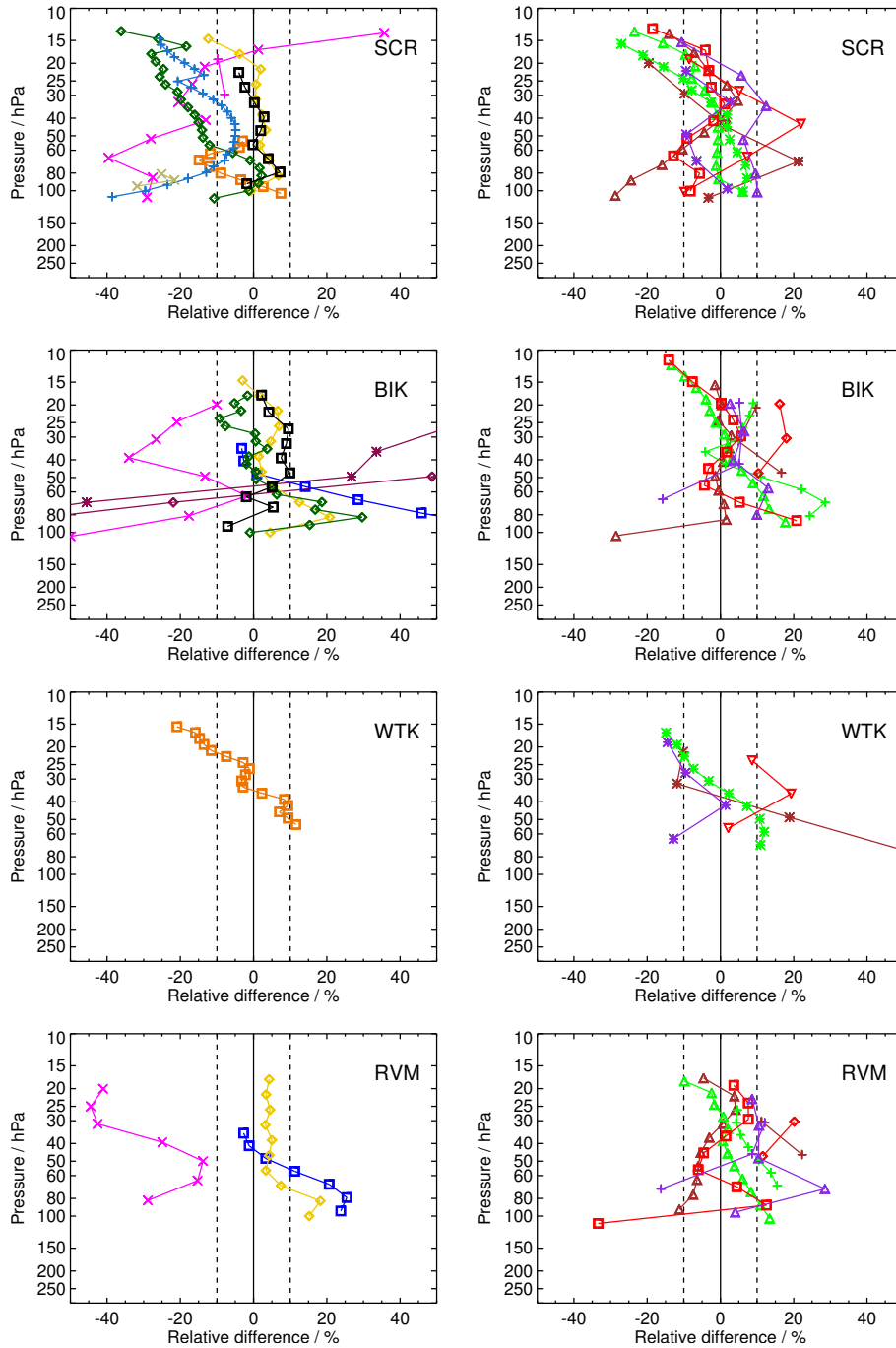


**Figure A9.** Same as Fig. A4 but for SCR, BIK, WTK, and RVM (left: non-MIPAS, right: MIPAS only).

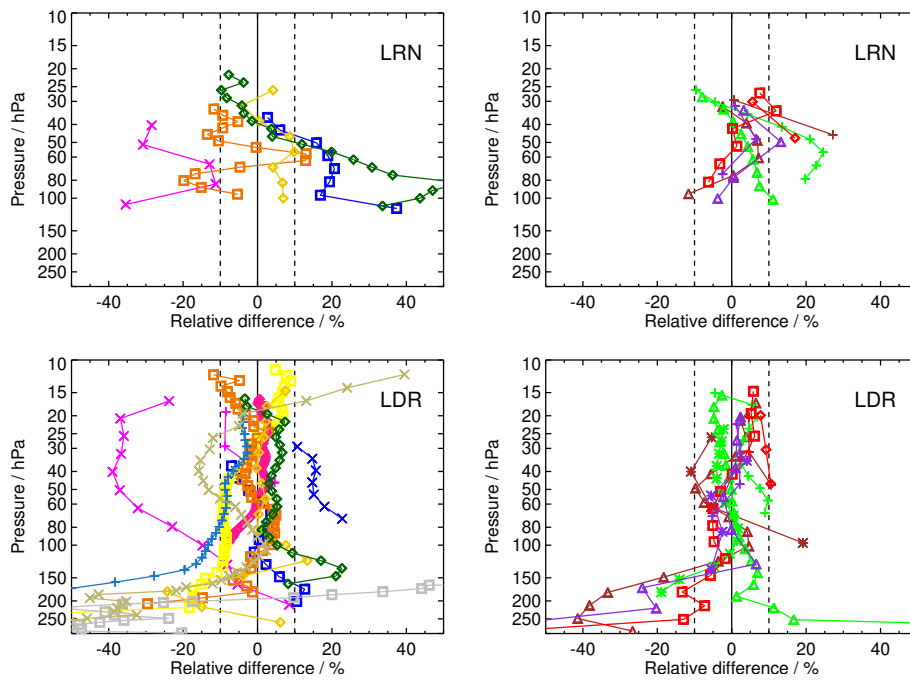


**Figure A10.** Same as Fig. A4 but for LRN and LDR (left: non-MIPAS, right: MIPAS only).



## Appendix B: Drift related plots

### B1 Drift profiles for every SAT-FP pair

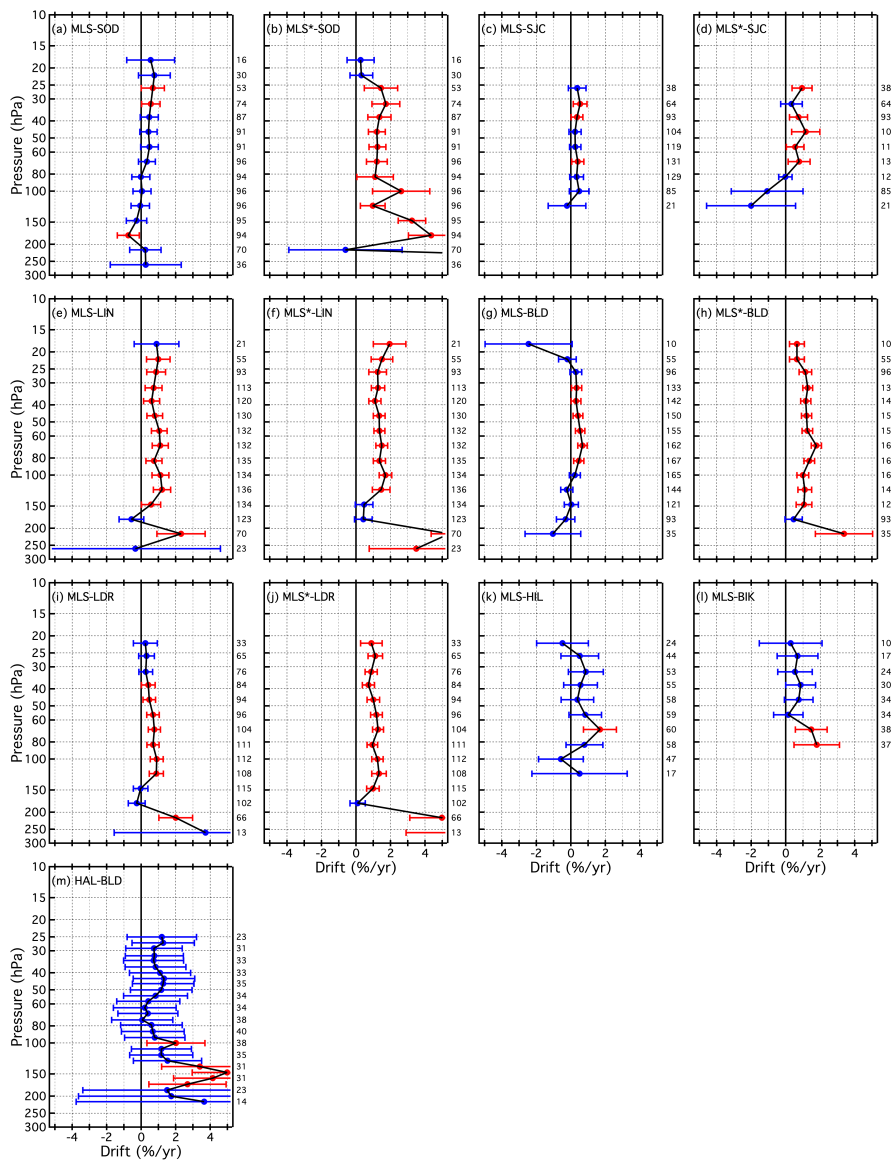


**Figure B1.** Vertical profiles of drifts (filled circles) and their 95 % confidence intervals (horizontal error bars) for 13 different SAT-FP pairs that include MLS, MLS\*, and HAL. Blue error bars denote drifts that are not significantly different from zero, while red error bars indicate statistically significant drifts. Numbers in black text to the right of each panel present the number of SAT-FP differences in the time series analyzed for drift at the corresponding pressure levels.

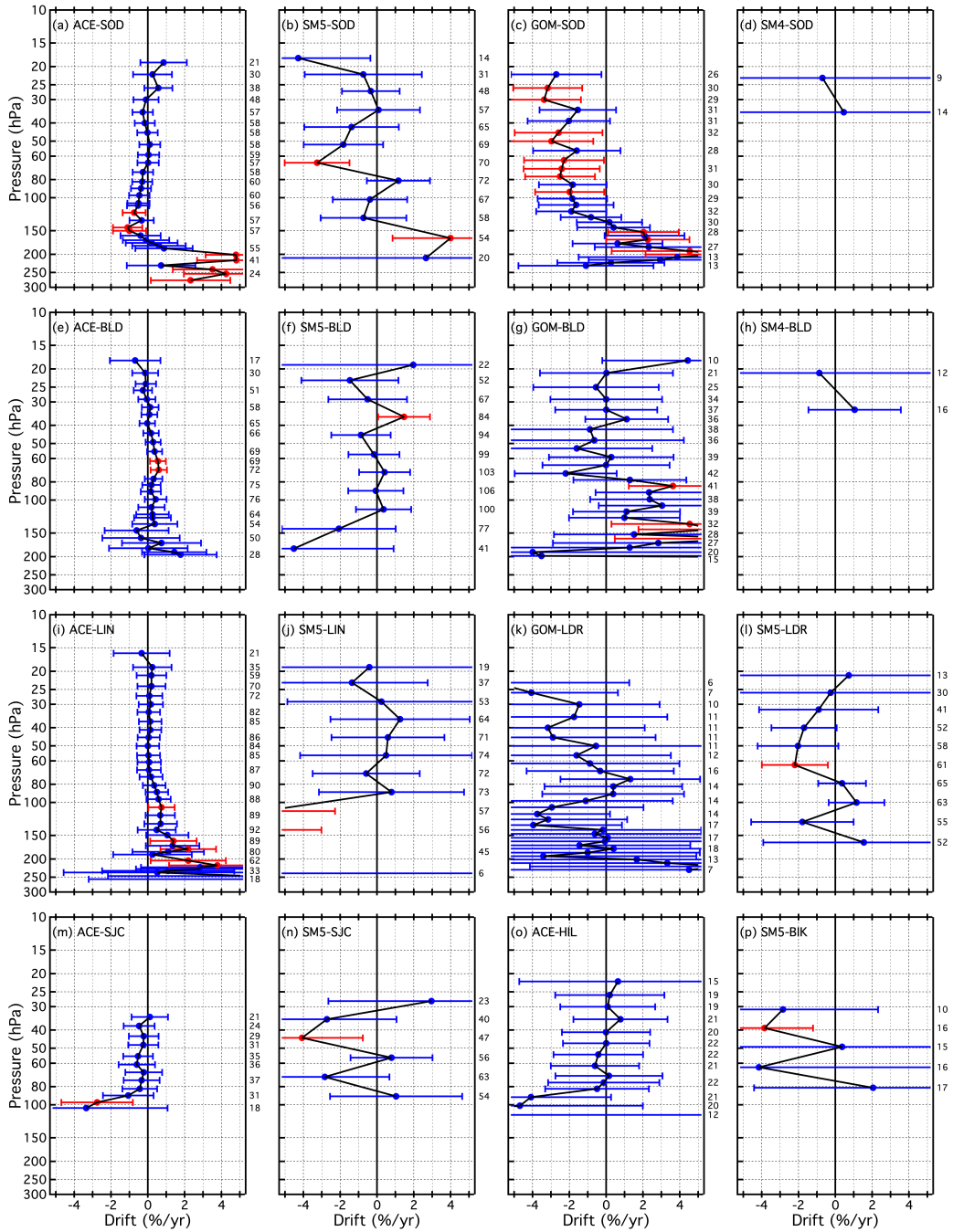


**Figure B2.** Same as Figure B1 for 16 additional SAT-FP pairings that include ACE, SM5, GOM, and SM4.

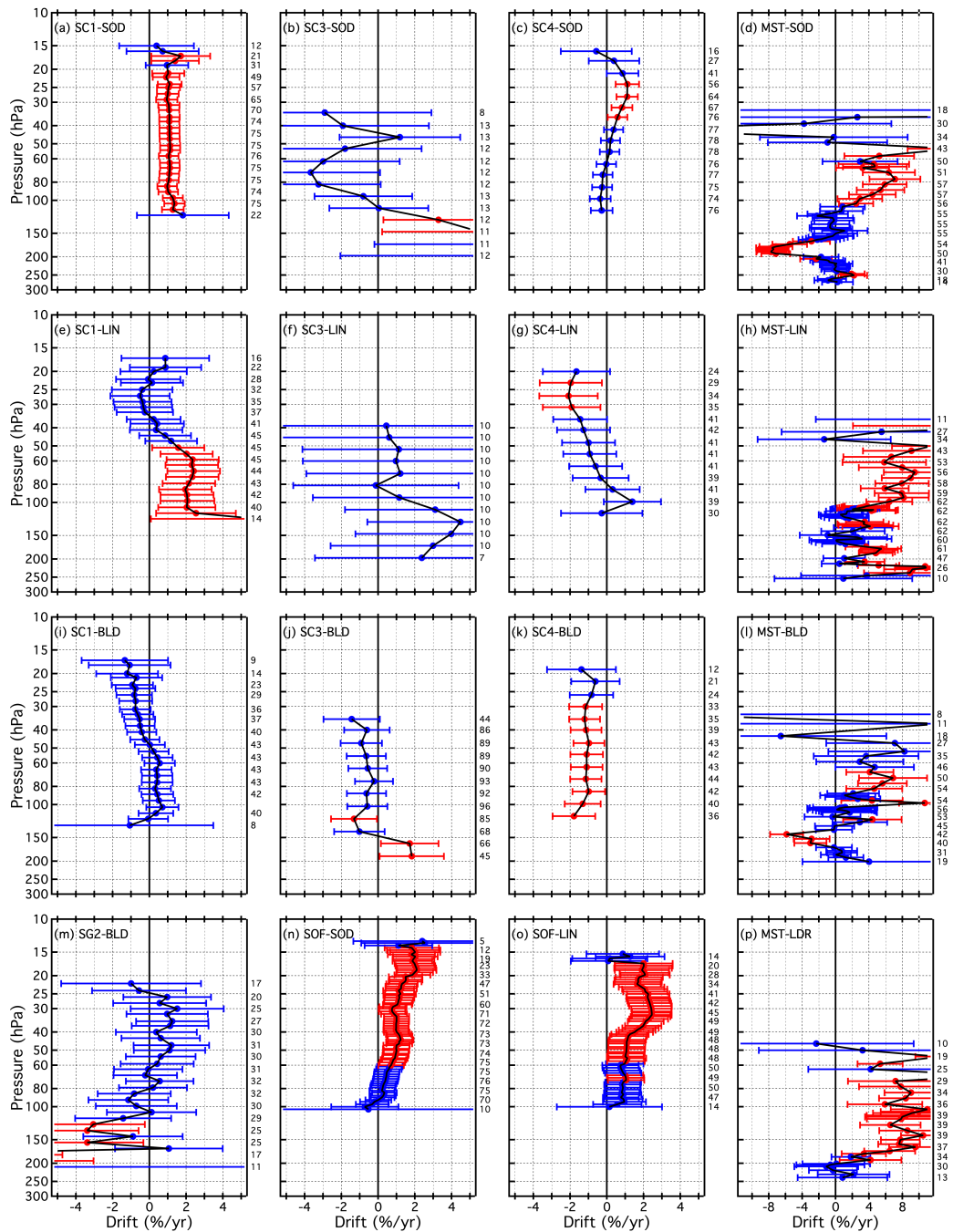


**Figure B3.** Same as Figure B1 for 16 additional SAT-FP pairings that include SC1, SC3, SC4, SG2, SOF, and MST. Note that the x-axis scale for the far right panels is expanded to better show the drifts.

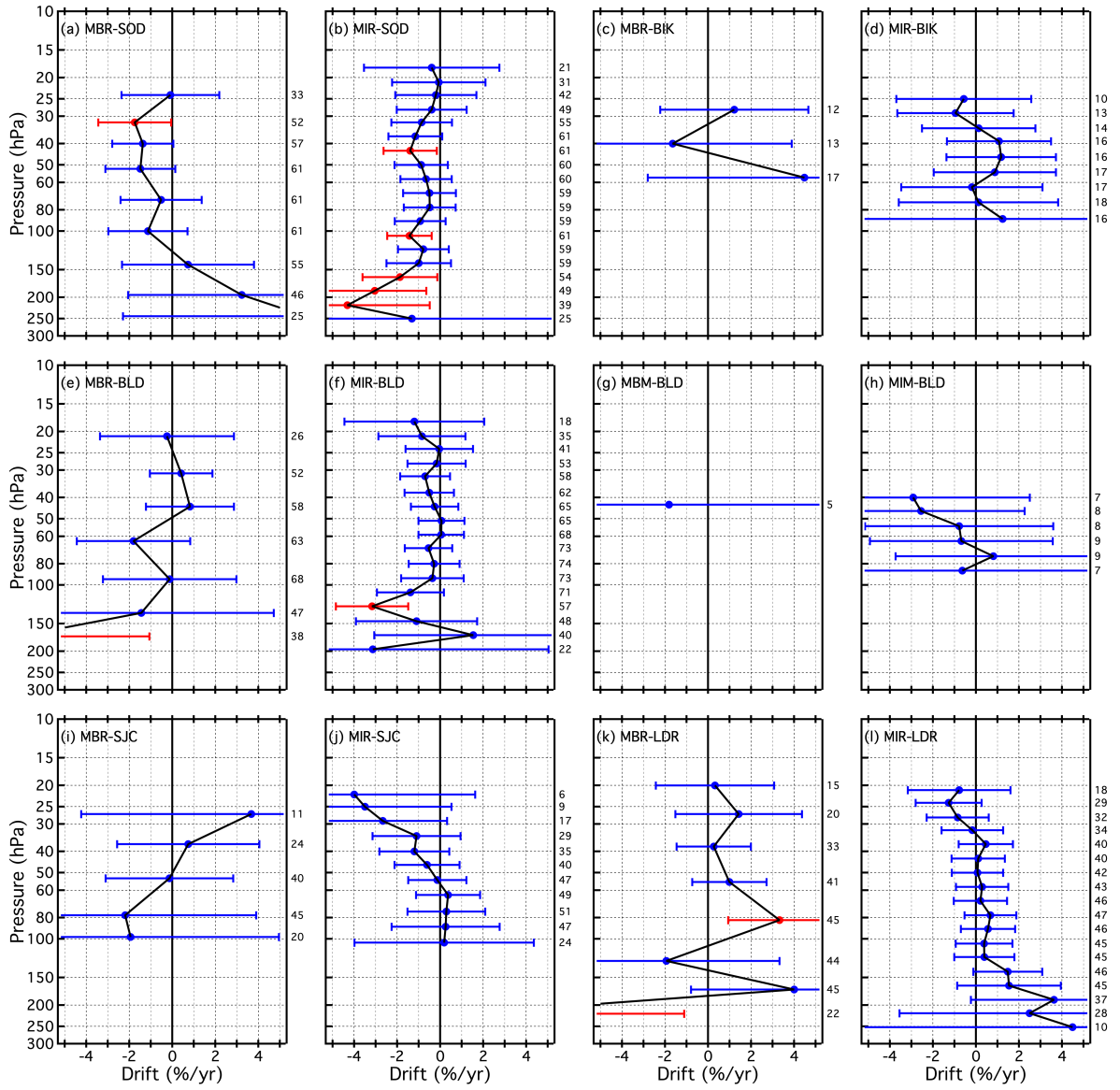


**Figure B4.** Same as Figure B1 for 12 additional SAT-FP pairings that include MBR, MIR, MBM, and MIM.

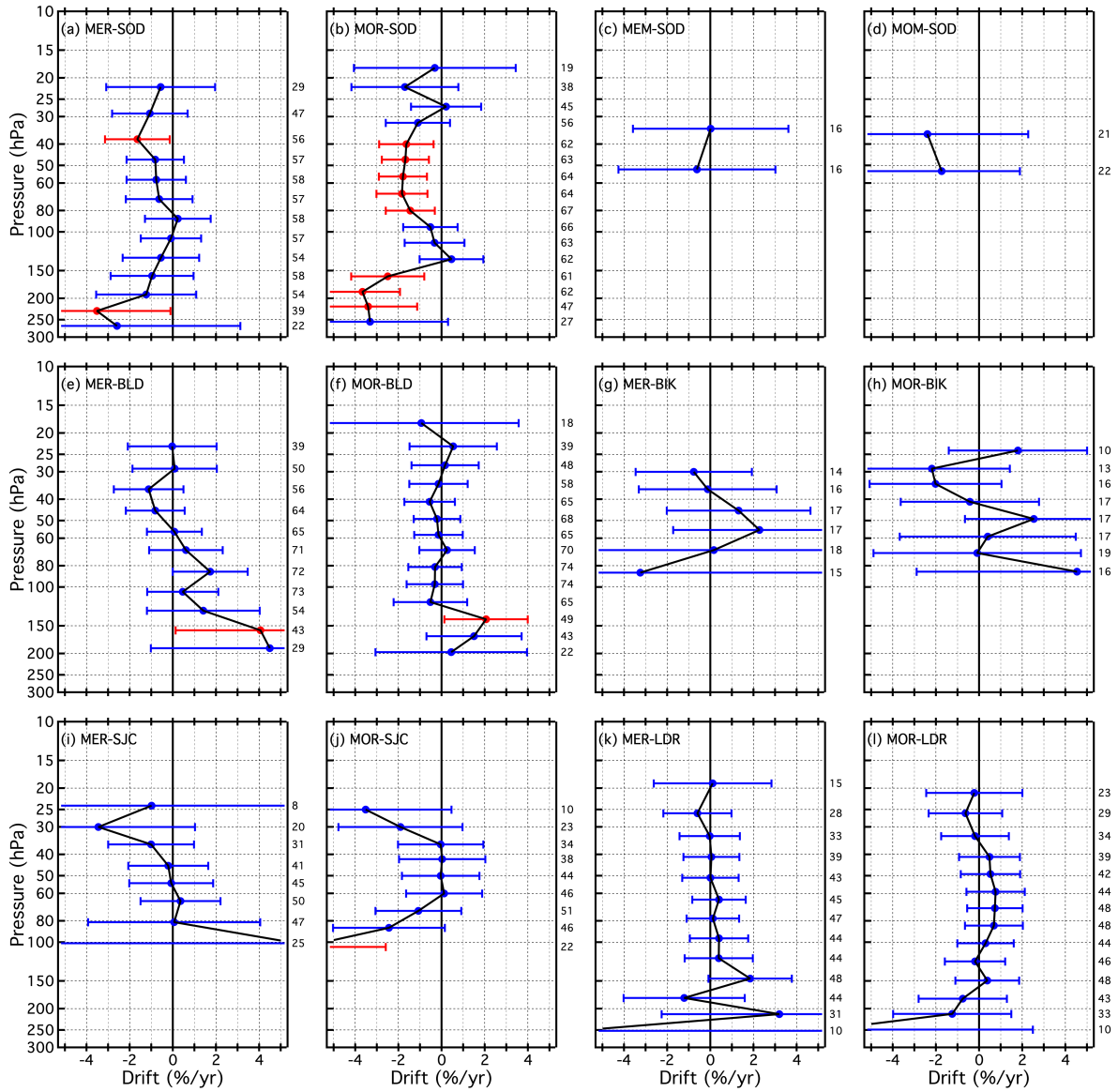


**Figure B5.** Same as Figure B1 for 12 additional SAT-FP pairings that include MER, MOR, MEM, and MOM.

## B2 Drifts per SAT dataset

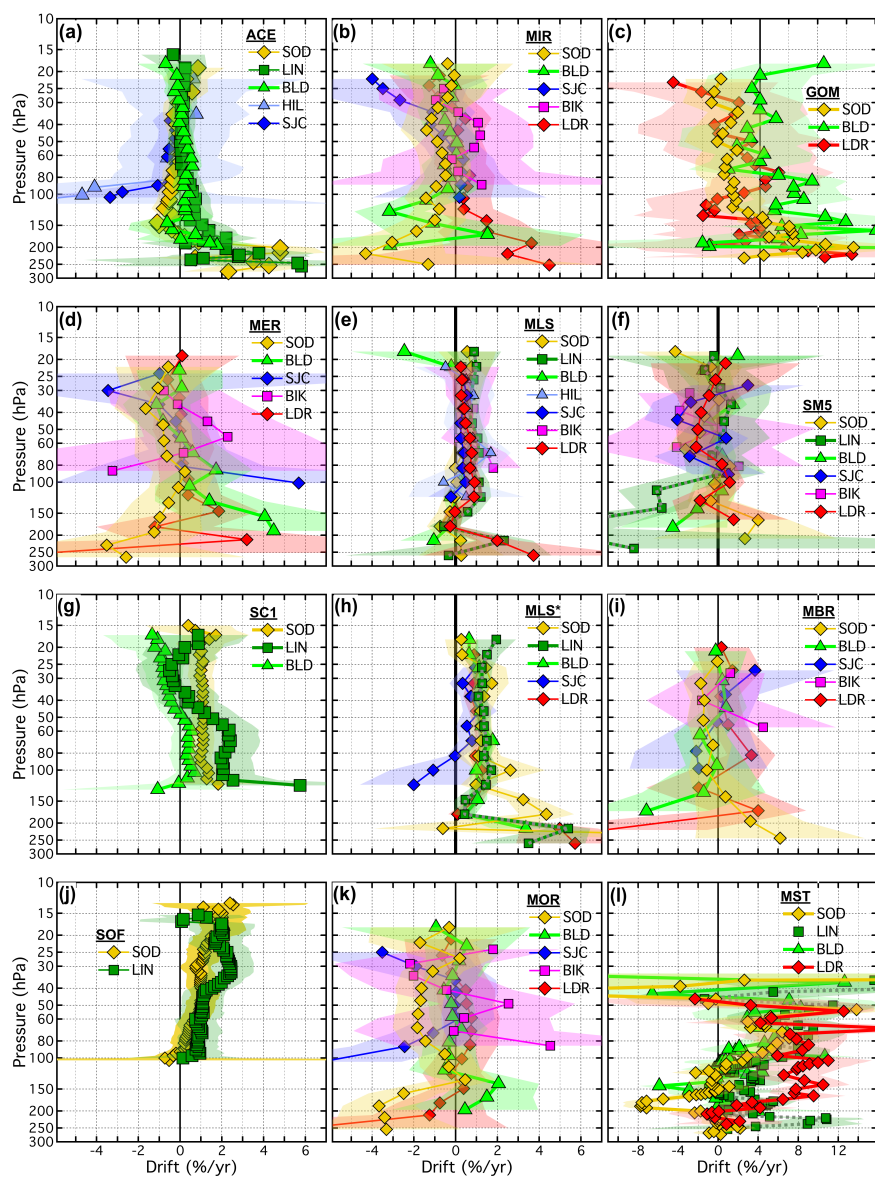


**Figure B6.** Vertical profiles of drifts in SAT-FP differences. Each panel displays the drifts for one SAT (ACE, MIR, GOM, MER, MLS, SM5, SC1, MLS\*, MBR, SOF, MOR, and MST) paired with 1-7 different FP sites. Drifts over each FP site (connected colored markers) are presented with their 95 % confidential intervals (colored-matched shading). Shading that does not cross the black vertical line at 0 % drift indicates drifts that are statistically significant. Note that the x-axis scale for the panels in the far right column is expanded to show the drifts with greater clarity.

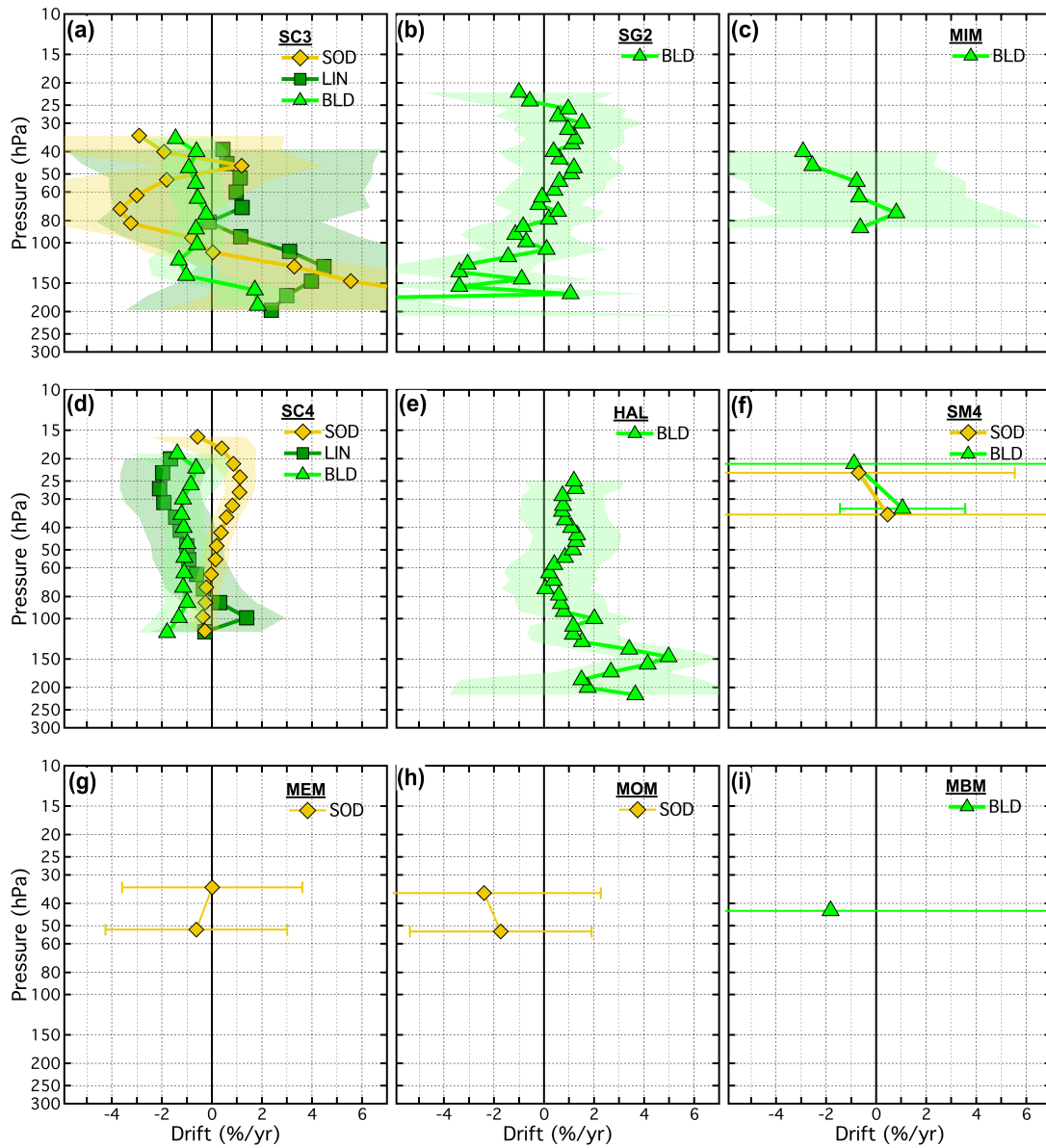


**Figure B7.** Same as Figure B6, but for SC3, SG2, MIM, SC4, HAL, SM4, MEM, MOM, and MBM.

### B3 Drifts per FP dataset, ordered by latitude

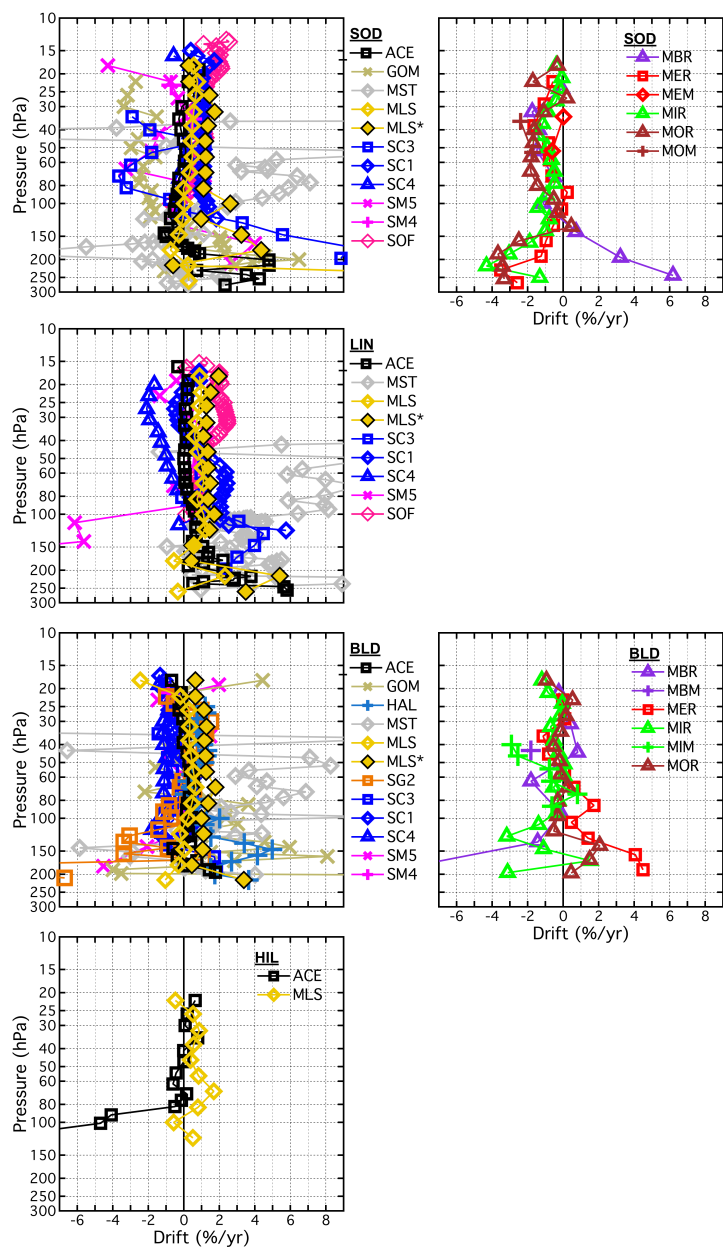


**Figure B8.** Vertical profiles of drifts in SAT-FP differences. Each panel displays the drifts for the multiple SATs paired with each FP site (SOD, LIN, BLD, and HIL). Profiles for non-MIPAS SATs appear in the left column and for MIPAS SATs appear in the right column. For LIN and HIL there were no pairings with MIPAS SATs.



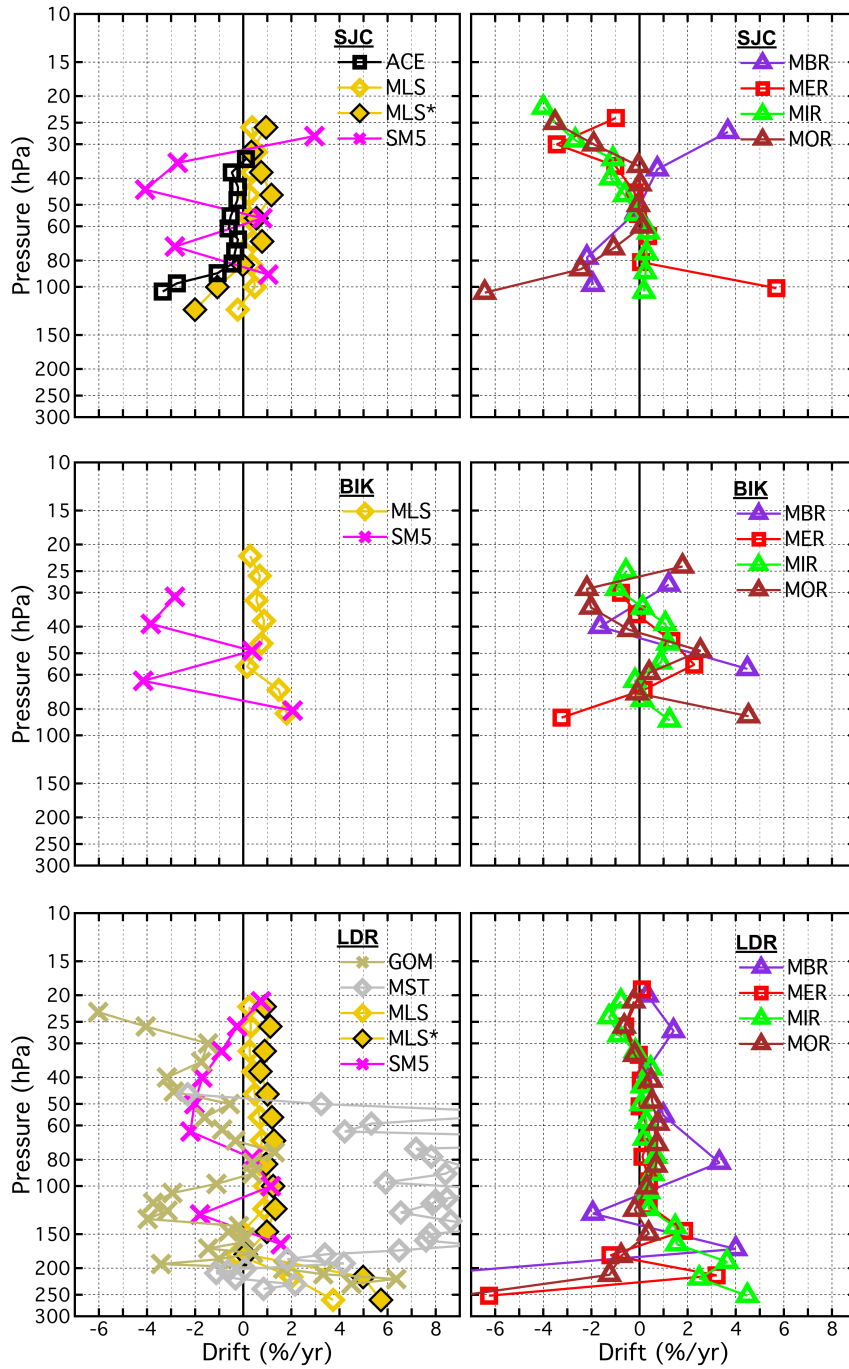


**Figure B9.** Same as Figure B8, but for SJC, BIK, and LDR.

920 *Competing interests.* Several of the (co-)authors are members of the editorial board of Atmospheric Measurement Techniques.

*Acknowledgements.* Dale Hurst thanks the NASA Upper Atmosphere Composition Observations program for continued financial support. Stefan Lossow was funded by the Stratospheric Change and its Role for Climate Prediction (SHARP) under contract STI 210/9-2. The Atmospheric Chemistry Experiment (ACE), also known as SCISAT, is a Canadian-led mission mainly supported by the Canadian Space Agency and the Natural Sciences and Engineering Research Council of Canada. We appreciate the HALOE Science Team and the many  
925 members of the HALOE project for producing and characterising the high-quality HALOE data set. We would like to thank the European Space Agency for making the MIPAS level-1b data set available and providing SCIAMACHY spectral data. The Oxford MIPAS data was provided by A. Dudhia. MLS data were obtained from the NASA Goddard Earth Sciences and Information Center. Work at the Jet Propulsion Laboratory, California Institute of Technology was done under contract with the National Aeronautics and Space Administration. Thanks to Hauke Schmidt for providing the HAMMONIA data used for the convolution of higher vertically resolved data sets. We want to express  
930 our gratitude to SPARC and WCRP (World Climate Research Programme) for their guidance, sponsorship and support of the WAVAS-II programme.

## References

- Barrett, E. W., Herndon Jr., L. R., and Carter, H. J.: Some Measurements of the Distribution of Water Vapor in the Stratosphere1, *Tellus*, 2, 302–311, <https://doi.org/10.1111/j.2153-3490.1950.tb00340.x>, <https://onlinelibrary.wiley.com/doi/abs/10.1111/j.2153-3490.1950.tb00340.x>, 1950.
- Blunier, T., Chappellaz, J. A., Schwander, J., Barnola, J. M., Desperets, T., Stauffer, B., and Raynaud, D.: Atmospheric methane, record from a Greenland Ice Core over the last 1000 year, *Geophysical Research Letters*, 20, 2219–2222, <https://doi.org/https://doi.org/10.1029/93GL02414>, <https://agupubs.onlinelibrary.wiley.com/doi/abs/10.1029/93GL02414>, 1993.
- Brewer, A. W.: Evidence for a world circulation provided by the measurements of helium and water vapour distribution in the stratosphere, *Quarterly Journal of the Royal Meteorological Society*, 75, 351–363, <https://doi.org/10.1002/qj.49707532603>, <https://rmets.onlinelibrary.wiley.com/doi/abs/10.1002/qj.49707532603>, 1949.
- Brinkop, S., Dameris, M., Jöckel, P., Garny, H., Lossow, S., and Stiller, G.: The millennium water vapour drop in chemistry-climate model simulations, *Atmos. Chem. Phys.*, 16, 8125–8140, <https://doi.org/10.5194/acp-16-8125-2016>, 2016.
- Dessler, A. E., Schoeberl, M. R., Wang, T., Davis, S., and Rosenlof, K. H.: Stratospheric water vapor feedback, *Proc Natl Acad Sci U S A*, 110, 18 087–18 091, <https://doi.org/10.1073/pnas.1310344110>, 2013.
- Dessler, A. E., Schoeberl, M. R., Wang, T., Davis, S. M., Rosenlof, K. H., and Vernier, J.: Variations of stratospheric water vapor over the past three decades, *J. Geophys. Res.*, 119, 12,588–12,598, <https://doi.org/10.1002/2014JD021712>, 2014.
- Dessler, A. E., Ye, H., Wang, T., Schoeberl, M. R., Oman, L. D., Douglass, A. R., Butler, A. H., Rosenlof, K. H., Davis, S. M., and Portmann, R. W.: Transport of ice into the stratosphere and the humidification of the stratosphere over the 2st century, *Geophys. Res. Lett.*, 43, <https://doi.org/10.1002/2016GL067991>, 2016.
- Fueglistaler, S. and Haynes, P. H.: Control of interannual and longer-term variability of stratospheric water vapor, *J. Geophys. Res.*, 110, D24108, <https://doi.org/10.1029/2005JD006019>, 2005.
- Gottelman, A., Birner, T., Eyring, V., Akiyoshi, H., Bekki, S., Brühl, C., Dameris, M., Kinnison, D. E., Lefevre, F., Lott, F., Mancini, E., Pitari, G., Plummer, D. A., Rozanov, E., Shibata, K., Stenke, A., Struthers, H., and Tian, W.: The Tropical Tropopause Layer 1960–2100, *Atmospheric Chemistry and Physics*, 9, 1621–1637, <https://doi.org/10.5194/acp-9-1621-2009>, <https://acp.copernicus.org/articles/9/1621/2009/>, 2009.
- Gottelman, A., Hegglin, M. I., Son, S.-W., Kim, J., Fujiwara, M., Birner, T., Kremser, S., Rex, M., Añel, J. A., Akiyoshi, H., Austin, J., Bekki, S., Braesike, P., Brühl, C., Butchart, N., Chipperfield, M., Dameris, M., Dhomse, S., Garny, H., Hardiman, S. C., Jöckel, P., Kinnison, D. E., Lamarque, J. F., Mancini, E., Marchand, M., Michou, M., Morgenstern, O., Pawson, S., Pitari, G., Plummer, D., Pyle, J. A., Rozanov, E., Scinocca, J., Shepherd, T. G., Shibata, K., Smale, D., Teyssède, H., and Tian, W.: Multimodel assessment of the upper troposphere and lower stratosphere: Tropics and global trends, *Journal of Geophysical Research: Atmospheres*, 115, <https://doi.org/10.1029/2009JD013638>, <https://agupubs.onlinelibrary.wiley.com/doi/abs/10.1029/2009JD013638>, 2010.
- Hall, E. G., Jordan, A. F., Hurst, D. F., Oltmans, S. J., Vömel, H., Kühnreich, B., and Ebert, V.: Advancements, measurement uncertainties, and recent comparisons of the NOAA frost point hygrometer, *Atmos. Meas. Tech.*, 9, 4295–4310, 2016.
- Hegglin, M. I., Plummer, D. A., Shepherd, T. G., Scinocca, J. F., Anderson, J., Froidevaux, L., Funke, B., Hurst, D., Rozanov, A., Urban, J., von Clarmann, T., Walker, K. A., Wang, H. J., Tegtmeier, S., and Weigel, K.: Vertical structure of stratospheric water vapour trends derived from merged satellite data, *Nature Geosci.*, 7, 768–776, <https://doi.org/10.1038/ngeo2236>, 2014.

- Hu, D.-Z., Han, Y.-Y., Sang, W.-J., and Xie, F.: Trends of Lower- to Mid-Stratospheric Water Vapor Simulated in Chemistry-Climate Models, *Atmospheric and Oceanic Science Letters*, 8, 57–62, <https://doi.org/10.3878/AOSL20140088>, 2015.
- 970 Hurst, D. F., Hall, E. G., Jordan, A. F., Miloshevich, L. M., Whiteman, D. N., Leblanc, T., Walsh, D., Vömel, H., and Oltmans, S. J.: Comparisons of temperature, pressure and humidity measurements by balloon-borne radiosondes and frost point hygrometers during MOHAVE-2009, *Atmospheric Measurement Techniques*, 4, 2777–2793, <https://doi.org/10.5194/amt-4-2777-2011>, <https://www.atmos-meas-tech.net/4/2777/2011/>, 2011a.
- Hurst, D. F., Oltmans, S. J., Vömel, H., Rosenlof, K. H., Davis, S. M., Ray, E. A., Hall, E. G., and Jordan, A. F.: Stratospheric water vapor trends over Boulder, Colorado: Analysis of the 30 year Boulder record, *J. Geophys. Res.*, 116, <https://doi.org/10.1029/2010JD015065>, 2011b.
- Hurst, D. F., Lambert, A., Read, W. G., Davis, S. M., Rosenlof, K. H., Hall, E. G., Jordan, A. F., and Oltmans, S. J.: Validation of Aura Microwave Limb Sounder stratospheric water vapor measurements by the NOAA frost point hygrometer, *J. Geophys. Res.*, 119, 1612–1625, <https://doi.org/10.1002/2013JD020757>, 2014.
- 980 Hurst, D. F., Read, W. G., Vömel, H., Selkirk, H. B., Rosenlof, K. H., Davis, S. M., Hall, E. G., Jordan, A. F., and Oltmans, S. J.: Recent divergences in stratospheric water vapor measurements by frost point hygrometers and the Aura Microwave Limb Sounder, *Atmos. Meas. Tech.*, 9, 4447–4457, <https://doi.org/10.5194/amt-9-4447-2016>, 2016.
- Inai, Y., Shiotani, M., Fujiwara, M., Hasebe, F., and Vömel, H.: Altitude misestimation caused by the Vaisala RS80 pressure bias and its impact on meteorological profiles, *Atmos. Meas. Tech.*, 8, 4043–4054, <https://doi.org/10.5194/amt-8-4043-2015>, 2015.
- 985 Kiehl, J. T. and Trenberth, K. E.: Earth’s Annual Global Mean Energy Budget, *Bull. Amer. Meteor. Soc.*, 78, 197–208, 1997.
- Kley, D., Smit, H. G. J., Vömel, H., Grassl, H., Ramanathan, V., Crutzen, P. J., Williams, S., Meywerk, J., and Oltmans, S. J.: Tropospheric water-vapour and ozone cross-sections in a zonal plane over the central equatorial Pacific Ocean, *Quarterly Journal of the Royal Meteorological Society*, 123, 2009–2040, 1997.
- Kley, D., Russell III, J. M., and Phillips, C., eds.: *Stratospheric Processes and their Role in Climate (SPARC) – Assessment of upper tropospheric and stratospheric water vapour*, WCRP No. 113, WMO/TD - No. 1043, SPARC Report No.2, WMO/ICSU/IOC, Paris, 2000.
- 990 le Texier, H., Solomon, S., and Garcia, R. R.: The role of molecular hydrogen and methane oxidation in the water vapour budget of the stratosphere, *Quarterly Journal of the Royal Meteorological Society*, 114, 281–295, <https://doi.org/10.1002/qj.49711448002>, <https://rmets.onlinelibrary.wiley.com/doi/abs/10.1002/qj.49711448002>, 1988.
- Lelieveld, J., Crutzen, P. J., and Dentener, F. J.: Changing concentration, lifetime and climate forcing of atmospheric methane, *Tellus B*, 50, 128–150, <https://doi.org/10.1034/j.1600-0889.1998.t01-1-00002.x>, <https://onlinelibrary.wiley.com/doi/abs/10.1034/j.1600-0889.1998.t01-1-00002.x>, 1998.
- 995 Lund, R. and Reeves, J.: Detection of Undocumented Changepoints: A Revision of the Two-Phase Regression Model, *J. Clim.*, 15, 2547–2554, 2002.
- Nedoluha, G. E., Bevilacqua, R. M., Gomez, R. M., Hicks, B. C., Russell III, J. M., and Connor, B. J.: An evaluation of trends in middle atmospheric water vapor as measured by HALOE, WVMS, and POAM, *Journal of Geophysical Research: Atmospheres*, 108, <https://doi.org/10.1029/2002JD003332>, <https://agupubs.onlinelibrary.wiley.com/doi/abs/10.1029/2002JD003332>, 2003.
- 1000 Nedoluha, G. E., Kiefer, M., Lossow, S., Gomez, R. M., Kämpfer, N., Lainer, M., Forkman, P., Christensen, O. M., Oh, J. J., Hartogh, P., Anderson, J., Bramstedt, K., Dinelli, B. M., Garcia-Comas, M., Hervig, M., Murtagh, D., Raspollini, P., Read, W. G., Rosenlof, K., Stiller, G. P., and Walker, K. A.: The SPARC water vapor assessment II: intercomparison of satellite and ground-based microwave measurements, *Atmos. Chem. Phys.*, 17, 14 543–14 558, <https://doi.org/10.5194/acp-17-14543-2017>, 2017.
- 1005

- Oltmans, S. and Hofmann, D.: Increase in lower-stratospheric water vapour at a mid-latitude Northern Hemisphere site from 1981 to 1994, *Nature*, 374, 146–149, <https://doi.org/10.1038/374146a0>, 1995.
- Oltmans, S. J., Vömel, H., Hofmann, D. J., Rosenlof, K. H., and Kley, D.: The increase in stratospheric water vapor from balloon-borne, frostpoint hygrometer measurements at Washington, D.C., and Boulder, Colorado, *Geophysical Research Letters*, 27, 3453–3456, <https://doi.org/10.1029/2000GL012133>, <https://agupubs.onlinelibrary.wiley.com/doi/abs/10.1029/2000GL012133>, 2000.
- 1010 Randel, W. and Park, M.: Diagnosing Observed Stratospheric Water Vapor Relationships to the Cold Point Tropical Tropopause, *Journal of Geophysical Research: Atmospheres*, 124, 7018–7033, <https://doi.org/https://doi.org/10.1029/2019JD030648>, <https://agupubs.onlinelibrary.wiley.com/doi/abs/10.1029/2019JD030648>, 2019.
- Randel, W. J., Wu, F., Vömel, H., Nedoluha, G. E., and Forster, P.: Decreases in stratospheric water vapor after 2001: Links to changes in the tropical tropopause and the Brewer–Dobson circulation, *J. Geophys. Res.*, 111, D12312, <https://doi.org/10.1029/2005JD006744>, 2006.
- 1015 Read, W. G., Stiller, G., Lossow, S., Kiefer, M., Khosrawi, F., Hurst, D., Vömel, H., Rosenlof, K., Dinelli, B. M., Raspollini, P., Nedoluha, G. E., Gille, J. C., Kasai, Y., Eriksson, P., Sioris, C. E., Walker, K. A., Weigel, K., Burrows, J. P., and Rozanov, A.: The SPARC Water Vapor Assessment II: assessment of satellite measurements of upper tropospheric humidity, *Atmos. Meas. Tech.*, 15, 3377–3400, <https://doi.org/10.5194/amt-15-3377-2022>, 2022.
- 1020 Riese, M., Ploeger, F., Rap, A., Vogel, B., Konopka, P., Dameris, M., and Forster, P.: Impact of uncertainties of atmospheric mixing on simulated UTLS composition and related radiative effects, *J. Geophys. Res.*, 117, D16305, <https://doi.org/10.1029/2012JD017751>, 2012.
- Rodgers, C. D.: Inverse Methods for Atmospheric Sounding: Theory and Practice, vol. 2 of *Series on Atmospheric, Oceanic and Planetary Physics*, F. W. Taylor, ed., World Scientific, Singapore, New Jersey, London, Hong Kong, 2000.
- Rollins, A. W., Thornberry, T. D., Gao, R. S., Smith, J. B., Sayres, D. S., Sargent, M. R., Schiller, C., Krämer, M., Spelten, N., Hurst, D. F., 1025 Jordan, A. F., Hall, E. G., Vömel, H., Diskin, G. S., Podolske, J. R., Christensen, L. E., Rosenlof, K. H., Jensen, E. J., and Fahey, D. W.: Evaluation of UT/LS hygrometer accuracy by intercomparison during the NASA MACPEX mission, *Journal of Geophysical Research: Atmospheres*, 119, 1915–1935, <https://doi.org/10.1002/2013JD020817>, 2014.
- Rosenlof, K. H., Oltmans, S. J., Kley, D., Russell III, J. M., Chiou, E.-W., Chu, W. P., Johnson, D. G., Kelly, K. K., Michelsen, H. A., Nedoluha, G. E., Remsberg, E. E., Toon, G. C., and McCormick, M. P.: Stratospheric water vapor increases over the past half-century, 1030 *Geophysical Research Letters*, 28, 1195–1198, <https://doi.org/10.1029/2000GL012502>, <https://agupubs.onlinelibrary.wiley.com/doi/abs/10.1029/2000GL012502>, 2001.
- Scherer, M., Vömel, H., Fueglistaler, S., Oltmans, S. J., and Staehelin, J.: Trends and variability of midlatitude stratospheric water vapour deduced from the re-evaluated Boulder balloon series and HALOE, *Atmos. Chem. Phys.*, 8, 1391–1402, <https://doi.org/10.5194/acp-8-1391-2008>, <https://acp.copernicus.org/articles/8/1391/2008/>, 2008.
- 1035 Schmidt, H., Brasseur, G. P., Charron, M., Manzini, E., Giorgetta, M. A., Diehl, T., Fomichev, V. I., Kinnison, D., Marsch, D., and Walters, S.: The HAMMONIA Chemistry Climate Model: Sensitivity of the Mesopause Region to the 11-year solar cycle and CO<sub>2</sub> doubling, *J. Clim.*, 19, 3903–3931, <https://doi.org/10.1175/JCLI3829.1>, 2006.
- Solomon, S., Rosenlof, K. H., Portmann, R. W., Daniel, J. S., Davis, S. M., Sanford, T. J., and Plattner, G.-K.: Contributions of Stratospheric Water Vapor to Decadal Changes in the Rate of Global Warming, *Science*, 327, 1219–1223, <https://doi.org/10.1126/science.1182488>, 1040 2010.
- Stauffer, R. M., Morris, G. A., Thompson, A. M., Joseph, E., Coetzee, G. J. R., and Nalli, N. R.: Propagation of radiosonde pressure sensor errors to ozonesonde measurements, *Atmospheric Measurement Techniques*, 7, 65–79, <https://doi.org/10.5194/amt-7-65-2014>, 2014.

- Stiller, G. P., Kiefer, M., Eckert, E., von Clarmann, T., Kellmann, S., García-Comas, M., Funke, B., Leblanc, T., Fetzer, E., Froidevaux, L., Gomez, M., Hall, E., Hurst, D., Jordan, A., Kämpfer, N., Lambert, A., McDermid, I. S., McGee, T., Miloshevich, L., Nedoluha, G., Read, W., Schneider, M., Schwartz, M., Straub, C., Toon, G., Twigg, L. W., Walker, K., and Whiteman, D. N.: Validation of MIPAS IMK/IAA temperature, water vapor, and ozone profiles with MOHAVE-2009 campaign measurements, *Atmospheric Measurement Techniques*, 5, 289–320, <https://doi.org/10.5194/amt-5-289-2012>, 2012.
- Vömel, H., David, D. E., and Smith, K.: Accuracy of tropospheric and stratospheric water vapor measurements by the cryogenic frost point hygrometer: Instrumental details and observations, *J. Geophys. Res.*, 112, <https://doi.org/10.1029/2006JD007224>, 2007a.
- 1045 Vömel, H., Yushkov, V., Khaykin, S., Korshunov, L., Kyro, E., and Kivi, R.: Intercomparison of stratospheric water vapor sensors: FLASH-b and NOAA/CMDL frost point hygrometer, *J. Atmos. Ocean. Tech.*, 27, 941–952, <https://doi.org/10.1175/JTECH2007.1>, 2007b.
- Vömel, H., Naebert, T., Dirksen, R., and Sommer, M.: An update on the uncertainties of water vapor measurements using cryogenic frost point hygrometers, *Atmos. Meas. Tech.*, 9, 3755–3768, <https://doi.org/10.5194/amt-9-3755-2016>, 2016.
- World Meteorological Organization: Definition of the tropopause, *Bulletin of the World Meteorological Organization*, 6, 136–137, 1957.